Search for Terrestrial Electron Beams in SAMPEX HILT data

Master Thesis in Space Physics
by
Vegard Aamodt

June 2015

Department of Physics and Technology
University of Bergen
Norway

"It is concluded, therefore, that the magnitude of the charge of the positive electron which we shall henceforth contract to positron is very probably equal to that of a free negative electron which from symmetry considerations would naturally then be called a negatron."

- Carl D. Anderson, 1933, *The Positive Electron*

Abstract

The Solar Anomalous and Magnetospheric Particle Explorer (SAMPEX) was a low polar orbiting satellite operating from 1992 to 2012. The goal of this master project has been to see if Terrestrial Electron Beams (TEBs), $\sim 20\,\mathrm{ms}$ bursts of electrons, were detected by the Heavy Ion Large Telescope (HILT) instrument on SAMPEX. After 1996 this instrument was switched to a mode where electrons in excess of 1 MeV were detectable, with a time resolution of 20 ms and a geometric factor of $60\,\mathrm{cm}^2\mathrm{sr}$. The time resolution and the relatively large geometric factor are reasons why we use HILT on SAMPEX.

TEBs are secondary relativistic electrons generated by Terrestrial Gamma-ray Flashes (TGFs) via Compton scattering and pair production. These electrons gyrate along geomagnetic field lines out to space. It is possible for satellites to detect such electrons several thousands of kilometers from where they originate, if the satellite passes through the actual field line at the right moment.

To distinguish real signals from variations in background noise, Poisson distribution is used to search for TEBs in HILT data for 2012. More than 300 TEB candidates, significant above background radiation, are observed. For all TEB candidates, the magnetic field lines are traced down to 45 km altitude. At the foot points we have searched for lightning using data from the World Wide Lightning Location Network (WWLLN). A null hypothesis has been performed to test if the lightning activity is random or correlated to the TEB candidates. We have done a modeling analysis of how many TEBs SAMPEX is expected to observe, compared to Fermi results. The probability of observing more than one TEB per year by SAMPEX, is estimated to be $\sim 9.8\%$.

Mostly all of the ~ 300 observed TEB candidates in 2012 are most likely something else than TEBs. Cosmic ray showers are thought to generate TEB mimic signals. One possible TEB has been found. Both in space and time, this event is correlated to two WWLLN detected lightning strokes.

Acknowledgement

First of all, I would like to thank my supervisor Prof. Dr. Nikolai Østgaard. He has during the whole master period been genuinely interested and engaged in my thesis. Thank you for excellent guidance along the way. I would also like to thank my co-adviser Dr. Thomas Gjesteland for engagement and good discussions at the weekly meetings. Thanks to Dr. Brant E. Carlson and Dr. Andrew B. Collier for spending time to answer a lot of my questions.

Thanks to Prof. Emer. Johan Stadsnes for helping with instrument technical calculations. For answering satellite related questions, I would like to thank Dr. Mark D. Looper and Dr. J. Bernard Blake in the SAMPEX Data Center Personnel group at The Aerospace Corp. and Dr. Michael S. Briggs in NASA's Fermi GBM group.

I would like to thank the institutions contributing to WWLLN and The SAMPEX Data Center, for providing data.

Thanks to all the masters students Anders, Annet Eva, Kjetil, Markus, Norah, Stefan and Theresa. Thanks to all the other employees at the Birkeland Centre for Space Science and to my friend Hallgeir Sirevaag for great support and good company.

Before and during this master project my wife Ingvild has given me great support. Thank you, Ingvild!

Finally, I would like to thank my family for the invaluable support and for all motivation through all these years at school and at the university.

Thank you,
Vegard Aamodt
31.05.2015, Bergen

Contents

List of Abbreviations

AGILE	Astrorivelatore Gamma a Immagini Leggero
ACS	Attitude Control Subsystem
BATSE	Burst and Transient Source Experiment, at CGRO
BGO	Bismuth Germanate detector
CC	Cloud-to-cloud lightning (intercloud)
CDF	The Poisson Cumulative Distribution Function
CG	Cloud-to-ground lightning
CGRO	Compton Gamma Ray Observatory
CPC	Central Processing Computer
cs	Compton scattering
DHSM	Downhill-Simplex Method
DLM	Dynamic Link Module
EIWG	Earth-Ionosphere Waveguide
ELF	Extremely Low Frequency, 3 Hz to 3000 Hz
GBM	The Gamma-ray Burst Monitor, at Fermi
HILT	Heavy Ion Large Telescope, at SAMPEX
hyp.	Hypothesis
IAGA	International Association of Geomagnetism and Agronomy
IC	Intracloud lightning
IGRF	International Geomagnetic Reference Field
IMF	Interplanetary magnetic field

LAT	Large Area Telescope, at Fermi
lat.	Latitude
LICA	Low energy Ion Composition Analyzer, at SAMPEX
LIS	Lightning Imaging Sensor
lon.	Longitude
MAST	Mass Spectrometer Telescope
MCAL	Mini-Calorimeter, at AGILE
NASA	National Aeronautics and Space Administration
OTD	Optical Transient Detector
PCF	Position-sensitive proportional counter
PCR	Rear Proportional Counter
ph	Photoelectric absorption
PET	Proton/Electron Telescope, at SAMPEX
pp	Pair production
PS set	Attitude/Orbit data, at SAMPEX
RHESSI	Reuven Ramaty High Energy Solar Spectroscopic Imager
ROI	Region Of Interest
RREA	Relativistic Runaway Electron Avalanche
SAMPEX	The Solar Anomalous and Magnetospheric Particle Explorer
SMEX	NASA's Small Explorer missions
SSD	Silicon drift detector, Solid state detector
TEBs	Terrestrial Electron Beams
TGFs	Terrestrial Gamma-ray Flashes
TLEs	Transient Luminous Events
TOGA	Time-Of-Group-Arrival
UTC	Coordinated Universal Time
VLF	Very Low Frequency, 3 kHz to 30 kHZ
WWLLN	World Wide Lightning Location Network

Chapter 1

Introduction

Terrestrial Electron Beams (TEBs) are relativistic electrons launched into space, generated by Terrestrial Gamma-ray Flashes (TGFs).

TGFs are millisecond-long bursts of energetic photons. The photons are in the energy range of megaelectron-volts (MeV) and are strongly correlated to lightning activity. This is the most energetic photon phenomenon produced on Earth and there are still many open questions according to this phenomenon. It was first discovered by *Fishman et al.* [1994] detected by The Burst and Transient Source Experiment (BATSE) on the National Aeronautics and Space Administration's (NASA) Compton Gamma-ray Observatory (CGRO).

Lightning strokes are results of strong electric fields in clouds that have been affected by electrification processes. These strong electric fields accelerate electrons to high energies, such that the electrons are able to knock out electrons that are bound to atoms or molecules. This results in a multiplication, by a factor in range of 10^{18}, of energetic electrons in a process called Relativistic Runaway Electron Avalanches (RREA). When energetic electrons interact with neutrals, they lose energy which is emitted as photons in a process called Bremsstrahlung. There is a general consensus that this is how TGFs are produced. However there is not a consensus about how and where exactly the large electric fields are produced.

When the TGFs propagate upwards in the relatively dense atmosphere, collisions occur. Terrestrial Electron Beams (TEBs) are secondary electrons and positrons produced when the gamma photons of a TGF interact with the atmosphere through Compton scattering and pair production. When these electrons/positrons reach altitudes where the collision frequency is low, they gyrate along the geomagnetic field lines into space, where they can be observed by satellites. The first TEB was discovered by *Dwyer et al.* [2008] in a re-analyzing study of the CGRO BATSE data (see BATSE TGF 2221 in Figure 1.1). One observed TGF did not confirm the established pattern of TGFs. It was a multi-peaked signal with a duration of

$\sim$ 30 ms. The satellite passed over the Sahara desert, which is not an area with high lightning activity. Similar events have also been observed over the Sahara desert by the Reuven Ramaty High Energy Solar Spectroscope Imager (RHESSI) [*Smith et al.*, 2006] and the Fermi Gamma-ray Burst Monitor (GBM) [*Briggs et al.*, 2011].

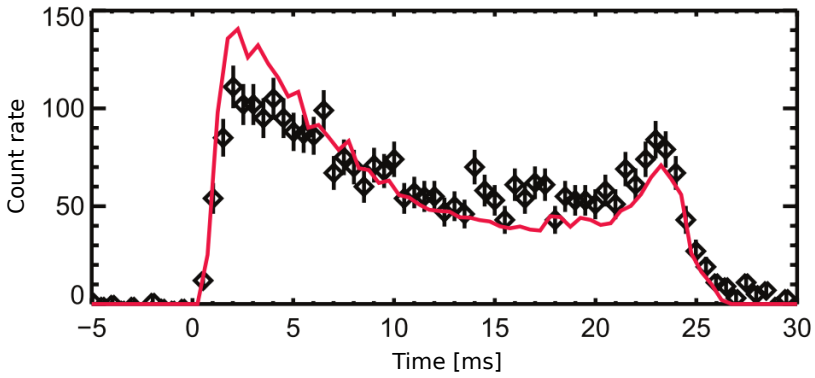

Figure 1.1: Total count rate (black points) for BATSE TGF 2221 along with the model results (red curve). The second peak is due to magnetic mirroring of the electrons by the geomagnetic field near the closest foot point. Figure and text from *Dwyer et al.* [2008].

When the satellites were passing over the Sahara desert, they were magnetically connected to a high lightning activity region further south in Africa. If a TGF generates TEBs in the southern hemisphere, a satellite could observe the gyrating electrons in the northern hemisphere, some thousands of kilometers further north. This could explain the first peak in the events. The second peak can be explained by the fact that gyrating particles mirror when the magnetic gradient becomes strong enough. Some of the electrons get lost in the atmosphere in the conjugate hemisphere and do not mirror, but a fraction gyrate back and the satellite observes this as a second and smaller peak. More than 13 TEBs have been observed so far and simulations support the double-peak signals with a total duration of 10 ms to 30 ms (see Figure 1.1) [*Dwyer et al.*, 2008; *Xiong et al.*, 2012].

The research of TEBs is quite new and there are still many open questions. Questions such as: How frequent are TEBs? Do every TGF produce TEBs? What is the role of energetic particles from thunderstorms on geospace? Do all lightning produce TGFs and TEBs? What causes the high particle energies observed? What is the electron/positron ratio in the beam? What are the lightning/TGF-ratio and the TGF/TEB ratio?

This study search for TEBs in data from the Heavy Ion Large Telescope (HILT) on the Solar Anomalous, and Magnetospheric Particle Explorer (SAMPEX). SAMPEX

was a satellite operating in a low Earth polar orbit from 1992 to the end of 2012. HILT consists of four solid state detectors with a total geometric factor of 60 cm^2sr, designed to detect electrons in excess of 1 MeV, with a time resolution of 20 ms. The time resolution and the relatively large geometric factor are reasons why we use HILT on SAMPEX.

Careful Poisson statistics is used to find events that are significant above background. 361 significant TEB candidates are observed in 2012. Every satellite position of the TEB candidates, is magnetically connected to two different foot points, one in the northern hemisphere and one in the southern hemisphere. All these foot points are searched for lightning activity using data from the World Wide Lightning Location Network (WWLLN). A null hypothesis is performed to test if the lightning activity is random or correlated to the HILT detections.

We have done a comparison analysis of how many TEBs SAMPEX is expected to observe, compared to Fermi results. The probability of observing one or more TEB per year is estimated to $\sim 9.8\%$.

Mostly all of the 361 TEB candidates are most likely something else than TEBs. It is known that such signals could be generated by cosmic rays [*Briggs et al.*, 2010]. One of 361 TEB candidates, has two WWLLN matched sferics detected ~ 125 km from the southern foot point. This is a possible TEB event.

In this thesis you will be introduced to several topics that are important for this study. In Chapter 2 we first present the electrons and the positrons, the particles we are searching for. How do electrons and positrons behave over time in electric and magnetic fields? Why do those particles bounce back and forth along geomagnetic field lines? How do photons and electrons interact with each other and what is the consequence of such interactions? All these questions are important to describe the processes that are thought to be the mechanisms behind the TEBs. When the different "tools" have been presented, we continue to describe how thunderclouds evolve and present what is known about lightning strokes. The goal is to give the reader an overview of mechanisms important for understanding high energy atmospheric physics, and especially the Terrestrial Gamma-ray Flashes (TGFs) and Terrestrial Electron Beams (TEBs), which is the focus of this thesis.

Chapter 3 presents the instrumentation and the data sets that are used in this study. Chapter 4 focuses on the methodology, e.g. the statistics in the TEB search algorithm, together with description of the comparison between HILT and WWLLN data. The observations of significant TEB candidates and lightning data are presented in Chapter 5. In Chapter 6, we discuss how many TEBs SAMPEX is expected to observe, the reliability of the TEB candidates and discuss other phenomena that could generate such signals. Chapter 7 will summarize the thesis. Finally, suggestions for future work are presented in Chapter 8.

Chapter 2

Theory and background

In this chapter we will introduce topics that are important in the study of lightning, Terrestrial Gamma-ray Flashes (TGFs) and Terrestrial Electron Beams (TEBs). We start with the particles we are searching for: electrons and positrons. We discuss how they behave over time in electric and magnetic fields. Further, we describe the gyration and bounce motion along geomagnetic field lines, interactions between particles and several other "tools" that are important for this study. In the end of this chapter, we present the mechanisms behind thunderclouds and lightning, which are important for understanding high energy atmospheric physics.

2.1 Relativistic electrons

2.1.1 Electrons, e^-

The electron was discovered by J.J. Thomson in 1897, when he measured the q/m ratio of cathode rays in his laboratory. This was the very beginning of particle physics and the beginning of understanding the atomic structure [*Tipler et al.*, 2012]. Electrons are first generation leptons, elementary particles, which mean that they have no internal structure, as far as we know. Characteristics of the electrons are given in Table 2.1.

Table 2.1: Electron characteristics [*Tipler et al.*, 2012].

Charge, q_e	$-1.60217653 \cdot 10^{-19}$ C
Rest mass, m_e	0.5110 MeV
Spin	$\frac{1}{2}\hbar$

An electron can be bound to an atom or a molecule, or be a free particle. The antiparticle of the electron is the positron, e^+. This particle has the same mass and angular momentum as the electron, but opposite charge [*McDaniel*, 1989]. The positron was predicted by P. Dirac in 1931 and discovered by C. Anderson in 1932 [*Anderson*, 1933]. Pairs of electrons and positrons are produced by pair production which will be discussed later.

2.1.2 Energies of relativistic electrons

Both TGFs and TEBs are energetic particles. Relativistic Runaway Electron Avalanches (RREA) and TEBs are relativistic electrons with energies in excess of 1 MeV, which is more than the electron rest mass ($E > m_e c^2$). The total energy of the electron is given by:

$$E_{\text{tot}} = E_0 + E_{\text{k}} = \gamma m_e c^2 \quad \text{where} \quad \gamma = \frac{1}{\sqrt{1 - \frac{v^2}{c^2}}}, \tag{2.1}$$

where E_0 is the rest energy of the electron, E_{k} is the kinetic energy, m_{e} is the electron rest mass, v is the particle speed in the laboratory frame and c is the speed of light. This expression gives us the particle velocity:

$$\beta = \frac{v}{c} = \sqrt{1 - \left(\frac{E_0}{E_0 + E_{\text{k}}}\right)^2}, \tag{2.2}$$

where β is the ratio between the particle velocity v and the speed of light c. Equation 2.2 is in this thesis used to estimate the propagation speed of Terrestrial Electron Beams with different energies (see Section 5.3.1.1).

2.2 Particle drift in electromagnetic fields

The TEBs we will study, gain their energies in strong electric fields in thunderclouds and propagate out to space affected by the Earth's magnetic field. This will be discussed in this section.

2.2.1 Electric field

For a charged particle in an electric field the Coulomb force $\mathbf{F}_{\text{C}}$, is given by:

$$\mathbf{F}_{\text{C}} = q\mathbf{E}, \tag{2.3}$$

where q is the particle charge and $\mathbf{E}$ is the electric field. In the case where an electron is located in an electric field, the Coulomb force will accelerate the electron towards the anode, as shown in Figure 2.1. The positron, which has the opposite charge, will be accelerated by the Coulomb force towards the cathode.

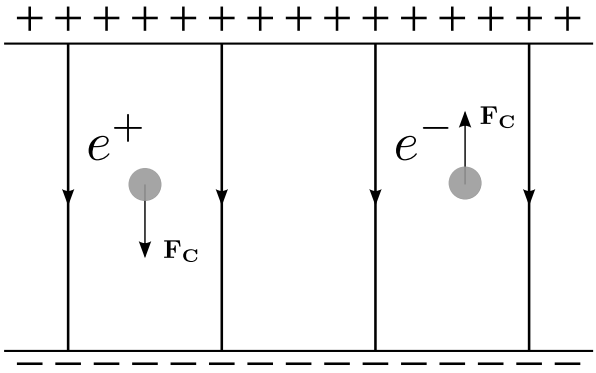

Figure 2.1: A homogeneous electric field points downward. The Coulomb force $\mathbf{F}_{\mathrm{C}}$ points towards the anode for an electron, and in the opposite direction, towards the cathode, for a positron.

2.2.2 Magnetic field

Charged particles with a velocity $\mathbf{v}$, moving in a magnetic field will experience the Lorentz force $\mathbf{F}_{\mathrm{L}}$:

$$\mathbf{F}_{\mathrm{L}} = q(\mathbf{v} \times \mathbf{B}), \tag{2.4}$$

where q is the particle charge and $\mathbf{B}$ is the magnetic field. In our situation, the electron moves in an external magnetic field (the geomagnetic field). This Lorentz force will then act perpendicular to the velocity vector of the particle, as shown in Equation 2.4. In Figure 2.2 an electron moves with a velocity vector perpendicular to a homogeneous magnetic field. The result of this is that the electron moves in a circular gyro motion. A positron's path would have been counter clockwise in the case presented in Figure 2.2, due to its opposite charge. This gyro motion is often described with the gyro frequency ω_{g} (Equation 2.5) and the gyro radius r_{g} (Equation 2.6). Both Equation 2.5 and 2.6 are valid for relativistic particles:

$$\omega_{\mathrm{g}} = \frac{qB}{\gamma m}, \tag{2.5}$$

$$r_{\mathrm{g}} = \frac{v}{|\omega_{\mathrm{g}}|} = \frac{\gamma m \beta c}{|q|B} = \sqrt{\gamma^2 - 1}\frac{mc}{|q|B}, \tag{2.6}$$

where q is the particle charge, B is strength of the magnetic field, γ is the relativistic Lorentz factor given in Equation 2.1, v and m is respectively the particle velocity and the rest mass.

According to Equation 2.6, a 1 MeV electron that gyrates at 300 km altitude (SAMPEX altitude, latitude 0°) has a gyroradius of $\sim$ 90 m. Equivalent, for a 10 MeV electron the gyroradius is $\sim$ 280 m. The magnetic field is estimated by the dipole field model, given by Equation 2.8 in Section 2.2.3. The gyro frequency is important in this thesis because it defines, together with the collision frequency, at what altitude particles are bound to the magnetic field.

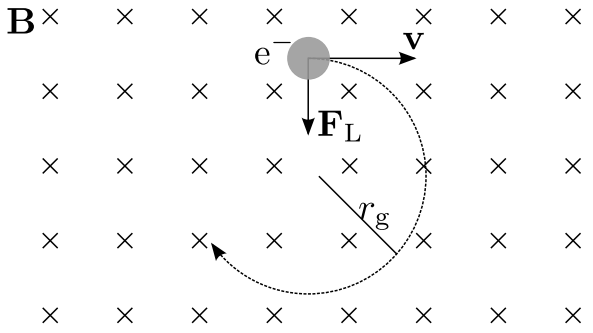

Figure 2.2: An electron with velocity $\mathbf{v}$ perpendicular to an inwards pointing homogeneous magnetic field. The Lorentz force $\mathbf{F}_{\mathrm{L}}$ points into the guiding center of the gyration path with radius r_{g}.

2.2.3 Dipole field

The Earth is surrounded by a magnetic field, due to convection processes in the outer core. This magnetic field interacts with the interplanetary magnetic field (IMF) and the solar wind. The result is that the geomagnetic field is compressed on the dayside and have a long tail at the nightside, meaning that the geomagnetic field is not symmetric as a dipole field. Close to the Earth the dipole field works as a good approximation of the geomagnetic field, see Figure 2.3, which is the region of interest in this thesis. In this case it is thought to be a dipole in the center of the Earth, along the axis of the magnetic poles. In a spherical coordinate system where origin is in the center of the Earth, radius r is the distance from origin and λ is magnetic latitude, the magnetic dipole field is given by:

$$\mathbf{B} = \frac{\mu_0}{4\pi}\frac{M_{\mathrm{E}}}{r^3}(-2\,sin\,\lambda\hat{\mathbf{e}}_r + cos\,\lambda\hat{\mathbf{e}}_\lambda), \tag{2.7}$$

where μ_0 is the permeability of free space, $M_{\mathrm{E}} = 8.05 \cdot 10^{22}\,\mathrm{Am}^2$ is the Earth's dipole moment, $\hat{\mathbf{e}}_r$ and $\hat{\mathbf{e}}_\lambda$ are unit vectors respectively in the r and λ direction. The

strength of the dipole field is given by:

$$B = \frac{\mu_0}{4\pi}\frac{M_{\mathrm{E}}}{r^3}(1 + 3\,sin^2\,\lambda)^{1/2}. \tag{2.8}$$

To get an expression of the magnetic field line $r = f(\lambda)$, it can be shown by using the cross product $\mathrm{d}\mathbf{s} \times \mathbf{B} = 0$, where $\mathrm{d}\mathbf{s}$ is an arc element, and Equation 2.7 that r is given by:

$$r = r_{eq}\,cos^2\,\lambda, \tag{2.9}$$

where r_{eq} is the equatorial radius to the magnetic field line. The relation $B \propto 1/r^3$ given in Equation 2.8 is used in a modeling of the pitch angles at different altitudes presented in Section 6.1.5. The pitch angle is presented in Section 2.2.4.

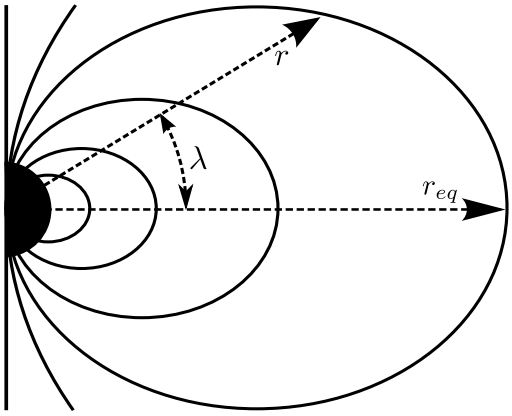

Figure 2.3: Dipole magnetic field lines, where r is the radius from the Earth center to an actual point on a magnetic field line, r_{eq} is the equatorial radius from the center of the Earth to the actual field line and λ is the angle between r and r_{eq}. Adapted from *Baumjohann and Treumann* [1997].

2.2.4 Pitch Angle

The pitch angle α is defined as the angle between the particle velocity vector $\mathbf{v}$ and the magnetic field line $\mathbf{B}$. It is given by:

$$\alpha = tan^{-1}\Big(\frac{v_\perp}{v_\parallel}\Big), \tag{2.10}$$

where $v_\perp$ and $v_\parallel$ are the velocity vectors respectively perpendicular and parallel to the magnetic field. This is shown schematically in Figure 2.4. Pitch angle is important when we shall explain the two peak structure with the tails, in a characteristic TEB signal (see Figure 1.1).

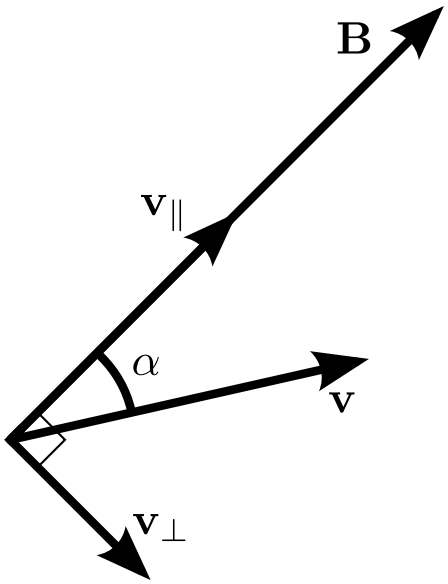

Figure 2.4: A schematically diagram of the pitch angle α, that is the angle between the particle velocity $\mathbf{v}$ and the magnetic field line $\mathbf{B}$. $\mathbf{v}_\parallel$ and $\mathbf{v}_\perp$ are the velocity vector components respectively parallel and perpendicular to the magnetic field.

2.2.5 Bounce motion

Consider a charged particle, in our case an electron or a positron, gyrating in a static converging magnetic field and the only force acting on the particle is the Lorentz force. This is the case when TEBs propagate along geomagnetic field lines. The speed of the particle has two components $\mathbf{v} = \mathbf{v}_\perp + \mathbf{v}_\parallel$ according to the magnetic field (see Figure 2.4). As can be seen in Figure 2.5, the Lorentz force has a component in the positive $\hat{\mathbf{z}}$-direction, that accelerates the particle in this direction. When a particle gyrates into a region where the magnetic field strength is increasing, the $\mathbf{v}_\parallel$ component will decrease and approach zero, and then move back into the region where the field strength is decreasing. The point where $\mathbf{v}_\parallel$ equals zero is called the mirror point. In a static magnetic field, $|\mathbf{v}|$ is constant. When the particle moves towards the mirror point $\mathbf{v}_\parallel \to \mathbf{v}_\perp$ and $\mathbf{v}_\perp \to \mathbf{v}_\parallel$ in the other case. In other words, the particle mirrors when the pitch angle is 90°.

If we take the first adiabatic invariant,

$$\mu = \frac{mv^2 \, sin^2 \, \alpha}{2B}, \tag{2.11}$$

into account, where we assume that the magnetic moment μ is constant along the magnetic field lines, the magnetic field strength in the mirror point B_m is given by:

$$B_\mathrm{m} = \frac{B_\mathrm{e}}{sin^2 \, \alpha_\mathrm{e}}, \tag{2.12}$$

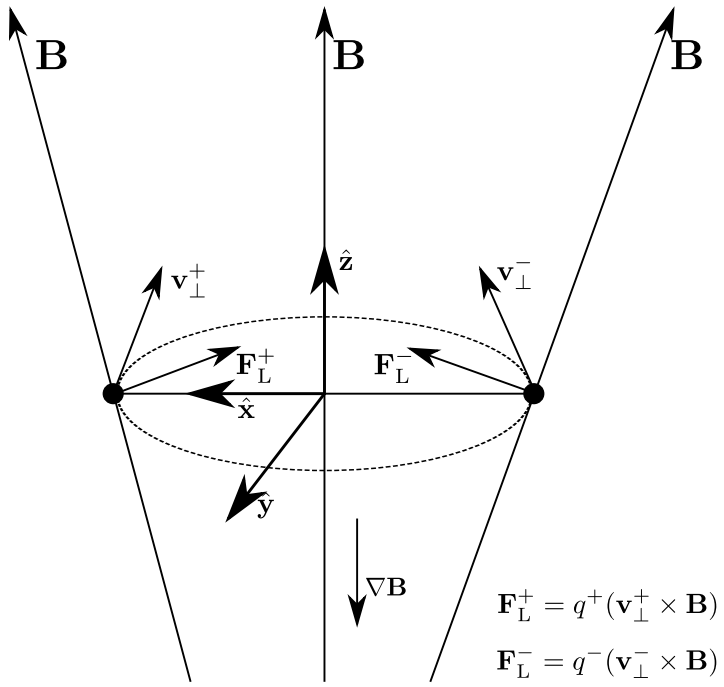

Figure 2.5: Schematically diagram of a gyrating particle in an inhomogeneous magnetic field, where the $\nabla\mathbf{B}$ is pointing downwards, $\mathbf{v}_\perp$ is perpendicular both to the magnetic field and the Lorenz force $q(\mathbf{v}_\perp \times \mathbf{B})$. The Lorentz force has a positive component in the $\hat{\mathbf{z}}$-direction that is accelerating both a positive and a negative particle in the opposite direction of $\nabla\mathbf{B}$. This acceleration is a change in direction, the energy is conserved.

where B_e is the magnetic field strength of the actual field line at equator and α_e is the equatorial pitch angle. The smaller the equatorial pitch angle is, the greater is the magnetic field strength in the mirror point (see Equation 2.12). If the mirror point is too deep into the atmosphere, the particle will experience collisions, lose its energy and will never return. In the case of mirroring TEBs, just a fraction of the beam mirrors. The rest is absorbed in the atmosphere at the conjugate hemisphere of the source.

It can be shown, from Equation 2.11, that the pitch angle of gyrating particles varies with the strength of the magnetic field, given by:

$$\frac{sin^2\,\alpha_\mathrm{a}}{sin^2\,\alpha_\mathrm{b}} = \frac{B_\mathrm{a}}{B_\mathrm{b}}, \tag{2.13}$$

where α_a and α_b is respectively the pitch angle at location a and b, and B_a and B_b is the corresponding magnetic field strengths. Equation 2.13 is used to calculate the pitch angle at different altitudes, in a comparison analysis between SAMPEX and Fermi (see Section 6.1.5).

2.3 Interaction between electromagnetic radiation and particles

In this section we will study the most important interactions included in the mechanisms of TGFs and TEBs. We start by introducing the cross section to define the effective size of interacting particles. Further, we describe scattering of electrons and positrons (Møller and Bhabha scattering), how particles generate electromagnetic radiation (Bremsstrahlung) and how electromagnetic radiation generates particles (photoelectric absorption, Compton scattering and pair production).

2.3.1 Cross section

The probability that two particles interact/collide with each other depends on the particle energies and their properties [*Tipler et al.*, 2012]. A measure of this probability is correlated to a measure of the Coulomb size of a particle, the cross section σ. This is a quantity that has the dimension of area. Since we talk about magnitudes in the order of πr_{n}^2, where r_{n} is in the range of a nucleus radius, barn is a useful cross section unit:

$$1\,\mathrm{barn} = 10^{-24}\,\mathrm{cm}^2 = 10^{-28}\,\mathrm{m}^2.$$

The cross section σ, for a particular reaction is defined as:

$$\sigma\,[\mathrm{barn}] = \frac{R}{I} = \frac{\nu_{\mathrm{c}}}{N}, \tag{2.14}$$

where R is the number of reactions per unit time per nucleus and I is the number of particles incident per unit time per area. ν_{c} is the collision frequency and I is a measure of incident intensity.

The cross section is a function of energy, particle properties and is also dependent on what kind of interaction that occurs. This means that for every possible interaction process, we have to find a partial cross section. The total cross section σ_{tot}, is then given by the sum of partial cross sections:

$$\sigma_{\mathrm{tot}} = \sum_{i=1}^{n} \sigma_i = \sigma_1 + \sigma_2 + \sigma_3 + ... + \sigma_n. \tag{2.15}$$

In the case where photons interact with matter, photoelectric effect (ph), Compton scattering (cs) and pair production (pp) are the dominating processes. The total cross section is then given by:

$$\sigma_{\mathrm{tot}} = \sigma_{\mathrm{ph}} + \sigma_{\mathrm{cs}} + \sigma_{\mathrm{pp}}, \tag{2.16}$$

which for photon interactions in air is plotted in Figure 2.11 in Section 2.3.4.4.

The mean free path λ for particles, is a measure of how far a particle on average can propagate, before it hits a target. This is correlated to the cross section σ, and the relation is given by:

$$\lambda\,[\text{meter}] = \frac{1}{n\sigma}. \tag{2.17}$$

where n is the molecular/atomic number density.

2.3.2 Scattering of electrons and positrons

In this section scattering of leptons are described. This is important in the mechanisms generating runaway electrons, that produces TGFs.

2.3.2.1 Møller and Bhabha scattering

Møller and Bhabha scattering are electromagnetic scattering of leptons, more particularly: electrons and positrons. Møller scattering is scattering where two electrons interact, as shown in Figure 2.6, a and b. These two processes are indistinguishable. By this, it is impossible to claim if process a or b have taken place. Because of this, the probability of each process to occur has to be added together, not the intensities [*Henley and Garcia*, 2007]. Møller scattering is important in the avalanche process, which will be discussed later.

Bhabha scattering is scattering of electrons and positrons, as can be seen in Figure 2.6, c and d. These two particles can be distinguished, by their opposite charges, but as for Møller scattering, it is impossible to claim which one of the processes described in Figure 2.6, c or d, that has occurred. The probability of each process to occur has to be added, as for Møller scattering.

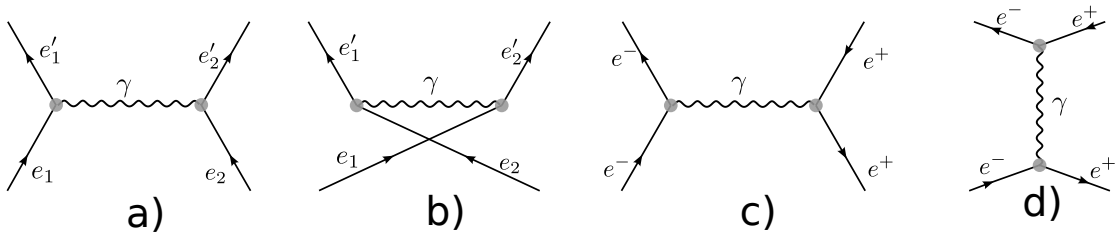

Figure 2.6: This sketch shows the concept (Feynman diagram) of Møller scattering, $e^- + e^- \rightarrow e^- + e^-$ (a and b), and Bhabha scattering, $e^+ + e^- \rightarrow e^+ + e^-$ (c and d). Adapted from [*Henley and Garcia*, 2007]

.

The cross section for Møller and Bhabha scattering is defined by quantum electrodynamics and Dirac theory. For large energies, $E \gg m_e c^2$, the cross section is given as:

$$\frac{d\sigma}{d\Omega} = \frac{\alpha^2}{E^2}(\hbar c)^2 f(\theta), \tag{2.18}$$

where $\alpha = e^2/\hbar c$ is the fine structure constant, E is the particle energy and $f(\theta)$ is a function of the scattering angle θ [*Henley and Garcia*, 2007]. As seen from Equation 2.18, the cross section for Møller and Bhabha processes are dependent on the particle energy and the scattering angle.

Møller and Bhabha scattering are more discussed in Section 2.5.2, where runaway electron generating mechanisms are introduced.

2.3.3 Particles generating electromagnetic radiation

TGFs are electromagnetic radiation generated by a process called Bremsstrahlung. This process will be presented in this section.

2.3.3.1 Bremsstrahlung

Classical electromagnetic theory predicts that an accelerated charged particle emits electromagnetic radiation [*Tipler et al.*, 2012]. When an energetic charged particle is deflected or slowed down by a Coulomb field of another charged particle, the change in momentum is emitted as a photon (see Figure 2.7). This process is called Bremsstrahlung or braking radiation. It is called Bremsstrahlung because it was first discovered when fast electrons were stopped in a metallic plate. Bremsstrahlung is one of the most important energy loss processes for electrons, but not so important for heavier particles as muons, pions and protons [*Henley and Garcia*, 2007].

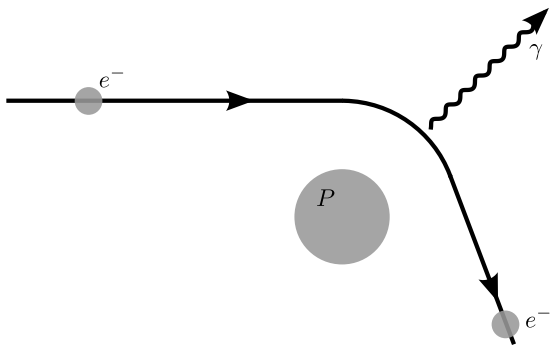

Figure 2.7: Schematically diagram of the concept of Bremsstrahlung, where an incoming electron interacts with a particle P.

Energy loss of electrons is dominated by radiation when the electron energy E, is in excess of a critical energy E_c, given as:

$$E_c \approx \frac{600\,MeV}{Z}, \tag{2.19}$$

where Z is the charge number of the absorber's atom. $E < E_c$ is called the ionization region [*Henley and Garcia*, 2007].

In our case where $Z \sim 8$ and $E \sim 10\,\mathrm{MeV}$, most of the electrons are in the ionization region ($E < E_c$) where ionization dominates the energy loss, but some electrons are deflected from its initially trajectory and slowed down in the Coulomb field of a nucleus, due to the Coulomb force. The deflected electron has lost some of its kinetic energy, which is emitted as a photon. Bremsstrahlung photons with energies above 1 MeV may produce pairs of electrons and positrons, which we will come back to when we describe pair production.

2.3.4 Electromagnetic radiation generating particles

Photons interact with matter in three different processes: photoelectric effect, Compton scattering and pair production [*Henley and Garcia*, 2007]. In this section we will describe them one by one, and we will focus on the collision process itself and the energy - cross section relation. These interactions are important for the study of the TEB mechanism, presented in Section 2.5.4.2.

2.3.4.1 Photoelectric absorption

In 1905 Albert Einstein presented his theory of photoelectric absorption or the photoelectric effect (schematically presented in Figure 2.8). The photon energy is given by $E = h\nu$, where h is the Planck constant ($h = 6.63 \cdot 10^{34}\,\mathrm{Js}$) and ν is the frequency. The electron has to be bound to an atom, because the momentum of a free electron would not be conserved if it has absorbed a photon. After photon absorption the kinetic energy of the electron is given by:

$$E_\mathrm{K} = h\nu - E_\mathrm{b} - E_\mathrm{A} \approx h\nu - E_\mathrm{b}, \tag{2.20}$$

where E_b is the electron binding energy and E_A is the energy transferred to the atom. Because of the mass ratio $m_\mathrm{electron}/m_\mathrm{proton} = 1/1\,836$, we can do the approximation were we neglect the energy transferred to the atom.

To give an expression for the total cross section of this process is complicated, and electrons in an atom interact with each other. The relativistic wave function by Dirac describes the bound electron in an atom. If we just take the K-shell into account,

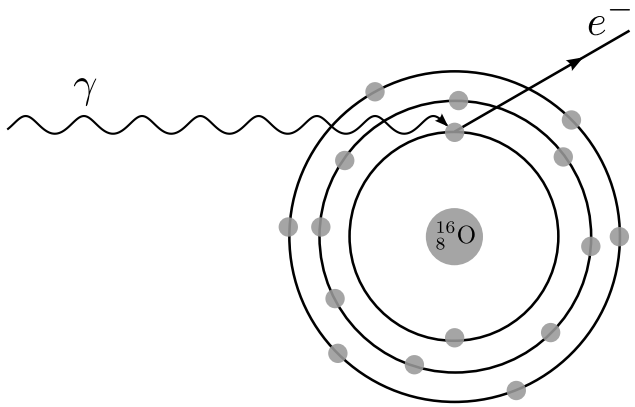

Figure 2.8: Schematically diagram of the concept of photoelectric absorption, where an incoming photon collides with a bound electron.

and do some non-relativistic calculations, we can use the Born approximation to find the photon cross section, given by:

$$\sigma_{\text{ph}} = \frac{32\sqrt{2}\alpha^4 r_{\text{e}}^2 Z^5}{3}\left(\frac{m_{\text{e}}c^2}{h\nu}\right)^{7/2} \quad \text{where} \quad r_{\text{e}} = \frac{e^2}{4\pi\epsilon_0 m_{\text{e}}c^2}, \tag{2.21}$$

where α is the fine structure constant, m_{e} is the rest mass of the electron, c is the speed of light, Z is the atomic number, r_{e} is the classical electron radius, e is the electron charge, ϵ_0 is the permittivity constant of free space, h is the Planck constant and ν is the incoming photon frequency [*Carlson*, 2009].

2.3.4.2 Compton scattering

An inelastic collision between a photon and a free electron, where the photon is scattered away with less energy than it had before the collision, is a phenomenon called Compton scattering. If we consider a free electron initially at rest and take into account the conservation of momentum and energy, we can write the expression as:

$$p = \frac{h\nu}{c} = \frac{h\nu'}{c}cos\,\theta + p_{\text{e}}cos\,\phi \quad \text{and} \quad \frac{h\nu'}{c}sin\,\theta = p_{\text{e}}sin\,\phi, \tag{2.22}$$

$$E = h\nu = E' + E_K = h\nu' + E_{\text{K}} \quad \text{where} \quad p_{\text{e}}c = \sqrt{E_{\text{K}}(E_K + 2m_{\text{e}}c^2)}. \tag{2.23}$$

By some manipulation of these equations, you get:

$$E' = h\nu' = \frac{h\nu}{1+\epsilon(1-cos\,\theta)} = \frac{E}{1+\epsilon(1-cos\,\theta)}, \tag{2.24}$$

$$E_{\text{K}} = \frac{\epsilon(1-cos\,\theta)h\nu}{1+\epsilon(1-cos\,\theta)} = \frac{\epsilon(1-cos\,\theta)E}{1+\epsilon(1-cos\,\theta)}, \tag{2.25}$$

$$cot\,\phi = (1+\epsilon)tan\,\frac{\theta}{2} \quad \text{where} \quad \epsilon = \frac{E}{m_e c^2} = \frac{h\nu}{m_e c^2}. \tag{2.26}$$

Equation 2.24 may be written as:

$$\lambda' - \lambda = \frac{h}{m_e c}(1 - cos\,\theta) \quad \text{and} \quad \frac{1}{E'} - \frac{1}{E} = \frac{1}{m_{\mathrm{e}} c^2}(1 - cos\,\theta), \tag{2.27}$$

where p is the photon momentum, h is the Planck constant, ν, ν', E and E' are the frequency and energy respectively before and after the collision, c is the speed of light, p_e is the electron momentum, m_{e} is the rest mass of the electron and E_{K} is the kinetic energy to the electron after the collision. The geometry is presented in Figure 2.9. From Equation 2.27 we can see that the change in photon energy is dependent on the scattered angle of the electron and independent of the incoming photon energy. We have the largest energy transfer from the photon to the electron when $\theta = \pi$ or $\theta = 3\pi/4$.

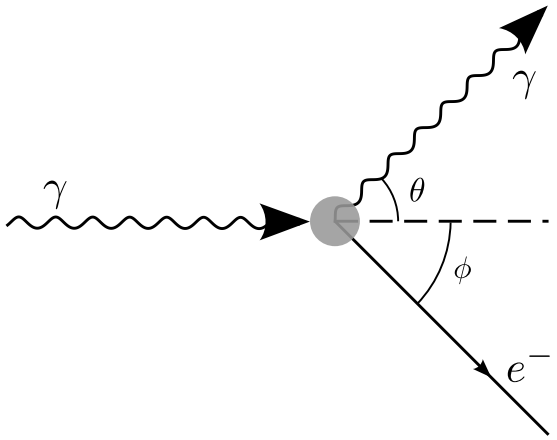

Figure 2.9: Schematically diagram of the concept of Compton scattering, where a photon collides with an electron. θ and ϕ is respectively the angle between the outgoing photon/electron and the direction of the ingoing photon.

The differential cross section per electron $\mathrm{d_e}\sigma_{\mathrm{cs}}/\mathrm{d}\Omega$, is called the Klein-Nishina formula and derived from the relativistic Dirac wave equation. If we integrate over all angles, we get the total Compton cross section, given by:

$$\begin{aligned}\sigma_{\mathrm{cs}} &= \int_0^{2\pi} d\phi \int_0^{\pi} sin\,\theta\, d\theta\, \frac{\mathrm{d_e}\sigma_{\mathrm{cs}}}{\mathrm{d}\Omega} \\ &= 2\pi r_e^2 \left\{ \frac{1+\epsilon}{\epsilon^2}\left[\frac{2(1+\epsilon)}{1+2\epsilon} - \frac{\ln(1+2\epsilon)}{\epsilon}\right] + \frac{\ln(1+2\epsilon)}{2\epsilon} - \frac{1+3\epsilon}{(1+2\epsilon)^2} \right\},\end{aligned} \tag{2.28}$$

where $\epsilon = h\nu/m_{\mathrm{e}}c^2$, where h is the Planck constant, ν is the frequency, m_{e} is the rest mass of the electron and c is the speed of light. r_{e} is the classical electron radius, as given earlier in the text [*Carlson*, 2009; *Skeltved*, 2013].

2.3.4.3 Pair production

If a photon has more energy than two times the rest mass of a particle, it may produce a pair of particles. This process is called pair production. It is impossible to occur in free space, because energy and momentum conservation could not be fulfilled when a mass less photon decays into relatively heavy particles [*Henley and Garcia*, 2007]. Since the photon has no charge, due to conservation laws, the algebraic sum of the produced particle pair charge has to be zero. For the same reason, the momentum has to be conserved by another particle P, or system of particles (see Figure 2.10) [*McDaniel*, 1989]. The rest mass of an electron is 511 keV, which means that the photon energy threshold is 1.022 MeV for electron-positron pair production to occur. This energy threshold is dependent on the particle P. The process can be described as:

$$\gamma + \mathrm{P} \rightarrow \mathrm{P} + e^- + e^+, \tag{2.29}$$

where γ is the incoming photon, P is the "particle" and e^- and e^+ is the electron-positron pair.

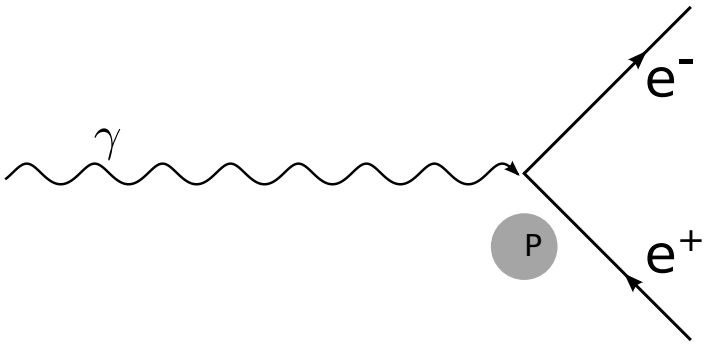

Figure 2.10: Schematically diagram of the concept of pair production, where an incoming photon interacts with a particle P and produce an electron-positron pair.

The kinetic energy of the electron and the positron, is given by:

$$E_{\mathrm{K}e^{+/-}} = \frac{E_\gamma - 2m_\mathrm{e}c^2}{2}, \tag{2.30}$$

where E_γ is the energy of the incoming photon $E_\gamma = h\nu$, m_e is the electron/positron rest mass and c is the speed of light. The conservation of momentum and energy works both ways, which means that an electron-positron pair can annihilate and produce two or three photons [*Tipler et al.*, 2012].

The cross section of pair production is complicated and can be approximated from quantum electrodynamics in different ways. If the photon energy $h\nu \gg 137\,\mathrm{m_e c^2\,Z^{-1/3}}$, the pair production cross section is given by:

$$\sigma_\mathrm{pp} \approx 4Z^2\alpha r_\mathrm{e}^2 \Big\{ \frac{7}{9}\left[\ln(183\,Z^{-1/3}) - f(Z)\right] - \frac{1}{54} \Big\}, \tag{2.31}$$

where $f(Z)$ is a correction factor according to Coulomb interaction between the pair produced particles and the particle P [*Carlson*, 2009].

2.3.4.4 Total cross section for photons in air

The cross section for each photon interaction process: photoelectric absorption, Compton scattering and pair production, in air are presented in Figure 2.11, together with the total cross section, given as Equation 2.16. For photons in excess of 1 MeV, in the case of TGFs, Compton scattering and pair production dominates. TEBs are thought to be generated by these two processes (see Section 2.5.4.2).

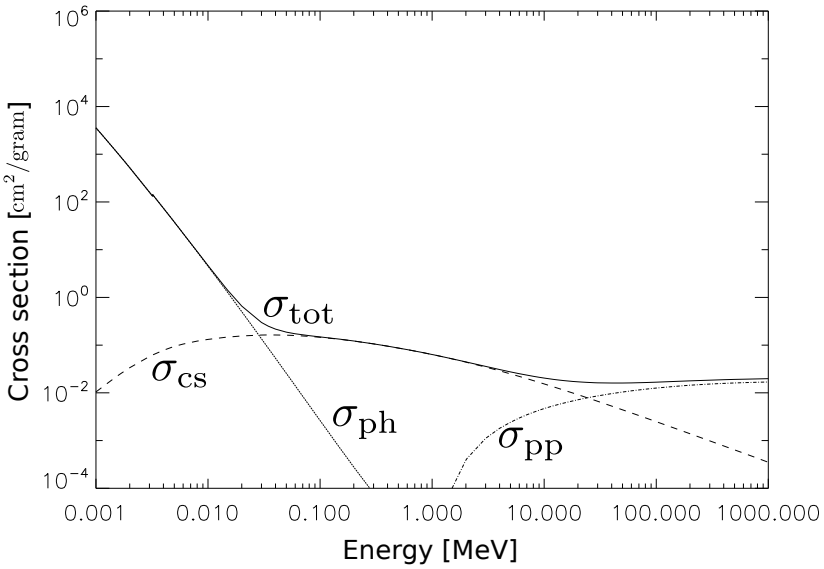

Figure 2.11: Cross section of photon interacting processes in air. σ_{ph} is for photoelectric absorption, σ_{cs} is for Compton scattering and σ_{pp} is for the pair production. The total cross section, sum of all three processes, is the σ_{tot}. Data collected from *Berger et al.* [1998].

2.4 Thunderclouds and lightning

Lightning is thought to be the origin of TGFs and TEBs, and is in this relation relevant for this thesis. It is an electric discharge process in strong electric fields of thunderclouds. It is one of the most fascinating and impressive geophysical phenomena that is commonly occurring on Earth [*Dwyer and Uman*, 2014]. At any time, humans have been fascinated and skeptical to thunderstorms. It produces one of the loudest sounds and brightest lights that we are exposed to. Lightning is dangerous. It may start house- and wildfires, is induced and affects our electrical circuits and it can be disastrous if humans are struck by them. Both the bright light and the loud sound have in the past been explained by religious affiliations, for example Thor with his hammer Mjölnir in Norse mythology. The first known systematical scientific work according to lightning and thunderstorms was done by B. Franklin (1706-1790). Using kites and laboratory experiments he discovered that lightning was an electrical process[*Dwyer and Uman*, 2014].

Lightning is quite common. Every second there are (44 ± 5) cloud-to-cloud and cloud-to-ground discharges, which means there are roughly 4 million discharges per day or 2.7 per km^2 per year [*Christian*, 2003].

In this section we will describe lightning as a physical phenomenon and study the processes behind it. We start with the evolution and electrification process of thunderclouds, further describe a model used to estimate the electric field and the charge distribution, then we will discuss the initiation process of lightning, the streamer and leader theory. In the end of this section we describe radio waves emitted from lightning and their propagation used for lightning detection. This is important for understanding how WWLLN detects lightning strokes.

2.4.1 Evolution and electrification of thunderclouds

Typical thunderclouds, where lightning occurs, are the cumulonimbus clouds. These clouds have been developed from small fair-weather clouds, called cumulus. A thunderstorm is a system of thunderclouds, and both terms are used in this text. Cumulus is a result of parcels of warm and moist air that rise and cool due to adiabatic expansion (see Figure 2.12) [*Rakov and Uman*, 2007]. Adiabatic means that there is no heat transfer out of the parcels, as in a saucepan of boiling water. This convection process is also important for the electrification of a cumulonimbus, which we will discuss later in this section.

The height of a thundercloud is dependent on ground humidity and the atmospheric temperature lapse rate, which is the decrease in temperature with increasing altitude. If a parcel of air is going to rise, the temperature gradient in the ambient air has to be larger than the moist-adiabatic lapse rate, that is about $-0.6\,^{\circ}\text{C}$

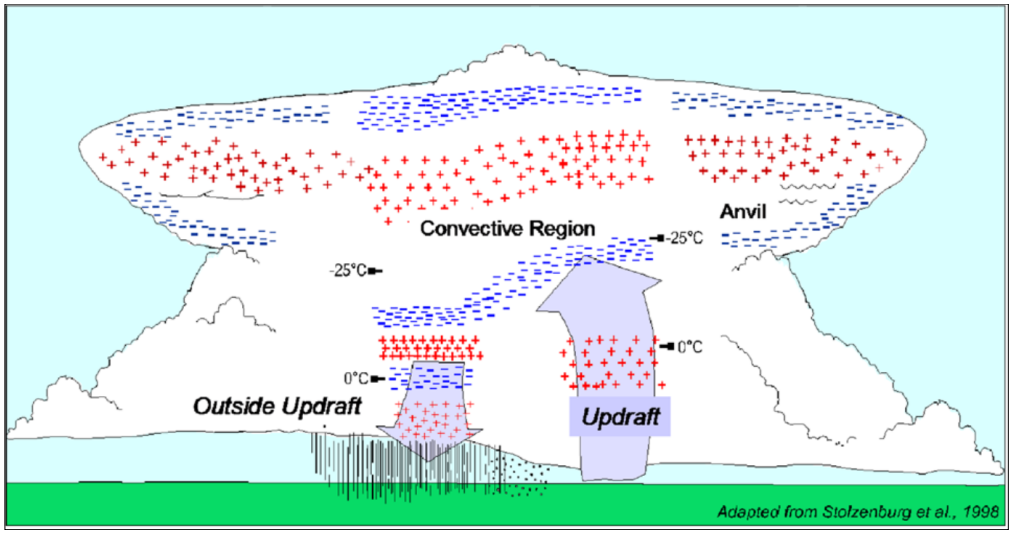

Figure 2.12: This sketch shows a charge distribution model of a thundercloud where we have a main positive and a main negative region and a convection cell where updraft dominates. Figure from *Stolzenburg and Marshall* [2008]; *Stolzenburg et al.* [1998]

per 100 m. The temperature in the lower atmosphere (troposphere) decreases with increasing altitude, up to the tropopause. Above this altitude, in the stratosphere, the temperature increases with height. The height of the troposphere can vary from approximately 8 km at high latitudes in the winter, to approximately 18 km at lower latitudes during summer time.

The size of a thunderstorm can vary from relatively small systems that cover an area of about 100 km^2 to 300 km^2, a circle of radius between 6 km to 10 km, to bigger systems that can be more than hundred times larger [*Dwyer and Uman*, 2014]. Those are typically composed of smaller thunderstorms that have merged together in groups along cold fronts [*Rakov and Uman*, 2007]. Small systems may produce cloud-to-ground lightning every 20 s to 30 s, compared to every second for large systems [*Dwyer and Uman*, 2014].

A thunderstorm often consists of units of convection, which we call convection cells. These cells are in the order of some kilometers in radius and may exist for about an hour. The characteristics of a convection cell is an updraft of air with speed in excess of 10 $m \cdot s^{-1}$ [*Rakov and Uman*, 2007].

At altitudes where we have temperatures between $-10\,°C$ and $-20\,°C$, there is a mixture of super cooled water droplets and ice particles, called hydrometeors. This is the region where the cloud electrification process occurs. Hydrometeors are divided into two different categories: precipitation particles and cloud particles. The first one are soft hail particles where the acting forces are dominated by gravity and the

fall speed is more than $0.3\,\mathrm{m}\cdot\mathrm{s}^{-1}$ even in the updraft zone, e.g. graupel particles. The other ones are small crystals of ice, light enough to be drawn up in the updraft. Hydrometeors are thought to be the dominating charge carrier in thunderclouds, due to collisions. The idea is that after collisions between graupels and ice crystals, the light ice crystals are positively charged and do rise in the updraft towards the top of the cloud. The negatively charged graupels are located in the middle of the cloud, due to heavier weight, as described above. This is called the non-inductive charge mechanism [*Dwyer and Uman*, 2014]. More of this process will be discussed in the paragraph about the tripole charge model (see Section 2.4.2).

2.4.2 Tripole charge model

The most accepted simple charge model for a thundercloud is the tripole model (see Figure 2.13). It consists of a relatively strong positive charge region at the top of the cloud, called main positive charge center (P), and a negative charge region, called main negative charge center (N), with the same magnitude but opposite sign, in the middle. At the bottom of the cloud there is thought to be a weak positive charge region, called the lower positive charge center (LP), above a perfect conducting ground. The two charges at the top form a dipole and are called the main charges. The weak positive charge center, at the bottom, is not always present [*Stolzenburg and Marshall*, 2008].

The electric field intensity $\mathbf{E}$, correlated to a thundercloud at a distance r from the vertical charge axis along the sea-level, can be found by using the tripole model, as seen in Figure 2.13. To compensate for the conducting ground/surface, it can be made a mirror image of the three point charges and use the principle of superposition, as seen in Figure 2.14. This is a way where the Earth's surface behaves like the ground potential. It is called the "method of images", a traditional problem-solving tool in electrostatics. The total electric field will be the sum of six contributions, three from the charges seen in Figure 2.13 and three from the mirror image.

The electric field component due to the point charge and its image, measured in a horizontal distance r from the point charge, is given by:

$$|\mathbf{E}^{(-)}| = |\mathbf{E}^{(+)}| = \frac{|Q|}{4\pi\epsilon_0(H^2 + r^2)}, \tag{2.32}$$

where the permittivity of free space $\epsilon_0 = 8.85 \cdot 10^{-12}\,\mathrm{C}^2 \cdot \mathrm{N}^{-1} \cdot \mathrm{m}^{-2}$, $|Q|$ is the magnitude of the charge and H is the point charge altitude (see Figure 2.14).

The magnitude of the total electric field in the vertical direction is twice the vertical

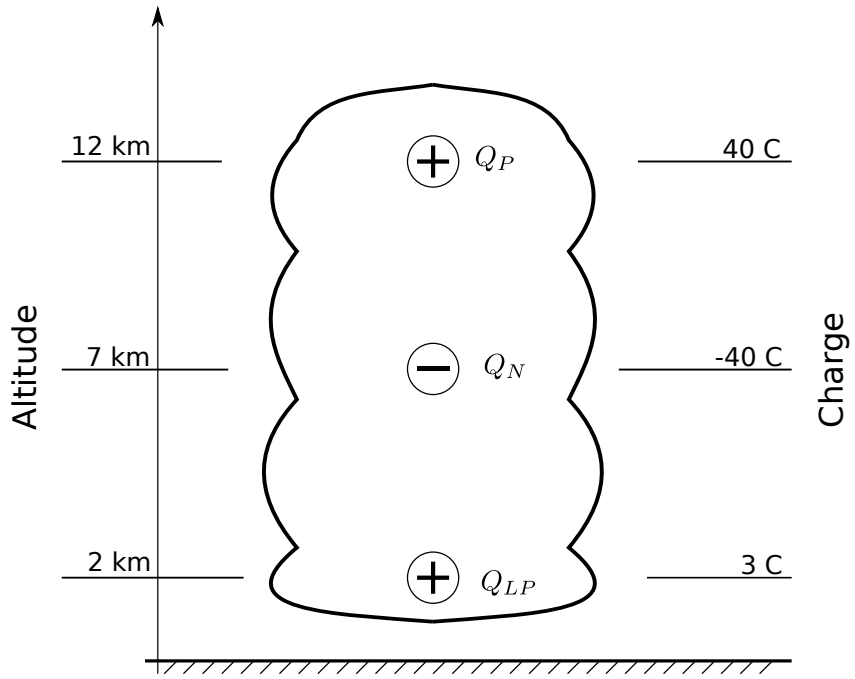

Figure 2.13: This sketch shows a tripole model of the charge distribution in a thundercloud. Q_P is the main positive region, located in the upper part of the cloud. In this case it is thought to be a point charge of +40 C at an altitude of 12 km. Q_N is the main negative charge, that is a point charge of −40 C at an altitude of 7 km. Q_P and Q_N are point charges with the same magnitude, but opposite sign. Q_{LP} is the lower positive charge region, a point charge of 3 C at an altitude of 2 km. Adapted from *Rakov and Uman* [2007]

component of $|\mathbf{E}^{(+)}|$ and $|\mathbf{E}^{(-)}|$:

$$\begin{aligned} |\mathbf{E}| &= 2|\mathbf{E}^{(-)}| cos\,(90^\circ - \alpha) = 2|\mathbf{E}^{(+)}| cos\,(90^\circ - \alpha) \\ &= 2|\mathbf{E}^{(-)}| sin\,\alpha \\ &= \frac{|Q|H}{2\pi\epsilon_0(H^2 + r^2)^{3/2}} \\ &= k\frac{sin\,\alpha}{R^2} \quad \text{if Q is constant, } k = \frac{|Q|}{2\pi\epsilon_0} \quad \text{and} \quad R^2 = (H^2 + r^2). \end{aligned} \tag{2.33}$$

The last expression in Equation 2.33 is just a simplification that makes it easier to discuss. α is the angle between the horizontal plane and the respective electric field vector.

The total electric field composed by the three individual point charges, as shown in Figure 2.13, can now be calculated, by Equation 2.33, as the algebraic sum of every contribution. This is done for $Q_\mathrm{P} = 40\,\mathrm{C}$ at $H_\mathrm{P} = 12\,\mathrm{km}$, $Q_N = -40\,\mathrm{C}$ at

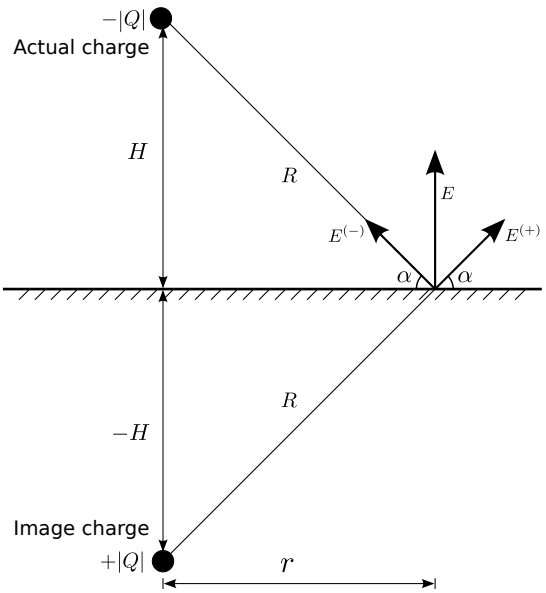

Figure 2.14: This sketch shows the components of the electric field intensity in a thundercloud, calculated by using the principle of superposition and a mirror image of a point charge at a given altitude. The image charge compensates for the perfectly conducting ground. H is the altitude of the point charge, r is the horizontal distance between the vertical charge axis and the "observer" location, at sea level. R is given by $R = \sqrt{H^2 + r^2}$, α is the angle between the radial electric field vector ($\mathbf{E}^{(-)}$ and $\mathbf{E}^{(+)}$) for each charges and the horizontal plane. E is the total vertical electric field intensity. Adapted from [*Rakov and Uman*, 2007].

$H_{\mathrm{N}} = 7\,\mathrm{km}$ and $Q_{LP} = 3\,\mathrm{C}$ at $H_{\mathrm{LP}} = 2\,\mathrm{km}$ and the result is presented in Figure 2.15. Both the contribution from every point charge and the total is presented. As you can see in Figure 2.15, the total electric field is negative nearby or beneath the thundercloud. This is caused by the lower positive charge Q_{LP}. As we increase r the electric field is positive due to the positive dipole structure and for large r the electric field decreases asymptotically towards zero.

It is difficult to measure the electric field intensity in a thundercloud. Bad weather conditions and unknown locations for the strongest electric field both in space and time are some of the difficulties. One of the biggest mysteries in atmosphere electricity science is that nobody has measured the electric field strong enough to match the theoretical magnitudes, estimated for a discharge to occur [*Dwyer and Uman*, 2014].

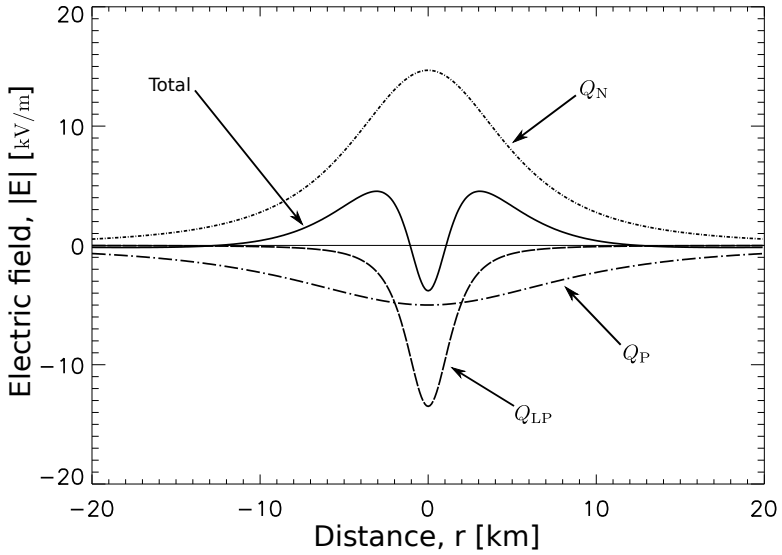

Figure 2.15: This plot shows the electric field strength in a distance r along sea level from the vertical charge axis in a tripole thundercloud model. The charge and height is given as $Q_{\mathrm{P}} = 40\,\mathrm{C}$ at $H_{\mathrm{P}} = 12\,\mathrm{km}$, $Q_{\mathrm{N}} = -40\,\mathrm{C}$ at $H_{\mathrm{N}} = 7\,\mathrm{km}$ and $Q_{\mathrm{LP}} = 3\,\mathrm{C}$ at $H_{\mathrm{LP}} = 2\,\mathrm{km}$. The total electric field is the algebraic sum of all components.

2.4.3 Electrical breakdown

Ionization and deionization are opposite processes where the number of electrons in a system respectively increases or decreases. In a given environment with a background electric field, as in a thundercloud, there is a competition between these processes [*Cooray*, 2003]. The relative efficiency ratio of ionization and deionization processes is dependent on the magnitude of the electric field. If the electric field magnitude exceeds a given value, called the breakdown electric field threshold, the electrical breakdown may occur. Qualitative analysis estimates this value to be $3.00 \cdot 10^4\,\mathrm{V/cm}$ [*Cooray*, 2003]. This is presented as the conventional breakdown field $E_{\mathrm{k}} \sim 32\,\mathrm{kV/cm}$ in Figure 2.16 [*Moss et al.*, 2006]. In this figure, the friction force of electrons in air at ground is plotted as a function of electron energy. This figure will be discussed more detailed later (see Section 2.5.2).

Electrical breakdown depends strongly on two conditions: (1) the electrical field has to be strong enough (in excess of the critical threshold) and (2) it has to be extended over a critical length. This critical length decreases with increasing field strength. The evolution and propagation of an electrical breakdown, will be more discussed in the section about streamer and leader processes (see Section 2.4.5).

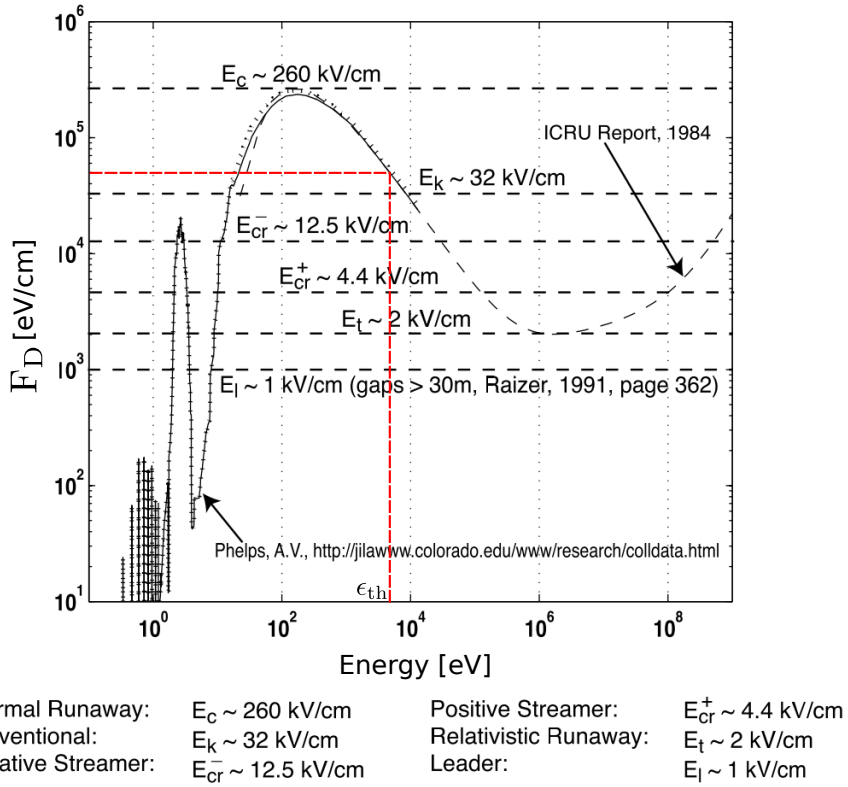

Figure 2.16: The dynamic friction force of electrons F_D in air at ground pressure is plotted as a function of electron energy. A solid line corresponds to a case when a total of 43 inelastic processes were accounted for corresponding to an air mixture of 78.11% N_2, 20.91% O_2 and .98% Ar gas using a set of cross sections compiled by A. V. Phelps, which excludes dissociation processes. A dotted line corresponds to a case which includes energy losses due to dissociation of N_2 and O_2 molecules. ϵ_{th} is used as an energy threshold in an example of run-away electrons in Section 2.5.2.1. Figure and text from *Moss et al.* [2006].

2.4.4 Thermal electron avalanche

If a free electron, at $x = 0$, in a gas is affected by an x-directed electric field, it will be accelerated in the direction of x. If the electric field is strong enough to give the electron at a certain distance as much energy as needed to ionize an atom due to collision, we will get two electrons. These two electrons will then be accelerated and collide into two new atoms. By this, the amount of electrons increases as x increases. The number of electrons n_x, at a given distance x, is given by:

$$dn = n_x(\alpha - \eta)\, dx, \tag{2.34}$$

where α is the number of ionizing collisions per unit length and η is the number of attachments per unit length.

The solution of Equation 2.34, is given by:

$$n_x = e^{(\alpha-\eta)x}. \tag{2.35}$$

As can be seen from Equation 2.35, the number of electrons in an electron avalanche increases exponentially with the distance x, if $\alpha > \eta$. An electron avalanche produces an electric field, due to charge separation. This charge separation is called space charge, and is important due to streamer theory (see Section 2.4.5).

2.4.5 Streamers and leaders

In a thundercloud where all electrical breakdown conditions are satisfied, we can get lightning discharges. Long sparks in range of 5 km to 10 km or 100 km in extreme [*Dwyer and Uman*, 2014], penetrate the potential gap. In this section we will discuss how these processes evolve, in terms of streamer and leader theory.

Most of the study of sparks is done in laboratories at much smaller scales than in nature. As already described, a short laboratory spark starts with a single electron that leads to an avalanche of electrons due to collision ionization. The avalanche grows, and charged particles get concentrated near the avalanche region. The increase in electron density affects the electrical field near the avalanche tip. When the local electrical field reaches the electrical breakdown threshold in this region, the avalanche is converted to a streamer discharge. In a small gap, the streamer may bridge the whole gap itself. If the gap is longer, as in a thundercloud, a lot of streamers may start from the electrode with a mutual streamer stem. In this streamer stem there is a current flowing that increases the temperature. The conductivity in the streamer stem is increasing, due to higher temperature. If the temperature surpasses a critical temperature, the streamer stem may be converted to a leader. Due to large conductivity in the leader, the electric potential at the electrode will now be transferred to the leader tip, where new streamers may be produced. We observe both positive and negative steamers/leaders.

2.4.5.1 Formation of positive streamers

Positive streamers propagate from the positive charge region, the anode, towards the negative charge region, the cathode, in a thundercloud or in a spark laboratory. The electron avalanche is attracted towards the anode and results in an excess of positive space charges at the avalanche head. The space charge sets up an electric field in this region. When the avalanche hits the anode, the negative charge will be absorbed and leaved behind the positive net charge. Energetic photons are produced in the avalanche head due to the recombination of positive ions and electrons. These photons produce new secondary avalanches near by the positive space charge.

The number of positive ions depends on the electric field intensity in the space charge region. If this number exceeds a critical value, this field is comparable to the background electric field. A consequence of this is that secondary avalanches are attracted towards the positive space charge of the primary avalanche, then neutralized and leaved behind a new positive space charge. This process repeats itself and when new positive space charges are produced, the positive streamer propagates towards the cathode. See Figure 2.17 for a schematic diagram of the formation of a positive streamer.

2.4.5.2 Formation of negative streamers

Negative streamers propagate from the cathode to the anode, the opposite way of a positive streamer. The electrons in the avalanche move into the gap, away from the expanding channel. They are leaving behind positive charge close to the cathode. Energetic photons produced by recombination of positive ions and electrons, produces secondary avalanches. As the primary avalanche grows, the number of positive ions increases. If this number exceeds a critical value, the electric field produced by the space charge is comparable to the background electric filed. Then secondary avalanches extend the space charge and a positive channel is set up between the cathode and the avalanche region. This channel reaches the cathode and knocks out electrons from the cathode. These electrons will neutralize the space charge and make a weak conducting channel between the cathode and the avalanche head. Because of this conducting connection, a strong electric field is set up at the avalanche head, as a "new" cathode. This cathode pushes the negative space charge further away into the gap, while the positive space charge is neutralized by electrons from the cathode that connects the avalanche head with the cathode. See Figure 2.18 for a schematic diagram of the formation of a negative streamer.

2.4.5.3 Leaders

In long sparks, as lightning in thunderclouds, a streamer does not bridge the gap in itself. Even in a laboratory experiment with a potential difference in range of mega volt, a streamer in air does not propagate longer than a meter. The streamers are created in the head of a long and high conductive leader that propagates step-wise through the gap. The region where the streamers operate is called the streamer zone, located in front of the leader tip. As much as 10^6 streamers can be formed in a volume of some cubic meters [*Skeltved*, 2013]. This is called a corona flash. Streamers convert cold gas to hot and dense plasma. Without this plasma it would have been unable to transport a significantly amount of charge into the gap. The plasma temperature in the leader channel is in range of 5 000 K to 10 000 K, hot and conductive [*Bazelyan and Raizer*, 2000].

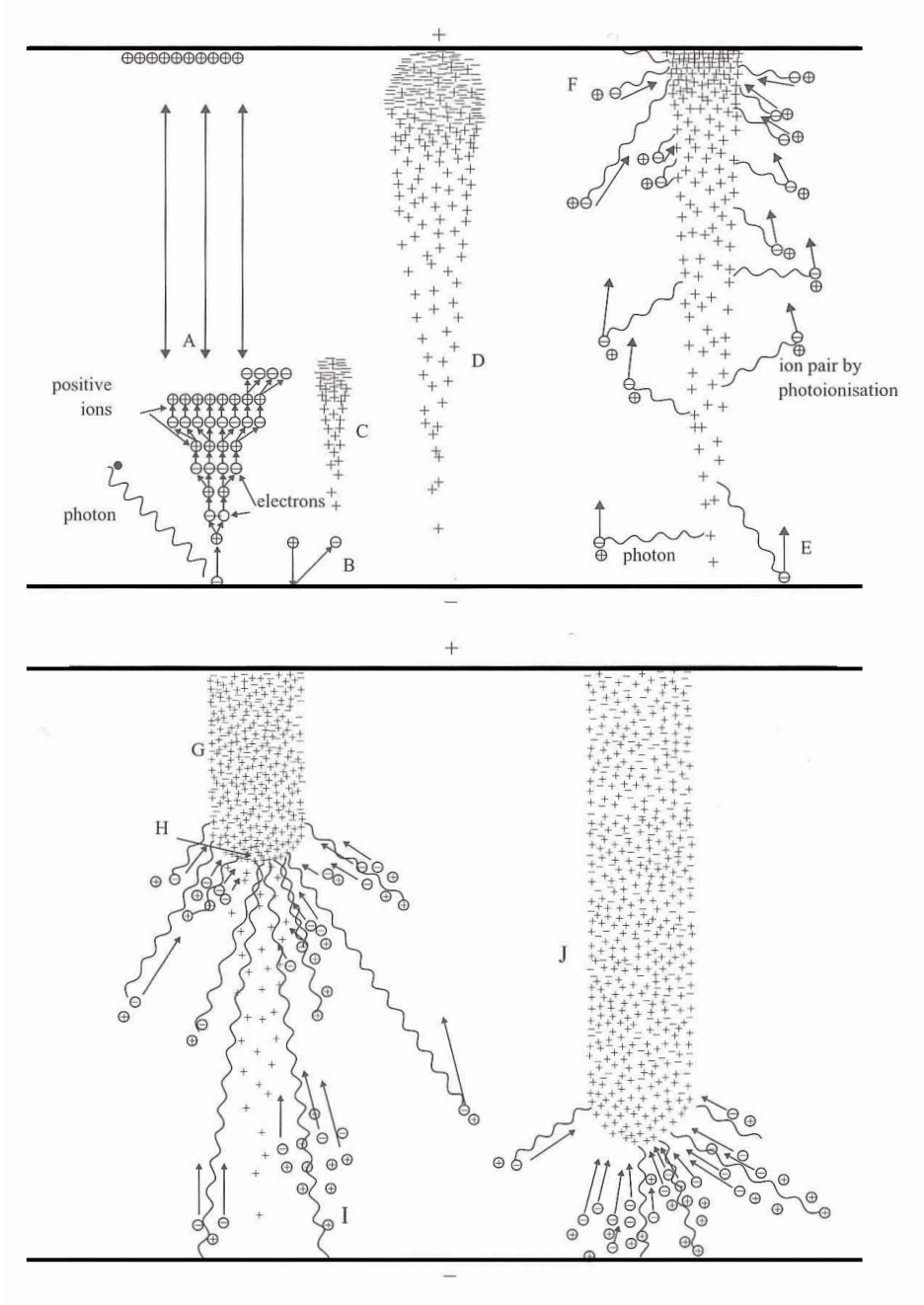

Figure 2.17: Schematic diagram showing the formation of a positive streamer. A: an external photon triggers an avalanche. B: a positive ion strikes the cathode and starts an avalanche C. D: the avalanche tip reaches the anode. E: photons originating from the avalanche produce free electrons both from the cathode and in the gas. F: the positive space charge close to the anode increases the electric field and a streamer is just about to be formed. G: plasma of positive ions and electrons forms the streamer channel. H: streamer tip. I: production of free electrons by photons. J: streamer close to the cathode. Figure and text from *Cooray* [2003].

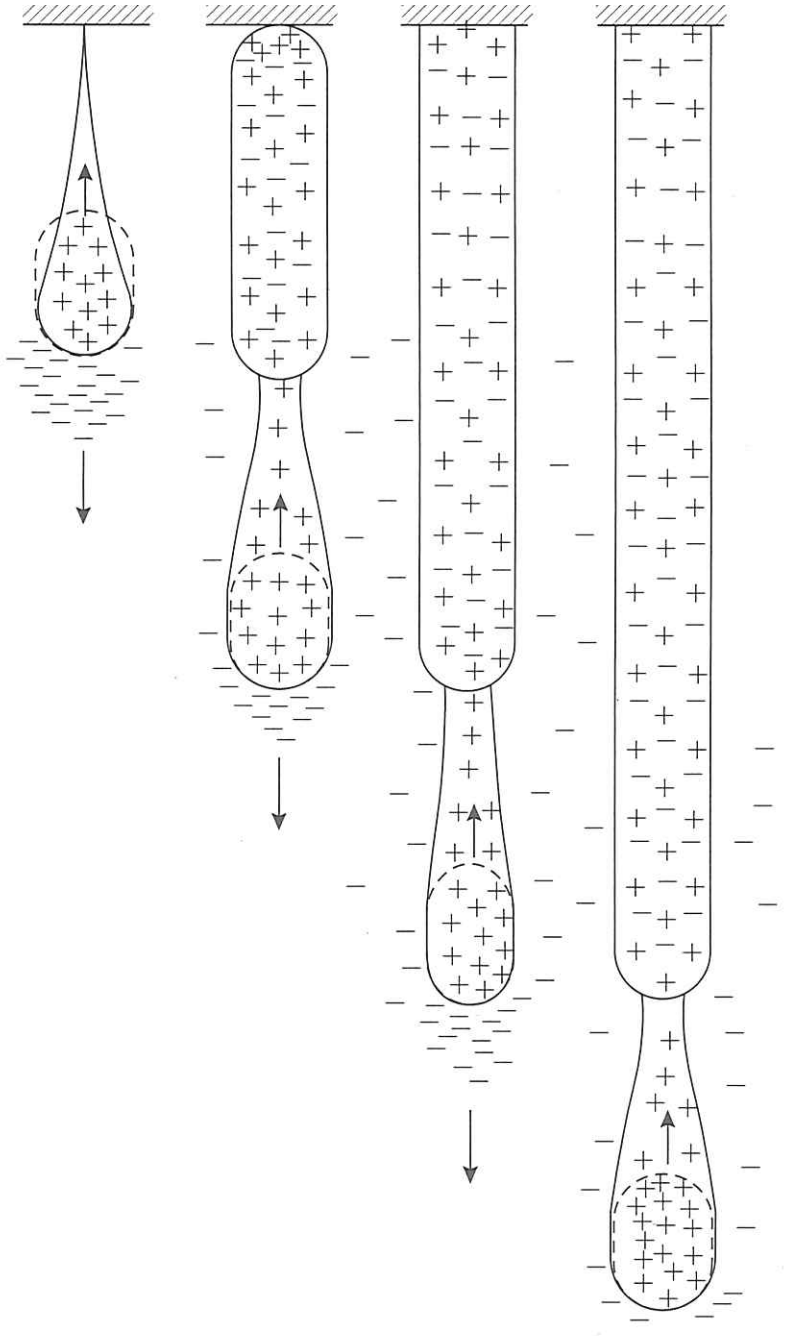

Figure 2.18: Schematic representation of the formation of a negative streamer and the physical processes taking place at the streamer head. Figure and text from *Cooray* [2003].

2.4.6 Types of lightning

Lightning discharges can be divided into two different categories: (a) lightning that propagate through the gap between the thundercloud and the Earth's surface and (b) lightning that propagate between charge layer in the cloud or between clouds. The first group is called (1) cloud-to-ground lightning and the second group is a collection of (2) cloud-to-cloud (intercloud), (3) lightning within a single thundercloud or cell (intracloud) and (4) cloud-to-air lightning. All these four different kinds of lightning can be seen in Figure 2.19. In Figure 2.19 you can also see the charge distribution in a thundercloud versus temperature, which is correlated to the altitude (see Section 2.4.1). It is important to notice that a thundercloud is much more complex than shown in Figure 2.19. It is different from thundercloud to thundercloud. The main negative and main positive charge center can be located at different altitudes and other charge centers can be present. What kind of lightning we may observe, presented in Figure 2.19, is also simplified, e.g. cloud-to-air lightning could be discharge from the negative part of the cloud, not only from the positive [*Dwyer and Uman*, 2014].

By convention, the positive direction of a lightning stroke is defined as a positive leader propagating downwards, towards the Earth' surface. This means that a negative leader that propagates upward, is defined as positive. This convention is used in the next sections.

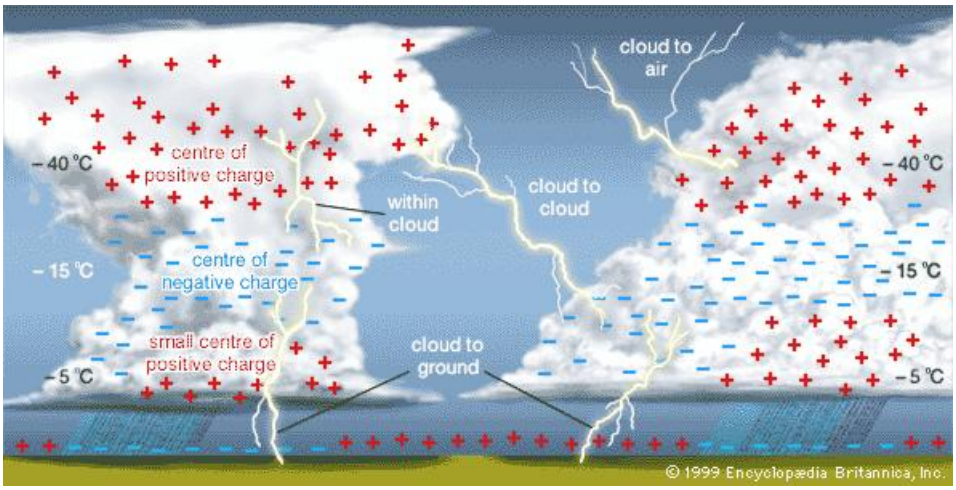

Figure 2.19: Charge distribution in two thunderclouds where cloud-to-ground (CG), intracloud (IC), intercloud (CC) and cloud-to-air lightning do occur. Figure from *Encyclopædia Britannica* [2007] and *Dwyer and Uman* [2014].

2.4.6.1 Cloud-to-ground lightning - CG^{+-}

Cloud-to-ground lightning is a discharge between the ground and a thundercloud. There are four categories of cloud-to-ground lightning, as you can see in Figure 2.20. About 90% of all cloud-to-ground lightning are initiated by a negatively charged leader that propagates downward, as can be seen in Figure 2.20a. This leader propagates from the main negative charge region in the middle of the cloud, carrying negative charge (negative leader) and propagates towards an induced positively charged ground. By the convention this is defined as CG^{-}. If the lower positive region is presented in the cloud, then the negative lightning penetrates and neutralizes some of the positive charges and then continues down to the Earth.

The opposite situation is when a positive leader propagates upwards from a positively charged ground, towards the negative charge center in the middle of the cloud. This is shown in Figure 2.20b. By the convention, this is also defined as CG^{-}.

Another type of cloud-to-ground lightning is when a downward positive leader propagates from the main positive charge region in the cloud towards the Earth (CG^{+}), as can be seen in Figure 2.20c. This one represents about 10% of all cloud-to-ground lightning [*Dwyer and Uman*, 2014]. The last one, presented in Figure 2.20d, is a negative leader carrying negative charge from a negatively charged ground towards the main positive charge region in the cloud (CG^{+}). Both leaders presented in Figure 2.20c and 2.20d are much less common than those presented in Figure 2.20a and 2.20b.

2.4.6.2 Intracloud lightning - IC^{+-}

A misconception is often that all lightning is formed between a thundercloud and the Earth's surface. The most common type of all lightning discharges is intracloud lightning, where the discharge occur between the positive and the negative charge region in one cell. Upward intracloud lightning (IC^{+}) is thought to be the most important discharge according to TGF production [*Briggs et al.*, 2010].

2.4.6.3 Cloud-to-cloud lightning - CC^{+-}

In cloud-to-cloud lightning, or intercloud lightning, the discharge occurs between an actual charge region in one thundercloud and the opposite charge region in another thundercloud. Another type of discharge is when a discharge occurs between a charge region in a thundercloud and the air around the cloud. This is called cloud-to-air lightning [*Dwyer and Uman*, 2014] and can be seen schematically in Figure 2.19.

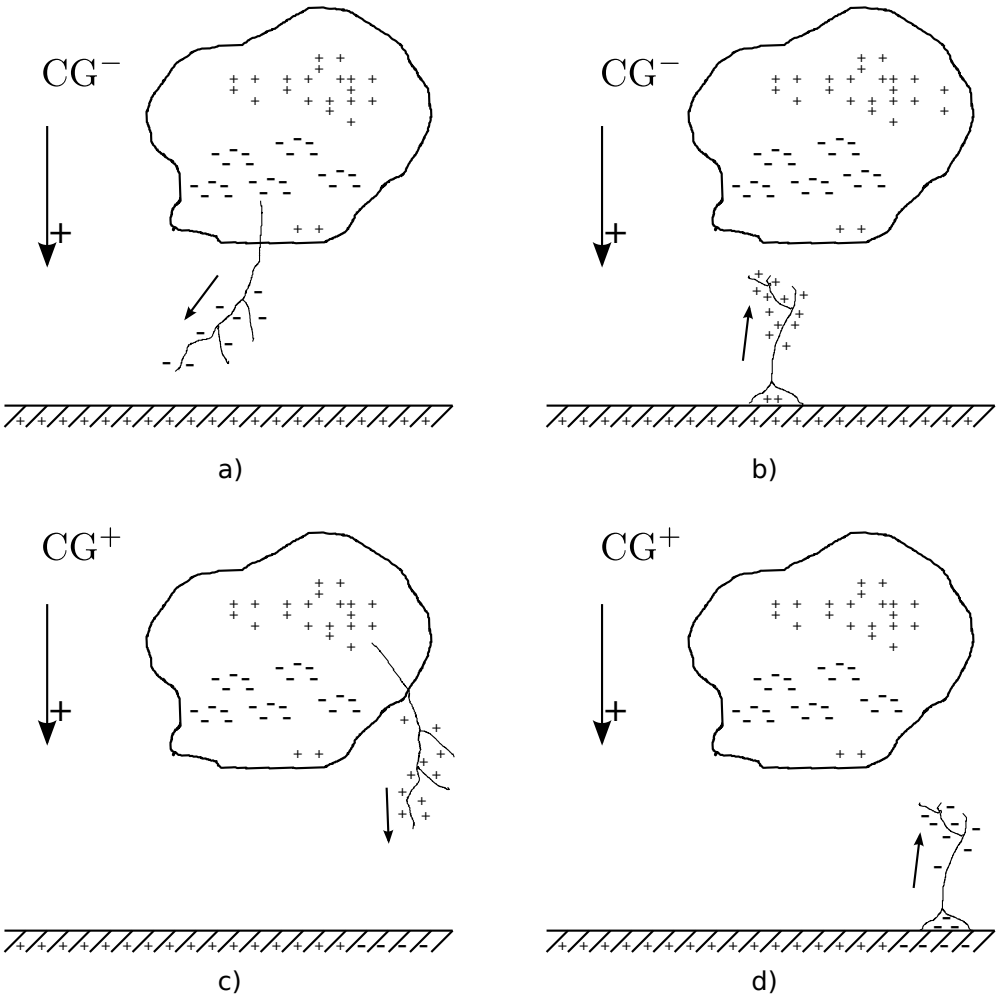

Figure 2.20: Four types of cloud-to-ground discharges. a) A negative leader propagating from the negative charged region in a thundercloud towards a positive ground (CG^-). b) A positive leader propagates from a positive ground towards the negative charge region in a thundercloud (CG^-). c) A positive charged leader propagates from the positive main charged region in a thundercloud towards a negative induced ground (CG^+). d) A negative leader propagates from an induced negative ground towards the positive region of a thundercloud (CG^+). Adapted from *Dwyer and Uman* [2014] and *Berger* [1978].

2.4.7 Radio waves emitted from lightning

Lightning return strokes emit electromagnetic waves in a broad frequency spectrum, from a few Hertz to gigahertz. Most all of the emitted energy is in the Extremely Low Frequency band (ELF: 3 Hz to 3 kHz) and the Very Low Frequency band (VLF: 3 kHz to 30 kHz). Due to these low frequencies, the propagation loss is just a few decibels per megameter and makes it possible for those waves to propagate long distances. Electromagnetic waves emitted from lightning strokes are called sferics, whistlers and tweeks and can propagate between the Earth's surface and the D-layer in the ionosphere, as can be seen in Figure 2.21. This propagation is called the Earth-Ionosphere Waveguide (EIWG), where the wave can be reflected both in the D-region of the ionosphere and the Earth's surface, or propagate along the line of sight between a source and a receiver.

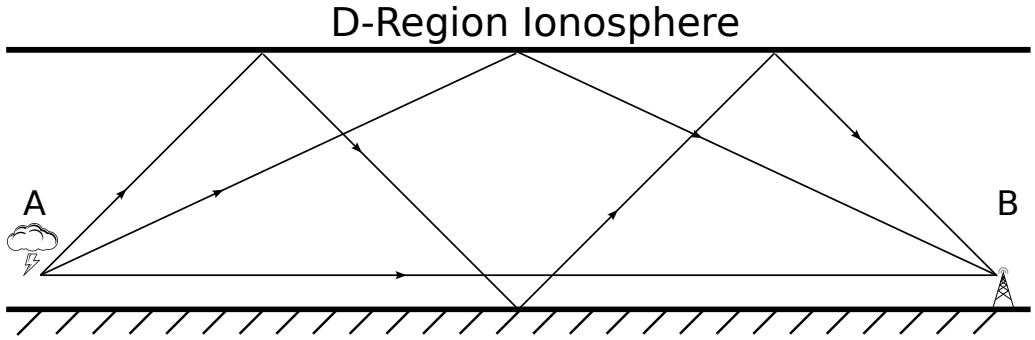

Figure 2.21: VLF propagation in the Earth-Ionosphere Waveguide (EIWG). Point A is a VLF source, e.g. a lightning stroke, and point B is a VLF receiver. Adapted from *Khairul et al.* [2011].

The refractive index n_r of an electromagnetic wave propagating towards the ionosphere, or in general in a magnetized plasma including collisions, is given by the Appleton-Hartree equation:

$$n_\mathrm{r}^2 = 1 - \frac{X(1-X-iZ)}{(1-iZ)(1-X-iZ) - \frac{Y^2 sin^2\theta}{2} \pm \sqrt{Y^2 cos^2\theta\,(1-X-iZ)^2 + \frac{Y^4 sin^4\theta}{4}}}, \tag{2.36}$$

where θ is the angle between the propagation direction and the external magnetic field vector. X, Y and Z is given by:

$$X = \left(\frac{\omega_\mathrm{p}}{\omega}\right)^2, \quad Y = \frac{\omega_\mathrm{ge}}{\omega}, \quad Z = \frac{\nu_\mathrm{e}}{\omega}, \tag{2.37}$$

where ω_p is the angular plasma frequency, ω_ge is the angular electron gyro frequency, ω is the angular wave frequency and ν_e is the electron collision frequency. If we

neglect the effects of the Earth's magnetic field and of collisions, Equation 2.36 can be reduced to:

$$n_{\mathrm{r}}^2 = 1 - X. \tag{2.38}$$

The wave reflects in the ionosphere when n_{r} is equal to zero, e.g. when X is equal to one. This happens when the wave frequency ω is equal to the plasma frequency ω_{p} (see Equation 2.37).

VLFs propagate almost at the speed of light and because of their long propagation range, it is possible to detect global lightning activity with a relatively small number of antennas. This is why VLFs are important for this thesis and will be more discussed in Section 3.2 about the World Wide Lightning Location Network (WWLLN).

2.5 High energy atmospheric physics

In this section we will focus on certain aspects of high energy atmospheric physics that are relevant for the study of Terrestrial Gamma-ray Flashes (TGFs) and Terrestrial Electron Beams (TEBs). Other phenomena, e.g. Transient Luminous Events (TLEs): sprites, elves and blue jets, are outside the scope of this thesis.

2.5.1 Historical introduction

High energy atmospheric physics was established as a field of physics in 1925 with C.T.R. Wilson's study of accelerating charged particles in strong electric fields [*Wilson*, 1925]. Wilson was especially interested in electric fields in thunderclouds. One can say that this was the cradle for the study of Terrestrial Gamma-ray Flashes and Terrestrial Electron Beams.

Fishman et al. [1994] was the first to report observation of gamma-rays at high altitudes in the atmosphere. A hard photon spectrum with a peak in the high energy region, consistent with Bremsstrahlung produced by electrons in the range of MeV, was observed. The discovery was done by The Burst and Transient Source Experiment (BATSE). BATSE is an instrument aboard at Compton Gamma-Ray Observatory (CGRO). These events were first believed to be related to the newly discovered TLEs, high up in the atmosphere. *Fishman et al.* [1994] estimated the origin of these flashes to be above at least 30 km, because they believed that X-rays lower than that could not propagate out of the atmosphere. As late as 2000, it was not fully accepted that lightning was emitting energetic radiation. It was thought that TGFs were generated in about 70 km height correlated to sprite discharges [*Dwyer and Uman*, 2014; *Gurevich et al.*, 1992; *Pasko*, 2010; *Roussel-Dupre and Gurevich*, 1996].

Smith et al. [2005] observed TGFs with energies up to 20 MeV with the Reuven Ramaty High Energy Solar Spectroscopic Imager (RHESSI) satellite. These events were, by their energy spectrum, estimated to have their origin in a much lower part of the atmosphere (< 21 km) than *Fishman et al.* [1994] thought earlier [*Dwyer*, 2008]. *Marisaldi et al.* [2010] detected TGFs with the Mini-Calorimeter (MCAL) instrument at Astrorivelatore Gamma a Immagini Leggero (AGILE) satellite with energies up to 40 MeV.

BATSE, RHESSI and the Gamma-ray Burst Monitor (GBM) instrument aboard The Fermi Gamma-ray Space Telescope have detected TEBs, but a lot rarer than for TGF events. TEB observations are presented in Section 2.5.4.1.

2.5.2 Runaway electron generating mechanisms

Since the discovery of the TGFs in 1994, the production mechanisms of these energetic particles have remained a mystery [*Dwyer*, 2008]. The mystery is complex and raises many unanswered questions. Why do lightning emits particles and radiation with so high energies? Where and when in the lightning process do this occur? Does it affect the atmospheric composition? Is the radiation dangerous for airplane passengers? To answer questions like these, it is important to study the mechanisms of how electrons can gain such high energies.

2.5.2.1 Wilson's runaway electrons

The runaway electron, discovered by *Wilson* [1925], is the main component in high energy atmospheric physics. Consider an electric field in an atmospheric gas. If the average rate of energy gain due to the electric field is greater than the average rate of energy loss in the system, then runaway electrons can reach high energies [*Dwyer and Uman*, 2014]. This energy loss is dominated by ionization and excitation processes for relativistic electrons below some tens of MeV (see Section 2.3.3.1 and Equation 2.19). For higher energies, Bremsstrahlung processes are also important. The energy loss per unit length for a minimum ionizing 1 MeV electron is $f_{\min} = 2.18\,\mathrm{keV/cm} \times n_{\mathrm{air}}$ [*Bethe and Ashkin*, 1953], where n_{air} is the relative air density.[1] An electric field $E_{\mathrm{t}} = 2.18\,\mathrm{kV/cm} \times n_{\mathrm{air}}$ will then gain the same amount of energy per unit length, eE_{t} (see Equation 2.3), as the minimum energy loss per unit length due to ionization. This is referred to the brake even field plotted as a horizontal dashed line at $E_{\mathrm{t}} \sim 2\,\mathrm{kV/cm}$ in Figure 2.16.

We will now discuss two situations, where E is the electric field, E_{t} is the break

[1] Air density relative to air density at sea-level at standard conditions for temperature and pressure (STP)

even field, described above, and $\mathrm{d}\epsilon = (eE - f_{\min})\,\mathrm{d}z$ is an expression of the change in energy:

1. $E < E_{\mathrm{t}}$: The change of energy is less than zero, $\mathrm{d}\epsilon < 0$, which means that the electron slows down and get lost.

2. $E > E_{\mathrm{t}}$: The change of energy is greater than zero, $\mathrm{d}\epsilon > 0$, which means that the electron gains energy from the electric field and "run away".

In Figure 2.16 the energy loss per unit length for an electron or a positron is plotted as a function of kinetic energy for electrons in air. Consider an electron that experience a friction force due to a strong electric field of 50 keV/cm. For an electron to "run away", the initial electron energy must be above an energy threshold ϵ_{th} [*Dwyer and Uman*, 2014], represented as a red dashed line in Figure 2.16. If the electric field E, is greater than a critical value E_{c}, which is above the friction curve for all kinetic energies, all free electrons may run away. This is called thermal runaway. A typical value of E_{c} is $\sim 260\,\mathrm{kV/cm}$ [*Moss et al.*, 2006]. Since the conventional breakdown field of air is $E_{\mathrm{k}} \sim 32\,\mathrm{kV/cm}$ (see Section 2.4.3), fields of this strength will not be maintained for a long time in a thundercloud. Fields of the E_{c} strength is more correlated to streamer tips in the end of lightning leaders (see Section 2.4.5) [*Celestin and Pasko*, 2011; *Dwyer and Uman*, 2014; *Moss et al.*, 2006].

2.5.2.2 Relativistic Runaway Electron Avalanches (RREA)

This avalanche process is built on Wilson's runaway electrons and describes how to get an avalanche of runaway electrons. The Relativistic Runaway Electron Avalanche (RREA) process was first described in detail by *Gurevich et al.* [1992], where it was presented in a way of how this could affect thunderstorm phenomena. The process is dependent on initial energetic seed electrons to start the avalanche. Secondary electrons from cosmic rays have been the most common model for initial electrons. These initial electrons do interact with atomic electrons via hard elastic Møller scattering (see Section 2.3.2.1) [*Dwyer*, 2008]. Some of the scattered atomic electrons get energies above the threshold energy ϵ_{th}, and do "run away" along with initial energetic electrons. The production of electrons increases exponential with time and distance [*Dwyer and Uman*, 2014] and is of course dependent on the flux of initial seed particles. To generate relativistic electron avalanches, the electric field threshold must exceed $E_{\mathrm{t}} \sim 2\,\mathrm{kV/cm}$, which can be seen in Figure 2.16 [*Coleman and Dwyer*, 2006; *Dwyer*, 2003; *Moss et al.*, 2006].

The number of runaway electrons $N(Z)$ a distance Z from the start of the avalanche, is given by:

$$N(Z) = N_0 e^{\frac{Z}{\lambda}}, \tag{2.39}$$

where N_0 is the number of initial electrons and λ is the avalanche length, defined as the distance electrons must travel to increase the number of runaway electrons by factor e. The avalanche length λ, for relativistic runaway electrons is empirical approximated as:

$$\lambda = \frac{7300\,\mathrm{kV}}{[E - 276\,\mathrm{kV/m} \times n/n_0]}. \tag{2.40}$$

This approximation is valid in the energy range of $E = 300\,\mathrm{kV/m}$ to $E = 3\,000\,\mathrm{kV/m}$.

Consider a uniform electric field E over an avalanche length λ. The maximum kinetic energy $\Delta K_{\max}$, that an electron can get over this avalanche length λ, is given by:

$$\Delta K_{\max} = [eE - f_{\mathrm{d}}\, n/n_0]\lambda, \tag{2.41}$$

where $e = 1.6 \cdot 10^{-19}\,\mathrm{C}$ is the electron charge, f_{d} is the energy loss per unit length, and n/n_0 is the ratio between the air density and the STP air density. *Dwyer* [2004] has performed detailed Monte Carlo simulations of RREA, using a runaway electron distribution function above 1 MeV. Then the energy loss per unit length is $f_{\mathrm{d}} = 270\,\mathrm{keV/m}$.

By combining Equation 2.40 with Equation 2.41, the maximum energy gained to the electron can be calculated. Due to the simulation parameters given above, this maximum energy over one avalanche length is 7 MeV [*Dwyer*, 2008]. This means that for a 20 MeV TGF, more than three relativistic electron avalanche lengths is required, if this process works alone. The energy distribution $N(\epsilon)$ is given by:

$$N(\epsilon) = \frac{1}{\epsilon} N_{\mathrm{RREA}} e^{-\alpha}, \tag{2.42}$$

where ϵ is the energy, N_{RREA} is the flux of electrons and α is the ratio between the energy ϵ and the mean energy $\bar{\epsilon}$ of the runaway electrons [*Skeltved*, 2013].

According to *Dwyer* [2008], if RREA should be the sole mechanism generating runaway electrons, a flux of initial seed electrons would have to be $5 \cdot 10^9 \mathrm{m}^{-2} \cdot \mathrm{s}^{-1}$.[2] This flux is about 500 000 times larger than the maximum flux of atmospheric cosmic rays and other background radiation, which is $10^4\,\mathrm{m}^{-2} \cdot \mathrm{s}^{-1}$. Monte Carlo simulations of runaway electron trajectories in a thundercloud has been performed by *Dwyer et al.* [2010] and is presented in Figure 2.22.

The thermal electron avalanche process was described in Section 2.4.4. A difference between these two processes is the length scale. RREA do occur on a scale of tens of hundreds of meters, in contrast to sub-millimeter scales for the thermal electron avalanche [*Dwyer and Uman*, 2014].

[2]Estimated by three RREA lengths and cross sectional area of $100\,\mathrm{km}^2$

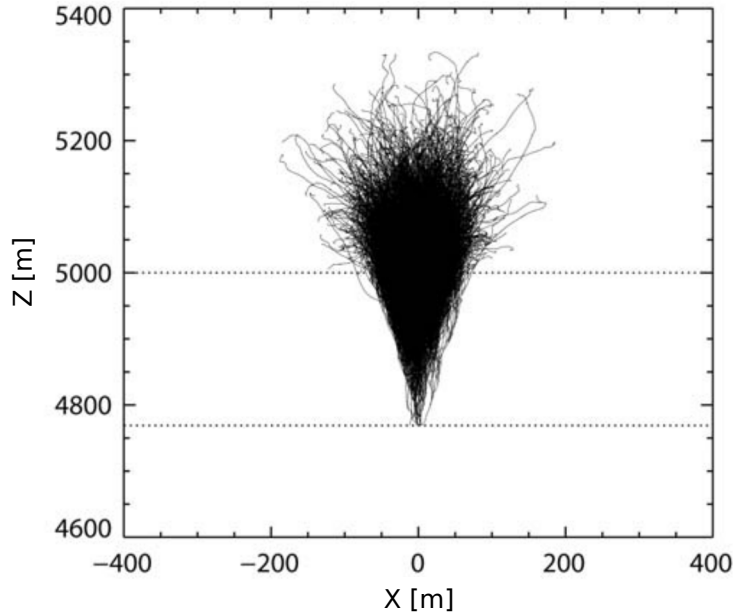

Figure 2.22: The result of Monte Carlo simulations of runaway electron trajectories in a thundercloud at 5 km altitude. A 375 kV/m uniform electric field is set up between the dotted lines. It all was initiated by 10 energetic electrons in the bottom of the electric field region. Figure from *Dwyer et al.* [2010].

2.5.2.3 Relativistic feedback mechanism

Dwyer [2003] built upon the RREA work done by *Gurevich et al.* [1992] and introduced a new mechanism. The relativistic feedback mechanism takes both the Wilson's runaway electrons [*Wilson*, 1925] and RREA into account. In RREA the electrons interact via Møller scattering. In the feedback mechanism, *Dwyer* [2003] adds Bhabha scattering (see Section 2.3.2.1) to his model. A consequence by introducing this, is that gamma and/or positron feedback is possible.

Energetic seed electrons may produce Bremsstrahlung (see Section 2.3.3.1), in the form of X-rays. These X-rays may be back scattered via Compton scattering or pair-produce pairs of electrons and positrons (see Section 2.3.4.2 and 2.3.4.3).

Monte Carlo simulations have been performed by several scientists, e.g. *Dwyer* [2003] built on *Lehtinen et al.* [1999] and *Babich et al.* [2005]. Figure 2.23 shows a visualization of simulations done by *Dwyer* [2003]. In this simulation a uniform electrical field of 1 000 kV/m pointing upwards is used, ranging over a horizontal distance of 200 m and marked with dotted lines in the figure. A seed electron of 1 MeV is injected at the top center of the volume and initiates an avalanche of electrons, marked with light trajectories. To the right in Figure 2.23, positron feedback is shown. A gamma-ray, dashed line, produces an electron-positron pair.

The positron runs away and produces more runaway electrons on its way, via Bhabha scattering. This part of the mechanism is called positron feedback. Because of high kinetic energy, this positron can propagate many hundreds of meters, before it annihilates.

To the left in Figure 2.23 a dashed line represents a gamma-ray that propagates upwards. This gamma-ray produces new seed electrons through Compton scattering and photoelectric absorption (see Section 2.3.4.1 and 2.3.4.2) [*Dwyer*, 2003].

In higher electric field strengths (e.g. $E > 750\,\mathrm{kV/m} \times n_{\mathrm{air}}$), Monte Carlo simulations show that gamma feedback dominates, but for lower electric filed strengths positron feedback dominates. This is due to different avalanche lengths for different processes.

According to *Dwyer and Uman* [2014], the Relativistic feedback mechanism generates up to trillions of times the amount of runaway electrons produced by RREA alone. This is why feedback is a feasible mechanism for e.g. Terrestrial Gamma-ray Flashes.

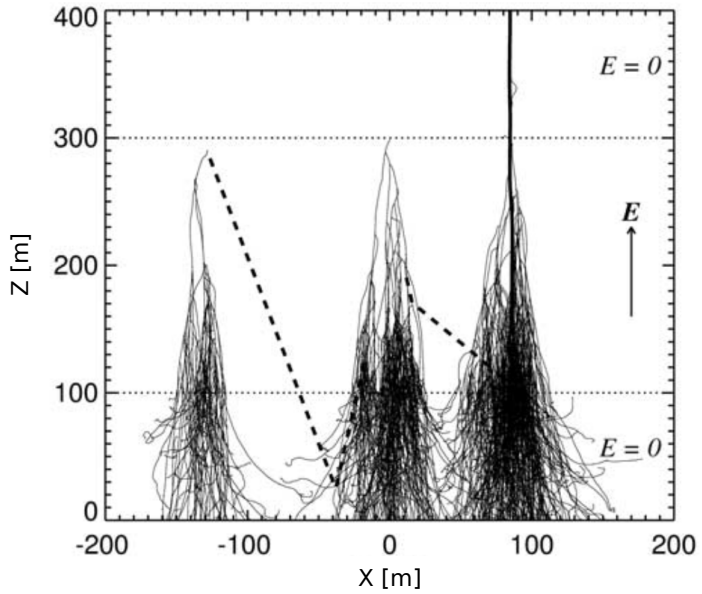

Figure 2.23: Monte Carlo simulation of Relativistic Runaway Electron Avalanches (RREA) and relativistic feedback mechanism. Initiated by a 1 MeV seed electron at the top center of the electric field region. The electric field between the dotted horizontal lines has a field strength of 1 000 kV/m. The avalanches on the left and right illustrate the gamma-ray feedback and positron feedback mechanism, respectively. Figure from *Dwyer* [2003]

.

2.5.3 Terrestrial Gamma-ray Flashes (TGFs)

In Section 2.5.1 an historic overview was presented. The goal of these sections is to give an idea of what scientists know about TGFs today. When first discovered, TGF was thought to be a high atmospheric phenomenon, but this paradigm has been changed. Observations, mechanisms and models show that such energetic processes do occur in the height of the discharge process itself.

TGFs are brief pulses with a typical duration of less than 1 ms. According to *Smith et al.* [2010], the average duration of all TGFs in the RHESSI catalog is in range of ~ 0.6 ms to ~ 0.7 ms, but now ~ 0.3 ms is more established. Observed TGFs have an energy spectrum $\propto 1/\mathrm{E}$, where the energy per photon is up to several tens of MeV [*Gjesteland et al.*, 2012; *Marisaldi et al.*, 2010; *Smith et al.*, 2005]. More about TGF mechanisms and observations are presented in Section 2.5.1 and 2.5.2.

2.5.4 Terrestrial Electron Beams (TEBs)

TGFs were thought to be produced in the higher parts of the atmosphere. Scientists believed that only X-rays from this altitude could by itself propagate out of the atmosphere. As the atmospheric density exponentially decreases with height, $n \approx \exp(-z/8.5\,\mathrm{km})$, X-rays in an altitude of 70 km could escape into space and be detected by orbiting satellites. As the sources of TGFs are thought to be in an altitude < 21 km [*Dwyer et al.*, 2008], the case is different. TEB observations, mechanisms and simulations are presented in this section.

2.5.4.1 TEB observations

Dwyer et al. [2008] discovered the first TEB in a re-analyzing study of the CGRO/BATSE data (see Figure 1.1). The number of observed TEBs is much less than for TGFs. In Table 2.2, 13 TEBs are presented. The GBM instrument at FERMI has detected 15 TEBs in total per 2015 [Michael Briggs, personal communication, March 27, 2015], 6 events are published and presented in Table 2.2. The third event in Table 2.2, identified as 091214.495, can be seen in Figure 2.24. The duration of the events is ranging from 1.5 ms to 30 ms. Those 6 GBM TEBs satisfy several of the following characteristics: a duration longer than 1 ms, a positron annihilation 511 keV line in the energy spectrum, a spectrum with a lower maximum energy, WWLLN activity in one of the magnetic foot points, no WWLLN activity beneath the satellite and that Fermi just measure signals on one side of the satellite [*Xiong et al.*, 2012].

The first three TEB observations are in detail described in *Briggs et al.* [2011]. The 080807.357 beam was consisting of 2.3 MeV electrons (E_0) and the positron fraction

Table 2.2: TEBs detected by GBM, RHESSI and BATSE [*Xiong et al.*, 2012]

Instrument	Id.	Date (yymmdd)	Lon. (deg.)	Lat. (deg.)	Duration (ms)	B-line length (km)
GBM	080807.357	080807	253.01	15.30	2.5	764
GBM	090813.215	090813	278.29	-2.19	4	1198
GBM	091214.495	091214	34.42	25.34	30	5493
GBM	100515.316	100515	278.29	-0.98	5	1124
GBM	110410.216	110410	286.38	0.15	2.2	1125
GBM	110625.474	110625	111.01	14.47	6	1216
RHESSI	-	040117	21.119	20.535	30	3797
BATSE	01470	920309	128.31	28.18	20	6371
BATSE	02221	930305	28.44	28.46	25	6294
BATSE	02248	930315	18.58	-3.03	< 10	720
BATSE	02457	930723	110.33	28.37	4	620
BATSE	07208	981111	119.44	14.45	1.5	1095
BATSE	07229	981125	177.04	-9.03	2	867

was 0.099 ± 0.022. This was a short event with duration of 2.5 ms and field line length of 764 km. The 090813.215 beam was consisting of 4.6 MeV electrons (E_0) and the positron fraction was 0.34 ± 0.08. This was also a short event, but a bit longer than the first one, with duration of 4 ms and field line length of 1198 km. The 091214.495 beam was consisting of 3.0 MeV electrons (E_0) and the positron fraction was 0.19 ± 0.02. This was a long, multi-mirroring peak, event with duration of 30 ms and field line length of 5493 km.

Cohen et al. [2010] presented the first TEB linked to its causative lightning discharge. The TEB was observed by Fermi GBM (Id.:100515.316) and the sferics were detected by the GLD360 network. The first electrons arrived at the spacecraft at $07 : 35 : 05.79585\,\mathrm{UTC} \pm 0.25\,\mathrm{ms}$. $\sim 75\,km$ from the northern foot point a lightning stroke was detected at $07 : 35 : 05.7920\,\mathrm{UTC} \pm 0.05\,\mathrm{ms}$, ~ 4 ms before Fermi detected the signal. The length of the magnetic field line corresponds to a speed-of-light propagation delay of ~ 3.77 ms, which is consistent with the time between the GLD360 and the Fermi GBM detection.

Carlson et al. [2009] have in their study found ~ 50 TEB candidates in 8 years of SAMPEX data (between August 7, 1996 and June 30, 2004), but these are not compared to lightning data yet.

2.5.4.2 TEB mechanism

Modeling shows that runaway electrons produced deep in the atmosphere is absorbed, due to interactions with air molecules. This happens immediately once they leave the strong electric field region in the thundercloud [*Dwyer and Uman*, 2014].

In 2004 Fermi detected particles over the Sahara Desert that at first was thought to be a usual TGF. As can be seen in Figure 2.24, it was a long multi peaked event with duration of about 30 ms. Fermi's time tag and position was compared to weather data in the actual area and time period, but there were no thunderstorms beneath the satellite. At the conjugate foot point of the geomagnetic field line that the satellite passed through, on the other hand, there were thunderstorms (see the left part of Figure 2.24).

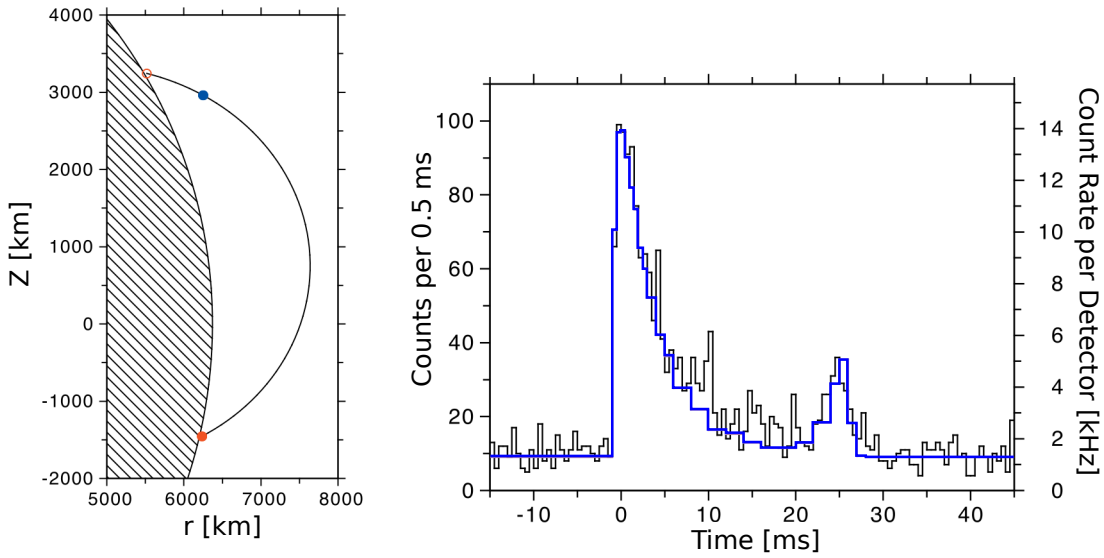

Figure 2.24: FERMI observation of TGF 091214. (left) The Earth and the actual magnetic field line plotted with the FERMI position (blue dot) and the magnetic foot points. (right) Black histogram: GBM particle counts summed over all 14 detectors (TGF 091214). Magenta histogram: Monte Carlo simulation of TGF 091214. Figure from *Briggs et al.* [2011].

Dwyer et al. [2008] suggested a mechanism for TEBs. This mechanism is built on a concept where it is not the runaway electrons that escape the atmosphere, but secondary electrons produced by gamma-rays. The runaway electrons produce gamma-rays via Bremsstrahlung (see Section 2.3.3.1 and 2.5.3). These gamma-rays interacts via Compton scattering and pair production (see Section 2.3.4.2 and 2.3.4.3) and produces TEBs. In an altitude of about 40 km the air is dense enough

for gamma-rays to interact with air molecules, but still not so dense that it allows the secondary electrons to escape. It is then possible for the secondary electrons to escape out of the Earth's atmosphere, into space. The process where a pair of electron and positron is produced is schematically presented in Figure 2.25.

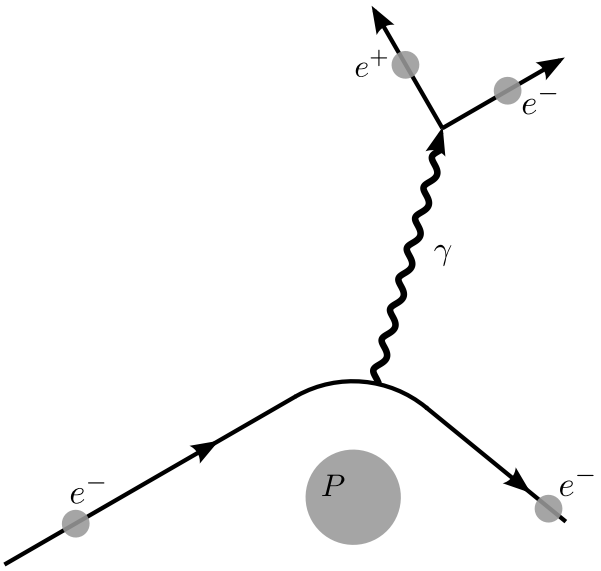

Figure 2.25: A schematically diagram of the production of TEBs, where relativistic runaway electrons interacts with a particle P, generates Bremsstrahlung (TGFs) that in the end produces an electron-positron pair due to pair production (TEBs). TEBs can also we produced by Compton scatting.

Collisions are dependent on the atmospheric density, which decreases with increasing altitude. There is a competition between collisions and gyration of the electrons in a TEB propagating upward in the atmosphere. When the electron gyro frequency ω_g, is equal or greater than the electron collision frequency ν_c, the gyro motion starts to dominate (see Section 2.3.1 and 2.2.2). Then the electrons and the positrons gyrate along the geomagnetic field lines into space. Modeling done by *Lehtinen and Inan* [2005] is presented in Figure 2.26. The altitude, where the collision frequency is equal to the gyro frequency, is plotted as a function of electron energy both for elastic and inelastic collisions. For electrons in excess of 1 MeV, this ratio (ω_g/ν_c) for inelastic collisions is equal to one in an altitude between 20 km to 30 km. Above this altitude, the gyration is thought to dominate more and more. This is important to take into account when deciding the altitude of the magnetic foot points (see Section 4.4).

The second bright peak in Figure 2.24 is, according to *Dwyer et al.* [2008], correlated to a mirrored peak of the TEB. When the electrons arrive the conjugate part of the field line, the magnetic gradient increases. This leads to magnetic mirroring for

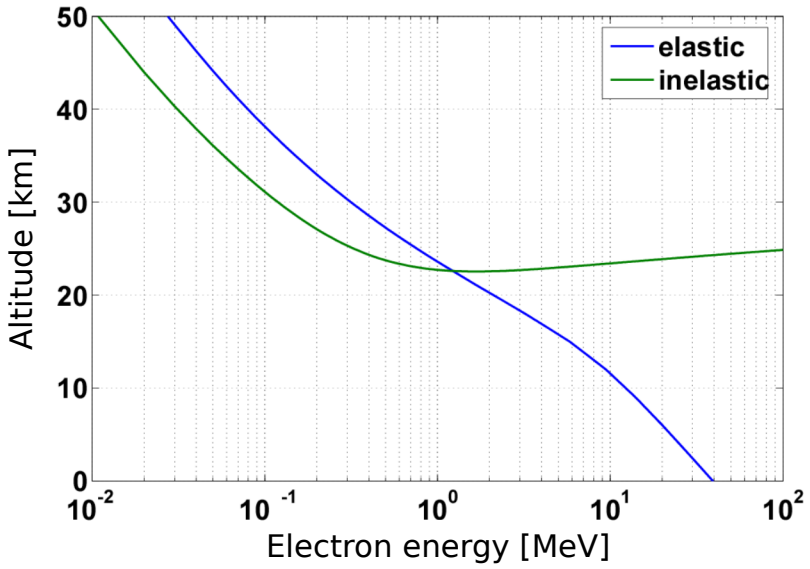

Figure 2.26: The plot presents in what altitude the gyro frequency ω_g is equal the collision frequency ν_c for an electron with a given energy. Figure from *Lehtinen and Inan* [2005].

those electrons that are not absorbed in the atmosphere (see Section 2.2.5). Those mirrored electrons gyrate back to the satellite, as seen about 25 ms after the first bright peak in Figure 2.24.

The blue curve in Figure 2.24 is the result of modeling. In the model, the travel distance between the conjugate mirror points and absorption in the conjugate hemisphere are taken into account [*Briggs et al.*, 2011]. The blue curve fits well both the first and second peak in the plot.

2.5.4.3 TEB simulations

Carlson et al. [2011] have performed Monte Carlo simulation of TEBs. The source of the TGF was located at 20 km altitude in an upward direction with solid angle distributed as $\mathrm{d}N/\mathrm{d}\Omega \propto \exp(-\theta^2/2{\sigma_\theta}^2)$, where θ is the zenith angle and σ_θ is a measure of the width of the beam. The initial photon energy distribution is based on earlier simulations of relativistic runaway avalanches and is consistent with TGF observations. Models to trace geomagnetic field lines (IGRF11) and particle interactions (GEANT4 Monte Carlo) are used in the simulation. A simulated satellite, where the beam is detected, is located in an orbit of 500 km altitude and an inclination of 26° (same as for the RHESSI satellite). The goal with the simulation was to find the detection frequency of TGFs and TEBs and two results were particularly relevant:

1. The number of electrons and photons per area (fluence) of the emission at satellite altitude.

2. The area of the TGFs and TEBs at satellite altitude.

Figure 2.27 shows examples of electron and photon fluence distributions at satellite altitude. For the electron beam the area is in the plane perpendicular to the field line. These simulations is based on photons with $\sigma_\theta = 40°$. In Figure 2.27a two electron beams are presented at different L-shells. The contours in the plot represent horizontal rings of radius 15 km, 25 km and 35 km at 57 km altitude upward along the geomagnetic field line. As seen in the figure, TEBs at different latitudes are not of the same geometric shape. This is also dependent on how narrow or broad the initial photon beam is, related to σ_θ.

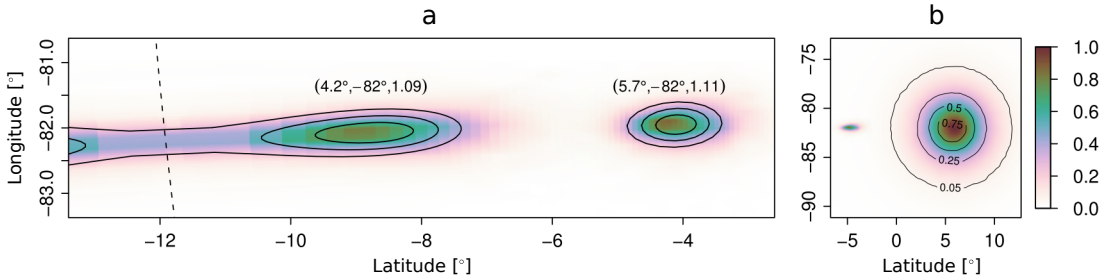

Figure 2.27: Electron and photon fluence at satellite orbit simulated with $\sigma_\theta = 40°$. (a) Electron beam and the electron generating photon source (labeled: latitude, longitude, L-shell). The contours represent horizontal rings of radius 15 km, 25 km and 35 km, at an altitude of 57 km. The dashed line is the geomagnetic equator. (b) Photon (to the right) and electron (to the left) fluence at satellite orbit. The photon source were located at latitude 5.7° and longitude −82°. The contours represent the photon fluence relative to the peak fluence. Figure from *Carlson et al.* [2011].

The effective geometry of TGFs and TEBs correlated to the simulations done by *Carlson et al.* [2011] can be seen in Figure 2.28. The factor a in this plot is the ratio a = P(TGF)/P(TEB). In other words, a is the ratio of how many TGFs that should be detected per TEB detection. The grey area indicates the effective TEB size vs the effective TGF radius in satellite altitude, assumed that the minimum detectable fluence for electrons and for photons are equal. The dashed lines connects identical peak fluences through different σ_θ. If you follow the dashed line labeled 5x, the TEB fluence is five times greater than the minimum detectable fluence at the instrument. As an example, if one consider a TGF with initial $\sigma_\theta = 40°$ such that the TEB peak is 20x larger than the detection threshold. Then Figure 2.28 tells that the effective size of the TEB will be about 55 km and the corresponding TGF will be about 600 km in radius at satellite orbit. This considered event is near the a=100 contour. By this, the satellite should detect 100 TGFs per 1 TEB.

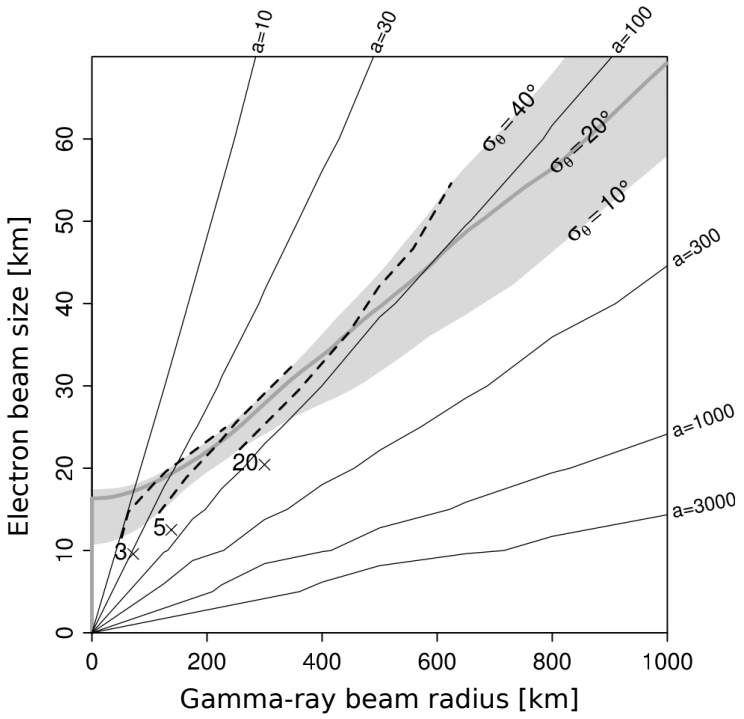

Figure 2.28: The effective geometry of TGF and TEB. The thick grey area denotes the effecitve electron beam size vs the effective photon beam radius at satellite orbit. a is the ratio P(TGF)/P(TEB). Figure from *Carlson et al.* [2011].

Since the number of detected TEBs is still too low to find statistical ratios in data bases, it is difficult to compare simulations, as described above, with observations. However, if we compare with observations from FERMI, which according to *Briggs et al.* [2011] observed 77 TGFs and 6 TEBs between July 11, 2008 and July 1, 2010. This correlates to $a \approx 13$, and it is much the same for BATSE [*Carlson et al.*, 2011]. $a = 13$ is a large number of TEBs compared to TGFs. *Carlson et al.* [2011] points out that the $a = 10$ contour in Figure 2.28 intersects the grey areas just for small sized TEBs and TGFs. The detection probability for TEBs with size < 20 km is $\sim 6 \times 10^{-6}$ [*Carlson et al.*, 2011]. The 6 FERMI TEBs detected in 2 years should correspond to at least 10^6 TGFs.

Xiong et al. [2012] have done simulations of where TEBs may be observed by satellites. The study is built on comparison lightning rate data from the Lightning Image Sensor (LIS) and the Optical Transient Detector (OTD). It is assumed that the TGF occurrence rate is proportional to the lightning rate. TEB observations depend on the satellite orbit, inclination, instrument detection thresholds and other instrumental effects. By this, the number of detected TEBs will be different from satellite to satellite, but *Xiong et al.* [2012] concludes that the best detection altitude for TEBs are below 1000 km. Figure 2.29 presents the full-year average result of the

study of where to detect TEBs. In other words, where the geomagnetic field line that the satellite passes through has foot points in regions with high lightning rates. The most actual regions are when magnetic foot points are located in South America, Africa or East Asia (as can be seen in Figure 2.29).

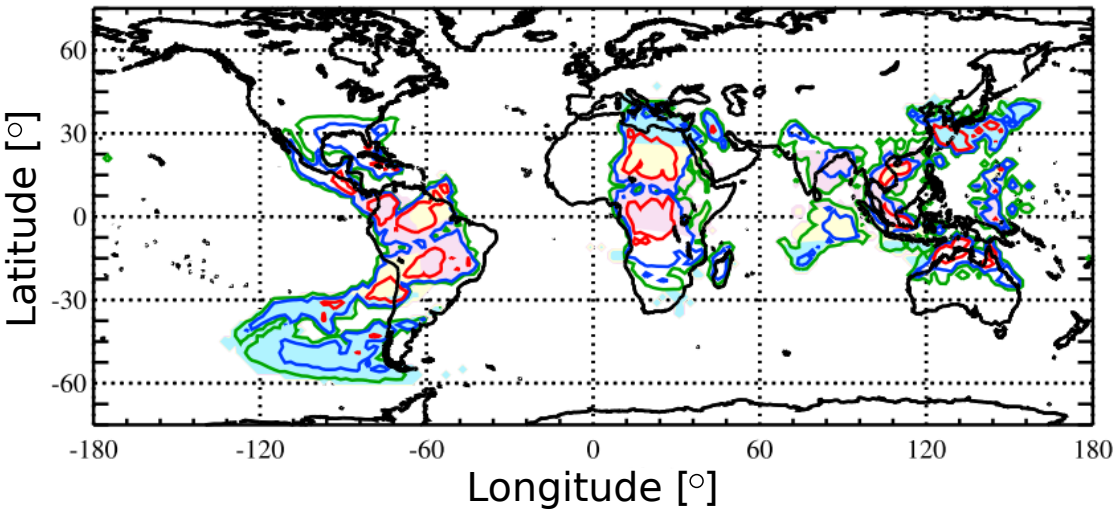

Figure 2.29: Full-year averaged location map for TEBs detected, by a satellite in 350 km altitude. The solid line contours correspond to relative TEB rates $1-5$ (green), $5-20$ (blue) and ≥ 20 (red). The colored regions indicate the length of the magnetic field line to that point: 500 km to 2 000 km (light red) 2 000 km to 5 000 km (light yellow) and $\geq 5\,000$ km (light blue). Figure from *Xiong et al.* [2012].

Chapter 3

Instrumentation and data description

In this chapter we will focus on instruments and the data used in this thesis. It starts with The Solar Anomalous and Magnetospheric Particle Explorer (SAMPEX) project and the Heavy Ion Large Telescope (HILT) instrument. Brief descriptions of the World Wide Lightning Location Network (WWLLN) and the International Geomagnetic Reference Field (IGRF) are given, and in the end the different types of data sets are described.

3.1 SAMPEX - The Solar Anomalous and Magnetospheric Particle Explorer

In 1988 NASA's Small Explorers (SMEX) program was first announced. The program should focus on low cost science projects, rapid development and launch with Small Expendable Launch Vehicles. Development, launch service, mission operations and data analysis should not charge NASA for more than $ 120 million per project [*NASA Goodard*, 2015].

The Solar Anomalous and Magnetospheric Particle Explorer (SAMPEX) was the first SMEX project. It was a relatively small spacecraft with mass of 350 lb ($\sim$ 160 kg), launched from NASA's Western Test Range (Lompoc, Ca) at 14:19 UTC on July 3rd 1992. It was launched into a polar low Earth orbit with inclination of 82° and altitude of 520 km by 670 km [*Baker et al.*, 1993]. In this thesis we use data from 2012, which was the last year of SAMPEX operation. The altitude in year 2012 was, according to altitude/position data, closer to 300 km. In Figure 3.1 the altitude on October 15, 2012 is plotted. It varies from $\sim$ 280 km to $\sim$ 310 km.

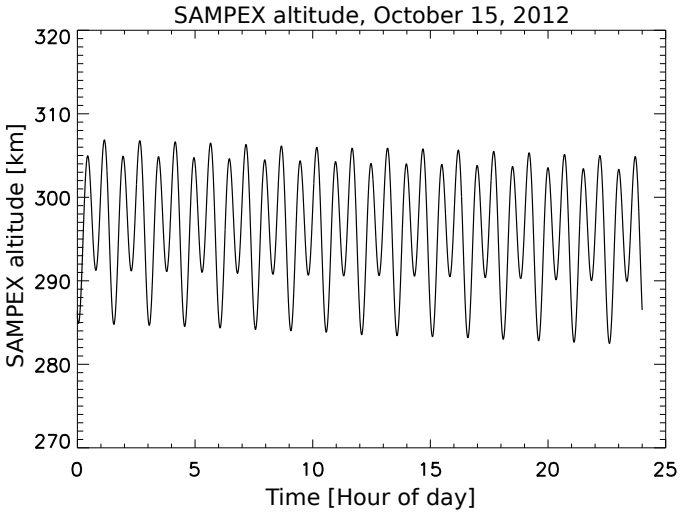

Figure 3.1: SAMPEX altitude on October 15, 2012. Data from SAMPEX Attitude/Orbit (PS Set) Data (see Section 3.4.2). The altitude varies from ~ 280 km to ~ 310 km.

SAMPEX had four different instruments: Low energy Ion Composition Analyzer (LICA), Heavy Ion Large Telescope (HILT), Mass Spectrometer Telescope (MAST) and Proton/Electron Telescope (PET). These four instruments had their mutual goal to study particles originating at the sun, map the magnetosphere and do in situ measurements of the radiation belts surrounding the Earth. Figure 3.2 presents the SAMPEX satellite schematically with all instruments and solar panels. Table 3.1 gives the primary measurements of each instrument.

The power subsystem was based on the two solar panels (see Figure 3.2) that generated electricity when the satellite operated in sunlight. Energy was stored in a nickel cadmium battery that was the power source during dark periods.

The Attitude Control Subsystem (ACS) was created as a solar-pointed/momentum-bias system and was consisted of one momentum wheel and three electromagnetic torque rods. The first part of the mission, through May 1994, SAMPEX was orientated such that it was pointed towards the sun and rotating about the sun line once per orbit. In this mode the instruments line-of-sight was pointed to zenith when passing over the poles. During 1994 and 1996 SAMPEX's attitude was modified such that it was pointed in the general direction perpendicular to the Earth's magnetic field, when the field strength was < 0.3 Gauss, typical in the equatorial region. A new orientation mode was introduced in May 8 1996, that is the actual mode for 2012 data, where the spacecraft continually spun 1 RPM around the sun pointing axis [*Mason et al.*, 1998].

On November 13, 2012 SAMPEX re-entered the atmosphere. The science mission ended on June 30, 2004, but the HILT instrument was operating to the very end of

2012. HILT is the instrument we have used in this TEB search and will be described more in detail in Section 3.1.1.

Table 3.1: SAMPEX instruments and their Primary Measurements. Adapted from *Mason et al.* [1998]

Instrument	Primary Measurements
HILT	Anomalous cosmic ray charge state: electrons > 150 KeV
LICA	Low energy ions: kilovolt electrons
MAST	Solar, galactic and anomalous cosmic ray isotopes
PET	Electrons > 400 keV: H, He isotopes

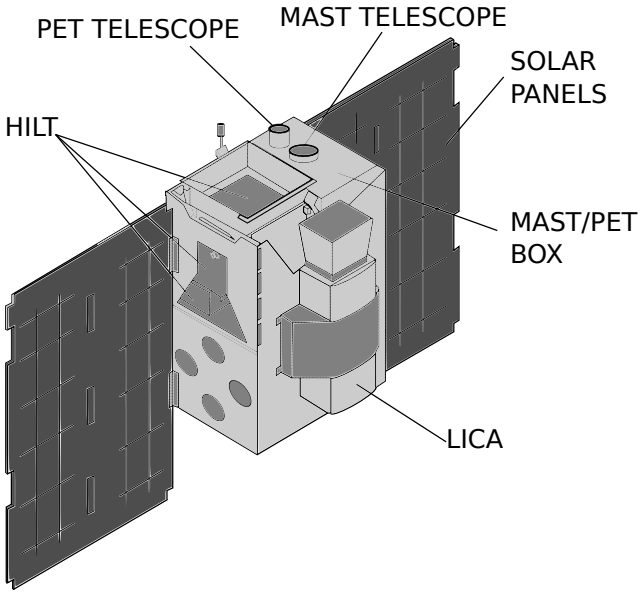

Figure 3.2: Schematic SAMPEX overview. All four instruments: HILT, PET, MAST and LICA are represented together with solar panels. Adapted from *Baker et al.* [1993]

3.1.1 HILT - Heavy Ion Large Telescope

One of four instruments at SAMPEX was the Heavy Ion Large Telescope (HILT). Data from this instrument is used in our TEB search. As the name tells, HILT is designed to measure heavier ions from helium to iron in the energy range of 4 MeV/nucleon to 250 MeV/nucleon. It has a relatively large geometric factor of 60 cm^2sr and is optimized to do compositional and spectral measurements of low intensity cosmic rays.

The instrument is built up of different components, as can be seen in Figure 3.3. It measures mass, kinetic energy and direction of particles that hit the detector. HILT consists of a three element ion drift chamber that is covered by two 20 μm thin aluminum plates and a micro meteoroid shield of 20 μm. The three elements in the ion drift chamber are the position-sensitive proportional counter in front (PCF), the ionization-chamber anode and the rear proportional counter (PCR) [*Mason et al.*, 1998]. The drift chamber was in its operational period filled with isobutane and the drift electric field (85 V/cm) was generated between parallel wires [*Klecker et al.*, 1993].

7.2 kg liquid isobutane was stored in an aluminum-Kevlar tank in the center of the spacecraft. This amount of isobutane was sufficient for continuous operation, the first three years of the mission. The gas density was actively regulated by valves, both out-flow and in-flow [*Klecker et al.*, 1993].

In the back of the ion drift chamber there were placed 16 circular Li-drift silicon solid state detectors (SSD) and 16 circular CsI crystal detectors behind the SSD's. Each solid state detector was 2 mm thick with a detectable area of 995 mm^2. They were arranged in four arrays with four detectors each and will later be described as four SSD detectors.

Particles with high energies that penetrate the SSD arrays and a 0.1 mm aluminum plate, are then detected by the CsI crystal array connected to a photodiode.

All these HILT components together make the different measurements. The element/mass measurements (dE/dx) are a combination of detection by the position sensitive proportional counter and the ionization chamber with remaining energy information from the SSD and the CsI detectors. Particle directions are derived from a combination of PCF, PCR, electron drift time and the SSD [*Klecker et al.*, 1993].

In addition to the heavier ion measurements, HILT also detects electrons with energies in excess of 15 keV and 1 MeV (see Table 3.2) [*Mason et al.*, 1998].

In November 1995, more than three years after launch, the aluminum-Kevlar container had no more isobutane. This led to a change of mode in the operational period of HILT. The mode before the isobutane ran out is called the *normal mode*. In some months, the ion drift chamber was drained out of gas and in March 1996 HILT was switched to the *High Energy mode*. The difference between these two modes is presented in Table 3.2. In the 2012 data (High Energy mode), that is used in this thesis, HILT detected electrons in excess of 1 MeV with a geometric factor of 60 cm^2sr.

Table 3.2: HILT energy ranges for selected species. Adapted from *Mason et al.* [1998]

Element	-Energy Range (MeV or MeV/nuc.)- Normal mode (Isobutane on)	High Energy mode (Isobutane off)	Geometric factor (cm^2sr)
Electrons	> 0.15	-	10
Electrons	> 1.0	> 1.0	60
^{4}He	4.3 - 38	20 - 40	60
^{16}O	8.2 - 200	42 - 200	60

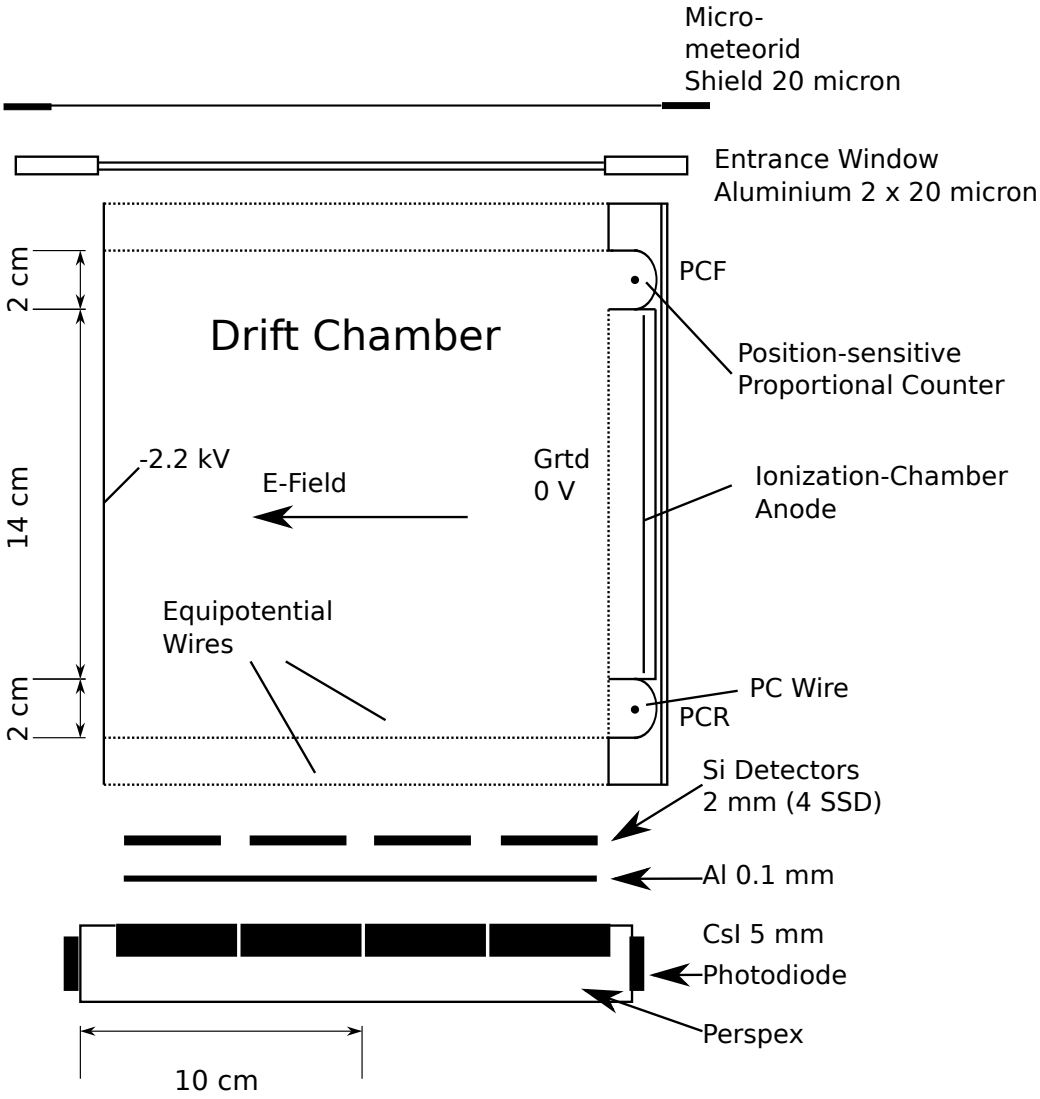

Figure 3.3: Schematic SAMPEX overview. Adapted from *Mason et al.* [1998]

3.2 WWLLN - World Wide Lightning Location Network

In our search for lightning activity corresponding to TEBs, we use data from the World Wide Lightning Location Network (WWLLN). WWLLN is a global network that consists of more than 60 detection sites located at university campuses and research stations all over the world [*Burkholder et al.*, 2013]. WWLLN detects both the position and time of lightning strokes.

The network identifies sferics in the middle part of the VLF band 6 kHz to 22 kHz, produced by lightning. These waves propagate in the Earth-Ionosphere Waveguide (EIWG) (see Section 2.4.7). These VLF-frequencies are ideal for long range lightning detection, because the attenuation factor is relatively small. The attenuation factor is about 1 db to 2 dB per 1 000 km of propagation, but depends on propagation direction and time of day (ionosphere altitude, see Section 2.4.7). This low factor makes it possible to detect global lightning activity with a manageable number of detectors. Use of both the propagation of "line-of-sight waves" and "sky-waves" (EIWG), has been shown to lead to significant location error problems [*Dowden et al.*, 2008]. We will describe methods that minimize these errors.

To determine the location and time of a lightning stroke, WWLLN uses a method called the Time-Of-Group-Arrival (TOGA) and detected sferics from at least four stations [*Dowden et al.*, 2002]. One of many challenges according to lightning detection is that the long range detection implies that the antennas receive signals from different lightning strokes during a very short time period. It is difficult to compare signals at different sites to the same actual lightning stroke. Consider a lightning-stroke X. This stroke has to be detected by at least four antennas. Each of these antennas receives about 100 VLF sferics every second from all directions and from distances up to 13 Mm. This means that if the nearest and the farthest antennas is respectively 1 000 km and 13 000 km away from the stroke, the TOGA differs in a typical range of $\sim$ 30 ms. During this period each antennas could have received other sferics from other strokes than X. To compensate for this, all the TOGAs labeled with the detection antenna, is sent to the central processing computer (CPC). Analyses done by the CPC using a WWLLN location algorithm sort out TOGAs with the actual lightning stroke.

To minimize the location-errors, WWLLN uses a method called the "down-hill simplex" method (DHSM). Consider a lightning stroke and at least four detectors that have registered the TOGA. X_0 is a zeroth approximation, where the location algorithm assumes that the lightning stroke occurred at the nearest detected antenna, the first TOGA-site. All the other TOGAs are calculated as if the stroke occurred at X_0. The X_0 TOGA is now the reference for all the other calculated times of group arrival that differs from those observed. The DHSM uses this set of

differs to move X_0 in a "down hill" direction to a better approximation, X_1. For a stroke in X_1, the respective group arrivals are calculated with a new set of differs. This algorithm has to be repeated for X_2, X_3, X_4 etc., until the differences are acceptable small.

WWLLN detects both cloud-to-ground (CG) and intra-cloud (IC) lightning (see Section 2.4.6), but does not differentiate between them. Because CG lightning generally have higher peak currents than IC, WWLLN is more sensitive to CG lightning [*Collier et al.*, 2011]. Comparison studies done by *Abarca et al.* [2010] showed that the WWLLN detection efficiency over the United States was 10.3% for CG lightning and 4.82% for IC lightning (2008 to 2009) and it was as high as 35% for the most powerful CG discharges [*Collier et al.*, 2011]. *Rodger et al.* [2005] did a study of the efficiency over Australia and found it to be $\sim$ 26% for CG and $\sim$ 10% for IC. As seen, the detection efficiency varies a lot from detection region to detection region. The detection efficiency has increased over years, by better algorithm and more network detectors.

3.3 IGRF - International Geomagnetic Reference Field

In Section 2.2.3 a simple geomagnetic dipole field was presented. In our search for TEBs we use a more complex numerical model that is called the International Geomagnetic Reference Field (IGRF). It is produced and maintained by modelers under the support of the International Association of Geomagnetism and Agronomy (IAGA) [*Finlay et al.*, 2010]. IGRF is based on observations done by many magnetic observatories and satellites.

This is a spherical harmonic model given by Equation 3.1, where the geomagnetic field vector is given by $\mathbf{B} = -\nabla V$. V is the magnetic scalar potential, given by:

$$V(r,\theta,\phi,t) = a\sum_{n=1}^{N}\sum_{m=0}^{n}\left(\frac{a}{r}\right)^{n+1}\left[g_n^m(t)\,cos\,(m\phi)+h_n^m(t)\,sin\,(m\phi)\right]\cdot P_n^m(cos\,\theta), \quad (3.1)$$

where r is the radius from the Earth center, $a = 6371.2$ km is the magnetic reference spherical radius (near the mean Earth radius), θ is the geocentric co-latitude[1] and ϕ is the east longitude. g_n^m and h_n^m are numerical Gauss coefficients and $P_n^m(cos\,\theta)$ is the Schmidt semi normalized associated Legendre function of degree n and order m [*Finlay et al.*, 2010]. The coefficients are determined by the large number of measurements and usually $n \sim 6$, meaning 6 coefficients.

[1] Co-latitude is 90° - latitude

3.4 Data description

We use data from The SAMPEX Data Center and WWLLN (`http://wwlln.net/new`) in our search for TEB events. There are different types of data sets to download at The SAMPEX Data Center (`http://www.srl.caltech.edu/sampex/DataCenter/`). We use the *High time-resolution Rate Data* from HILT and *Attitude/Orbit data*. In this section the different sorts of data will be described.

3.4.1 High time-resolution Rate Data from HILT

The *High time-resolution Rate Data* from HILT is organized in 4 states. State 1 is data with launch configurations, from 1992 to 1996. These data sets give counts per 100 ms. State 2 is the first 20 ms SSD configuration from parts of 1994. In this state HILT counted counts per 20 ms for SSD1, SSD2, SSD3 but counts per 100 ms for SSD4. State 3 is a 30 ms SSD/PCRE configuration from the end of 1994 through 1995. All these states, 1 to 3, have a geometric factor of 15 cm^2sr per SSD detector. The one we are interested in is the state 4 data. From 7th of August 1996 to 3rd of November 2012, the High time-resolution Rate Data gives the sum of particle flux detected from all four SSD detectors in counts per 20 ms. This means that we have an effective geometric factor of 60 cm^2sr and a time resolution of 20 ms. We had to reorganize our data set before we could start our search. State 4 data is built up of rate 1 to rate 6 [*Davis*, 2012]:

- Rate 1: Sum from Time to Time + 20 ms
- Rate 2: Sum from Time to Time + 20 ms to Time + 40 ms
- Rate 3: Sum from Time to Time + 40 ms to Time + 60 ms
- Rate 4: Sum from Time to Time + 60 ms to Time + 80 ms
- Rate 5: SSD4 from Time to Time + 100 ms
- Rate 6: Sum from Time + 80 ms to Time + 100 ms

Rate 5 data are counts per 100 ms from SSD4 only. This is not interesting for this TEB search algorithm, where we want the optical time resolution of 20 ms (typical TEB duration can be seen in Table 2.2). Therefore rate 5 is not used. To make an array of time and counts one has to pick out the first element in rate 1, the first element in rate 2, rate 3, rate 4, rate 6, etc. This will be the first 0.1 s of the reorganized data set, with a respectively time array like: [0.00, 0.02, 0.04, 0.06, 0.08 ...]. The state 4 data set does not start at 0 seconds after midnight in all days and it jumps over seconds in the middle of the day. It is therefore important to include the time data from the data set. The time and counts are all the information you get from The high time-resolution Rate Data.

The spacecraft clocks drift about a second during each day, but start synced every midnight. This lead to time uncertainty in The High time-resolution Rate Data of as much as one second. SAMPEX was mainly designed around measurements varying more with location than with time, not for millisecond duration events [Mark Looper, personal communication, November 26, 2014]. The absolute time uncertainty is $\leq 1\,\mathrm{s}$.

3.4.2 SAMPEX Attitude/Orbit (PS Set) Data

SAMPEX Attitude/Orbit (PS Set) Data have a time resolution of 6 seconds and contains a lot of information. In our TEB search, we use time and position information from this data set, e.g. year, day of year, hour, second of day, SAMPEX georadius, geolongitude and geolatitude.

It has been done a linear interpolation between the 6 second data points, but since these data runs on the same spacecraft clock as The High time-resolution Rate Data, the drift in the clock also affects the accuracy in the position data to be $\leq 1\,\mathrm{s}$.

3.4.3 WWLLN data

The World Wide Lightning Location Network (WWLLN) data set is sorted per day and presents time of the lightning stroke (date and time), the predicted lightning location in longitude/latitude, a measure of the strength of the lightning stroke and the number of stations that detected the sferics. Time and location are the only parameters used in this thesis.

The position accuracy of a WWLLN detection varies with the number of antennas involved. According to *Rodger et al.* [2005] and *Jacobson et al.* [2006], accuracies of WWLLN location and time at source are respectively $\leq 10\,\mathrm{km}$ and $\sim 30\,\mu s$. Notice that the time uncertainty for WWLLN is much smaller than for the SAMPEX data.

Chapter 4

Methodology

There are four main components in the search for TEBs: 1) the HILT data and the position data at SAMPEX, 2) a geomagnetic field line traced by IGRF, 3) a lightning stroke detected by WWLLN and 4) a beam of gyrating electrons/positrons (propagation time). In Figure 4.1 the geometry of the main components that are included in the TEB search is presented.

In this chapter the method will be presented. At first we describe the search for significant counts in the HILT data, called the TEB search algorithm. Then geographical search limits, tracing of geomagnetic field lines and the search for lightning are described. In the end a null hypothesis is presented.

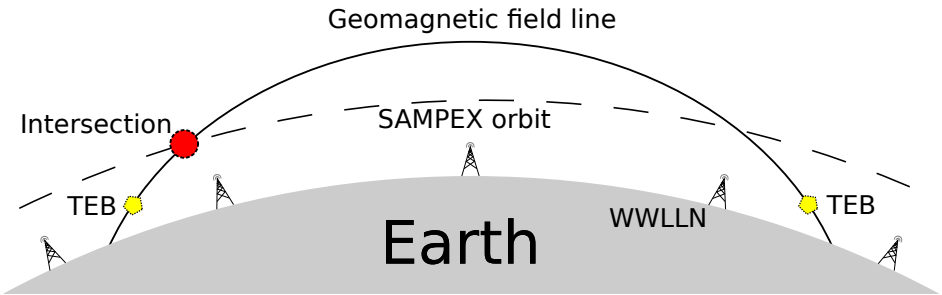

Figure 4.1: The Earth (in grey) with WWLLN antennas, the SAMPEX orbit (dashed curve) and a geomagnetic field line are presented (solid curve). The points of interests are where the SAMPEX orbit intersects the actual geomagnetic field line around which the electrons in the TEB gyrate (red disk) and the potential TEB sources at the two foot points of the field line (yellow pentagon).

4.1 Search for significant counts

4.1.1 Search A - Poisson statistics

The TEB search algorithm searches for counts in the HILT data, that is significant above the background radiation. One day of counts consists of $\sim 4.3 \cdot 10^6$ bins of 20 ms. The search algorithm searches bin by bin, with a m bin wide Region of Interest (ROI), where n observed is the sum of counts in the ROI. Typical values of m could be 1, 2 or 3 bins, that corresponds to 20 ms, 40 ms and 60 ms. If you assume the background radiation is Poisson distributed, you can use the Poisson distribution function to find the probability $P(N \geq n|b_{obs})$. Conditions that have to be satisfied are given in Appendix A. This is the probability to find N counts in a ROI, that is greater than or equal to the sum of counts n in the actual ROI, given an observed background count rate b_{obs}. The lower this probability value is, the more significant is our candidate. To get an approximation of the true background count rate in the time period before and after one given ROI, the mean value of k bins before and k bins after the ROI has to be estimated. A typical value of k could be 40, that corresponds to 800 ms. The observed background count rate b_{obs} is given by:

$$b_{obs} = \frac{1}{2 \cdot k}\Big(\sum_{h=i-(k+l)}^{i-l-1} n_h + \sum_{j=i+l+m}^{i+k+l+m-1} n_j \Big), \tag{4.1}$$

where l is the number of bins between the ROI and the background bins, to prevent signals from the peak to affect the background count rate level. m is the number of bins in the ROI and n_i is counts in the first bin in the ROI. The indices are illustrated in Figure 4.2.

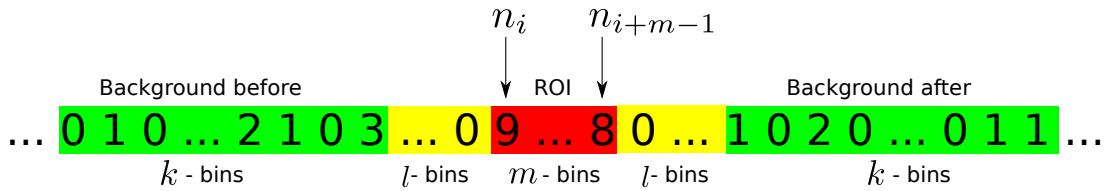

Figure 4.2: An example of an array of counts. The m bin wide Region of Interest (ROI) consists of the bins those are evaluated. The observed background count rate b_{obs} is estimated by taking the average of k bins before and k bins after the ROI, with l bins between. n_i is the first bin in the ROI and n_{i+m-1} is the last bin in the ROI. The search algorithm is searches bin by bin.

The first search (search A) for TEB candidates is done by The Poisson Cumulative Distribution Function (CDF). The probability of observing the sum of counts N in a ROI to be equal or greater than the sum of counts n in the actual ROI, given an

observed background count rate b_{obs}, is given by (see Appendix A about the Poisson distribution):

$$P_A(N \geq n|b_{obs}) = 1 - \sum_{i=0}^{n-1} \frac{\mu^i e^{-\mu}}{i!}, \tag{4.2}$$

where the expected value $E(N) = \mu = b_{obs}$. This probability value is called the p-value. If the estimated p-value for a ROI is less than a given p-value limit, the bin has to be flagged as interesting. In a year we have $\sim 10^9$ bins of data. By this, we will get one false positive TEB candidate per year if we choose p-value less than 10^{-9}, and one false positive per 10 years for p-value less than 10^{-10}. We accept one false positive per year, P$< 10^{-9}$.

In our TEB search a lot of different values of k, l and m are tried out. Some of the chosen values are presented in Table 4.1. In method 1.1-1.3, the search tests both for a one ($m = 1$) and two bins ($m = 2$) wide ROI. If a candidate is significant both in one and in two bins, the one with the lowest p-value is chosen. This is also the case if two ROI's are overlapped. Then the ROI that is most significant is chosen. Method 2.1 and 2.2, where the search is based on a three bin wide ROI ($m = 3$), is the same as *Carlson et al.* [2009] used in their search for TEBs. Method 3.1 is a collection of all the different TEB candidates found by method 1.1-2.2.

Table 4.1: Table of method description. k, l and m are described in Figure 4.2.

Method	k	l	m
1.1	40	3	1 or 2
1.2	250	50	1 or 2
1.3	250	3	1 or 2
2.1	40	0	3
2.2	40	9	3
3.1	Collection of all different methods (1.1-2.2)		

According to the typical TEB duration of ≤ 30 ms (see Table 2.2), a TEB is expected to be spread over a maximum of three 20 ms bins. Figure 4.3 is a visualization of why we use one, two and three bins wide ROI ($m = 1, 2, 3$) in our search. Consider a one bin signal, see Figure 4.3a. This could be significant above background in a one bin wide ROI (method 1.1-1.3) and maybe in a two bin wide ROI. If the signal is not very bright, the signal could be missed by using three bins. Events like this would then be marked as interesting by method 1.1-1.3, but not by method 2.1-2.2. A signal spread over two bins, see Figure 4.3b, could be significant with a two bins wide ROI, but insignificant by using one or three bins. Then it would be sorted out by method 1.1-1.3, but not by method 2.1-2.2. Equivalent, Figure 4.3c presents a signal that is thought to be significant for a three bins wide ROI (method 2.1-2.2), but it has to be brighter in at least one bin to be detected by method 1.1-1.3. It is

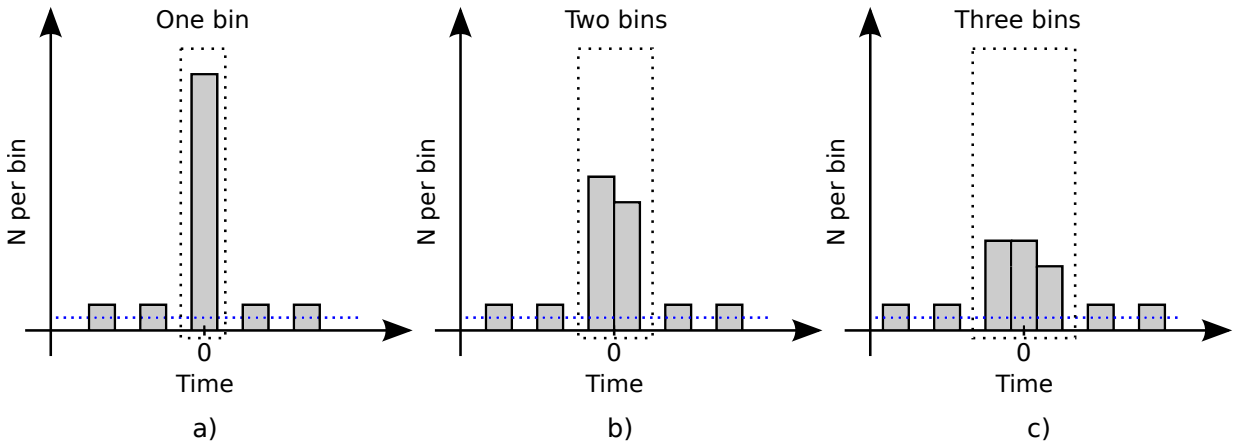

Figure 4.3: Examples of different signals spread over one, two and three bins. All these signals are thought to be potential TEBs. Method 1.1-1.3 are thought to find signal a) and b) more significant than signal c). Method 2.1-2.2 are thought to find signal c) more significant than signal a) and b).

expected that the number of signals sorted out, will decrease with increasing number of bins in the ROI.

4.1.2 Search B - Fluctuations in the background

All candidates found by search A, have to be checked by search B. The estimated background, k bins before and after the ROI, is subject to statistical fluctuations. Such fluctuations, may have a major effect on the probability calculation of events to occur. It has been tried to compensate for these fluctuations, by taking an average of the unknown true background count rate b. The probability of finding counts in the ROI N, greater or equal than the counts observed n, given an observed background b_{obs}, is now given by:

$$P_B(N \geq n|b_{obs}) = \int_0^\infty P(N \geq n|b)P(b_{obs}|b)\,\mathrm{d}b. \tag{4.3}$$

$P_B(N \geq n|b_{obs})$ has to be less than a given p-value limit, in this search set to 10^{-9}. This method allows the unknown true background count rate to be higher than the observed background count rate, by allowing for statistical fluctuations. According to *Carlson et al.* [2009] this is especially relevant in cases where there are just a few counts in the ROI and the background count rate is low or zero.

4.1.3 Search C - Number of bins

In search C, all the events that have been marked as interesting in search A and B are checked again. This is a correction for the number of time bins N_{bins}, for both P_A and P_B. *Briggs et al.* [2013] did this in the search for TGFs and TEBs, and pointed out that this is precisely not the probability that a candidate is a chance fluctuation, but rather a useful rank of the candidates. The corrected p-values in search C, are given by:

$$P_{C_A} = 1 - (1 - P_A)^{N_{bins}}, \tag{4.4}$$

$$P_{C_B} = 1 - (1 - P_B)^{N_{bins}}, \tag{4.5}$$

where N_{bins} is the number of bins in the ROI (m) for the actual candidate. Both P_{C_A} and P_{C_B} have to be less than 10^{-9}.

4.2 Polar regions and the South Atlantic Anomaly

Due to high particle flux in the polar regions and the South Atlantic Anomaly, it is important to consider where SAMPEX is located during an actual significant TEB candidate. According to *Carlson et al.* [2009], one detected pulse of electrons associated to TEBs will maximum be in order of 50 counts, which means that the TEB will be drowned in the data due to high background radiation. A way to avoid this problem is to make some geographical cut-off limits for the search. One case is to exclude all candidates where SAMPEX is at higher latitudes than 45°, to avoid the polar region at the northern hemisphere. At the southern hemisphere it is important to exclude both the polar region and the South Atlantic Anomaly. The geographical search limits used in this search for TEBs, are presented in Figure 4.4. These are much the same as the search region *Carlson et al.* [2009] used. The region inside the limits is called the TEB search region. An example of a removed event detected by HILT outside the TEB search region, is presented and discussed in Section 5.1.4 (Figure 5.4a).

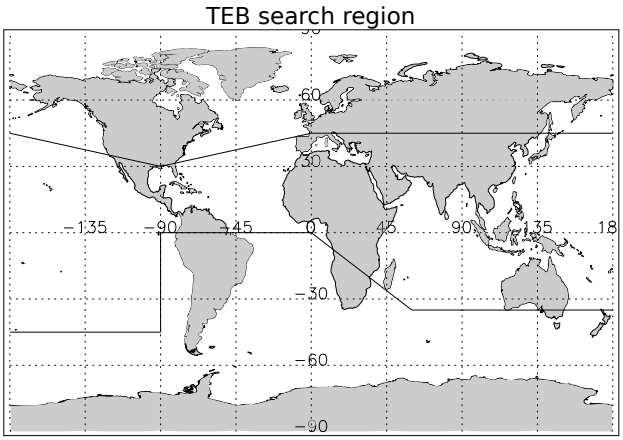

Figure 4.4: Geographical limits are marked as solid lines. The TEB search is restricted to moments where the satellite is in this region. These limits are used in the TEB search to avoid high particle fluxes when the satellite passed over the polar regions and the South Atlantic Anomaly.

4.3 Strong gradients in the observed background

The TEB search algorithm searches for brief $\sim 20\,\mathrm{ms}$ pulses of electrons (see Table 2.2), not long duration events. If SAMPEX entered a region where the count rate per bin increases a lot from one bin to another, and this is something in the duration range of seconds, then the background count rate varies a lot from the region of bins where the count rate is low, to the bins where the count rate is high. An illustration of this can be seen in Figure 4.5. The first and the last bins in such an event, where there are strong gradients in the background, may affect the TEB search significantly. A method that is used to identify such events, is to compare the background count rate estimated from the bins before and after the triggered ROI.

If σ is the square root of the total background count rate b_{obs}, that is the average of both the bins before and after the triggered ROI (Equation 4.1), a criterion (Equation 4.6) has to be fulfilled. The background count rate before b_{obs1} and the background count rate after b_{obs2} the ROI, has to be less than 3σ:

$$b_{\mathrm{obs1}} < 3\sigma = 3\sqrt{b_{\mathrm{obs}}} \text{ and } b_{\mathrm{obs2}} < 3\sigma = 3\sqrt{b_{\mathrm{obs}}}. \tag{4.6}$$

This criterion is shown to be a feasible way to sort out candidates that are obviously something else than TEBs, typical coming out of regions near by the South Atlantic Anomaly and the radiation belts. Example of such an event is presented in Figure 5.4b.

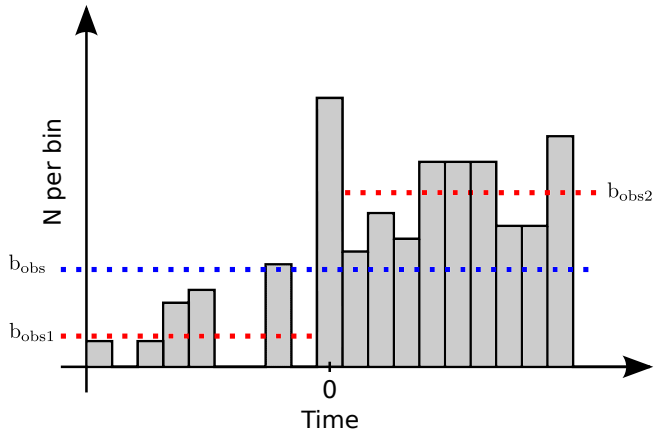

Figure 4.5: Illustration of strong gradient in the background count rate. b_{obs} is the observed background count rate (blue dotted line). b_{obs1} and b_{obs2} are respectively the estimated background count rate before and after the triggered bin(s) (red dotted lines).

4.4 Tracing geomagnetic field lines

In Section 3.3 the International Geomagnetic Reference Field was introduced. This model is used to map the geomagnetic field from the SAMPEX position, down to the Earth. In this mapping process we use the IDL Geopack DLM (`http://ampere.jhuapl.edu/code/idl_geopack.html`) that is a Dynamic Link Module (DLM) written by Research Systems, Inc. This package gives access to the GEOPACK Fortran library by N. A. Tsyganenko [*Korth*, 2008]. IDL Geopack DLM also gives access to other geospace related functions, such as coordinate converters used in this project.

The GEOPACK-TRACE function gives the geomagnetic field line vector and the foot points in both the northern and the southern hemispheres. These foot points are where the magnetic field line intersects the Earth's surface. In our search for TEBs, the interesting foot points are in an altitude of $\sim$ 45 km. Above this altitude the competition between gyration and collision is thought to be dominated by gyration. This is discussed more detailed in Section 2.5.4.2 and illustrated in Figure 2.26. *Cohen et al.* [2010] used a foot point altitude of 35 km, which is in the same range. To calculate the speed-of-light propagation delay for each electron beam, the propagation length is estimated as the distance from the foot point to the satellite position, along the magnetic field line.

4.5 Comparing candidates with WWLLN

A significant signal measured at SAMPEX is not necessarily a TEB event. Something that will give more confidence that the signal is really a TEB, is if there is lightning activity in the area around the magnetic foot points. In this search we use WWLLN (see Section 3.2).

We have three different categories in our search for lightning:

1. WWLLN match
2. Associated lightning activity
3. No associated lightning activity

These three categories are described below. To compare the time of a WWLLN sferic t_{WWLLN} with a measured signal at SAMPEX, we use this time interval criterion:

$$t_1 - \Delta t \leq t_{\mathrm{WWLLN}} + \frac{s}{c} \leq t_2 + \Delta t, \tag{4.7}$$

where s is the distance between the foot point and the satellite along the geomagnetic field line and c is the speed of light. Δt is at least the uncertainty value of the SAMPEX time tag. t_1 and t_2 are respectively the start and the end time of the actual ROI in the HILT data. The $t_{\mathrm{WWLLN}} + s/c$ is the estimated time of arrival of the first electrons hitting the detector. It is supposed that the fastest electrons propagate near by the speed of light, due to high kinetic energy and a small pitch angle [*Cohen et al.*, 2010].

4.5.1 WWLLN match

A WWLLN match is a TEB candidate that has at least one WWLLN detection within a radius of 250 km that meets the time criteria given by Equation 4.7. For a WWLLN match the Δt is set equal to the accuracy of the SAMPEX time tag ± 1 s ($\Delta t = 1$ s). This means the estimated time of arrival of the electrons has to be within the accuracy time interval of the measured signal at SAMPEX. This is the most stringent criteria of all these three categories.

4.5.2 Associated lightning activity

As mentioned in Section 3.2, WWLLN detects just a fraction of all lightning strokes that occur. It is a relatively high probability that WWLLN does not detect the actual lightning stroke that generates a TEB, but detects some lightning strokes in the same thunderstorm. Associated lightning activity is in this thesis defined as

lightning strokes detected by WWLLN within a radius of 250 km and a time interval of ± 1 min ($\Delta t = 60$ s). A radius of 250 km is larger than a typical thunderstorm (see Section 2.4.1), but this includes systems of thunderstorms.

4.5.3 No associated lightning activity

The third classification of the lightning search, is defined as TEB candidates that have no WWLLN detected sferics within a radius of 250 km, in a time interval of ± 1 min ($\Delta t = 60$ s). It is reasonable to assume that no associated TEB candidates, probably have to be something else than TEBs. This is more discussed in Section 6.3.

4.6 Null hypothesis

In Section 4.5.2 the associated lightning activity category is presented. We do not know if this lightning activity is correlated to TEBs. It is interesting to see if there are more lightning activity in foot points connected to SAMPEX when a significant signal is measured, than when SAMPEX just measures background. The motivation for the null hypothesis is to find out if our associated lightning activity seems to be random or not. If our TEB candidates actually are TEBs, it should be reasonable to expect significant more lightning activity correlated to those foot points, than in arbitrary foot points.

One million arbitrary moments in 2012 were generated by a pseudo-random number generator in IDL. For all these moments, the satellite position, magnetic field line and foot points were found in the same way as for the TEB candidates. The SAMPEX positions at arbitrary moments have to be inside the geographical search region (see Section 4.2). All moments where the criteria are fulfilled, have been searched for associated lightning activity (see Section 4.5.2).

A challenge in making such a null hypothesis, is that arbitrary moments do not necessarily lead to arbitrary positions. Satellites with inclination of more than 0° are passing more of their orbit at higher latitudes than at lower latitudes (see Figure 6.4). In this case, where the SAMPEX inclination is 82° and the geographical search region limits are $\sim \pm 40°$, the flight time per latitude is assumed to be more or less uniform.

To check if there are more associated lightning activity correlated to TEB candidates, than for arbitrary null candidates, the associated lightning activity ratios have to be compared. This is performed by a hypothesis test for a binomial distribution, where the associated lightning ratio for the TEB candidates η_{TEB} and the associated

lightning ratio for the null candidates η_{NULL}, are expressed in two hypotheses:

$$\begin{aligned} \text{H}_0 &: \eta_{\text{TEB}} \leq \eta_{\text{NULL}}, \\ \text{H}_1 &: \eta_{\text{TEB}} > \eta_{\text{NULL}}. \end{aligned} \tag{4.8}$$

H_0 is the hypothesis where there are no more associative lightning activity correlated to the TEB candidates than the null candidates. H_1 is the opposite hypothesis, where there are more associated lightning activity correlated to the TEB candidates.

$\text{P}(\text{X} \geq \text{x})$ is, according to the binomial distribution, the probability of observing more or equal the number of TEB candidates with associated lightning activity x, where $\text{X} \sim \text{bin}(n, p)$. The probability is given by:

$$\begin{aligned} \text{P}(\text{X} \geq \text{x}) &= 1 - \text{P}(\text{X} < \text{x}) \\ &= 1 - \sum_{i=0}^{\text{x}-1} \binom{n}{i} p^i (1-p)^{n-i}, \end{aligned} \tag{4.9}$$

where n is the total number of TEB candidates and the probability of success p is based on the associated lightning activity ratio for the null candidates. np is the expected value of TEB candidates with associated lightning activity. For $\text{P} < 0.05$, we reject H_0 with 95% level of confidence. If this is the case, the probability that there are more associated lightning activity correlated to TEB candidate foot points, than to arbitrary null candidates, is 95%.

4.7 Weaknesses of the method

There are several weaknesses in such a statistical search method, as the TEB candidate search algorithm. We only check for signals that are significant above background, but this does not mean that the measured signals are correlated to TEBs and lightning. Such signals just tells that HILT measures something above background variations. It could be something interesting or just fluctuations in the background radiation (one false trigger per year with p-value $< 10^{-9}$).

Another weakness are the limitations in the SAMPEX data, compared to other satellites. Other satellites do have energy, charge, mass and pitch angle measurements. In the HILT High-Resolution Count Rates data, we are limited to information about count rates, time and position. Because of this, we do not have the opportunity to search for positron annihilation lines at 511 keV in energy spectra.

The time resolution of 20 ms in the HILT data, is in range of a typical TEB event [*Carlson et al.*, 2009]. Because of this, we do not have the opportunity to observe multi peaked count rate spectrum, such as *Dwyer et al.* [2008] and *Briggs et al.*

[2010]. The drift in the space clock at SAMPEX of about one second per day, makes the time accuracy larger than first expected. This makes it more difficult to proclaim simultaneity between HILT and WWLLN.

Chapter 5

Observations

The SAMPEX data for 2012 have been analyzed as described in Chapter 4. The instruments used to measure signals that have generated these data sets, are described in Chapter 3. In this chapter the observations will be presented. Observations are events that have been flagged as interesting by the TEB search algorithm. There are different types of observations. At first, the data sets of significant signals measured by HILT will be presented. Then the lightning data set, WWLLN detection in foot points, are described. Finally, results of the SAMPEX - WWLLN comparison are presented.

5.1 Significant SAMPEX candidates

The TEB search algorithm does see a lot of significant TEB candidates in the SAMPEX data for 2012. A lot of bright signals with peaks significant above the background count rate level are observed. The number of observed significant signals are presented in Table 5.1, with their probability values. As mentioned in Chapter 4, there are different ways to do the TEB search. The different methods, 1.1 to 3.1, and searches, A to C, are described in Section 4.1. The methods consist of different number of bins in the ROI (m), the background count rate estimate ($2 \cdot k$ bins) and the bins between the ROI and the background bins (l). Search A is where the pure cumulative Poisson distribution function is used. In search B fluctuations in background are tried to be compensated for. Search C is where we correct for the number of bins used in the ROI. For all methods, 1.1.-2.2, search A to C are done. Method 3.1 is a collection of all the TEB candidates found by method 1.1-2.2. In this section, the data observed by the TEB search algorithm are presented.

Table 5.1: Number of significant candidates found by method 1.1 to 3.1 and search A to C. Description of the methods and searches are given in Section 4.1 and Table 4.1. $k \cdot 2$ is the number of 20 ms bins included in the estimated background count rate, l is the number of bins between the ROI and the background bins and m is the number of bins in the triggered ROI. Common candidates are those that fulfill search A to C and are found by more than one method (1.1-1.3, 2.1-2.2 or 1.1-2.2).

Method	$P(N \geq n\|b)$	Search A	Search B	Search C	Common	Common
	$< 10^{-9}$	509	254	228	164	5
1.1	$< 10^{-10}$	149	72	72	67	4
$k = 40$	$< 10^{-11}$	45	18	18	18	2
$l = 3$	$< 10^{-12}$	13	3	3	3	0
$m = 1$ or 2	$< 10^{-13}$	3	2	2	2	0
	$< 10^{-14}$	1	1	1	1	0
	$< 10^{-9}$	356	317	273		
1.2	$< 10^{-10}$	100	88	88		
$k = 250$	$< 10^{-11}$	27	22	22		
$l = 50$	$< 10^{-12}$	4	3	3		
$m = 1$ or 2	$< 10^{-13}$	2	2	2		
	$< 10^{-14}$	0	0	0		
	$< 10^{-9}$	348	313	272		
1.3	$< 10^{-10}$	94	85	85		
$k = 250$	$< 10^{-11}$	27	25	25		
$l = 3$	$< 10^{-12}$	4	3	3		
$m = 1$ or 2	$< 10^{-13}$	2	2	2		
	$< 10^{-14}$	0	0	0		
	$< 10^{-9}$	219	73	37	23	
2.1	$< 10^{-10}$	69	20	20	17	
$k = 40$	$< 10^{-11}$	18	5	5	5	
$l = 0$	$< 10^{-12}$	5	2	2	2	
$m = 3$	$< 10^{-13}$	2	2	2	2	
	$< 10^{-14}$	2	1	1	1	
	$< 10^{-15}$	1	1	1	1	
	$< 10^{-9}$	214	67	32		
2.2	$< 10^{-10}$	57	18	18		
$k = 40$	$< 10^{-11}$	20	4	4		
$l = 9$	$< 10^{-12}$	5	2	2		
$m = 3$	$< 10^{-13}$	3	1	1		
	$< 10^{-14}$	1	1	1		
	$< 10^{-9}$	766	441	361		
3.1	$< 10^{-10}$	235	126	126		
$k = 1$, 2 or 3	$< 10^{-11}$	70	29	26		
$l = 0$, 3, 9 or 50	$< 10^{-12}$	19	6	6		
$m = 1$, 2 or 3	$< 10^{-13}$	6	5	5		
(All TEB cand.)	$< 10^{-14}$	3	2	2		
	$< 10^{-15}$	2	1	1		

5.1.1 Observations by method 1.1-1.3

Method 1.1-1.3 sort out bright signals spread over one or two 20 ms bins. According to Table 5.1, method 1.1 sorts out 509 signals in search A, with probability value less than 10^{-9}. This p-value corresponds to one false trigger per year. By sending those 509 candidates through the search B algorithm, 254 are still left in the data set. This means that there are 255 candidates in search A that does not meet the criterion given in search B. This is as expected because search B is a more stringent criterion than search A, where we try to compensate for fluctuations in the observed background. Finally, when we apply the search C criteria, 26 candidates fail, and 228 candidates pass. By doing three more and more stringent searches, A to C, with the method 1.1 criterion, the number of candidates has been reduced from 509 to 228. Examples of bright one bin and two bins candidates, are presented in Figure 5.1.

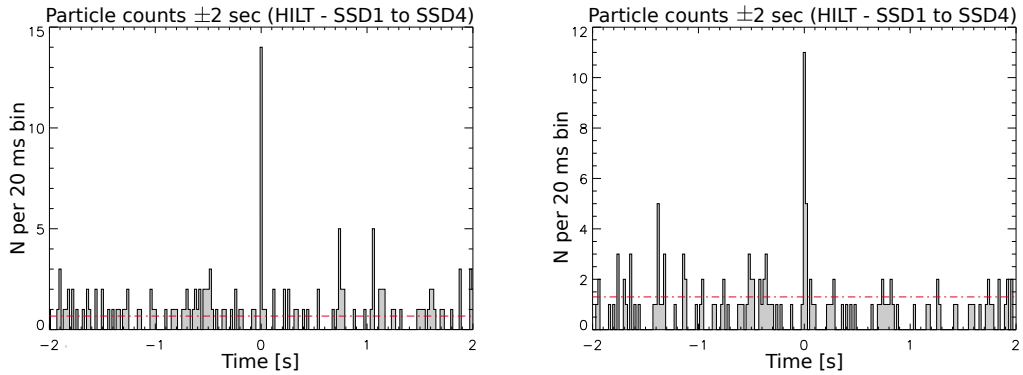

(a) Bright one bin signal (b) Bright two bins signal

Figure 5.1: One and two bins events plotted as counts per 20 ms bin, 2 sec before and after a significant signal measured by HILT on SAMPEX. (a) A bright one bin signal measured when SAMPEX passed over Pakistan (lon. 70.08°, lat. 29.29°) on the 11th January 2012, 08:43:54.16 UTC. 14 counts and a background count rate of 0.67 counts per 20 ms were observed. (b) A bright two bins signal where measured when SAMPEX passed over the Indian Ocean (lon. 74.32°, lat. -13.36°) on the 25th May 2012, 00:49:05.48 UTC. 16 counts and a background count rate of 1.3 counts per 40 ms were observed.

Applying method 1.1-1.3, we find many of the same candidates. After search C is applied for all methods (1.1-1.3), 164 candidates are common. This means that 164 of 228 candidates found by method 1.1, 273 found by method 1.2 and 272 found by method 1.3, are found by all these methods. It is reasonable that most of the candidates found by method 1.1-1.3 should be common events, since all these methods are based on one or two bins ROI, but with different selections of background bins (k and l in Table 4.1).

5.1.2 Observations by method 2.1-2.2

Method 2.1-2.2, that exclusively search in three bins ROI, find fewer events than method 1.1-1.3, but still a relatively large number of candidates. This is as expected because a one bin (or two bins) candidate has to be brighter to be observed by method 2 than by method 1 (see Section 4.1.1). Method 2.1 and 2.2 are much the same algorithm. Because of this, most of the detected candidates are common. Method 2.1 finds 219 three bins signals in search A, with probability value less than 10^{-9}. Of these, 73 fulfill the criterion in search B, and after search C, 37 candidates passed, by the same reason as for method 1. For comparison, method 2.2 finds 214, 67 and 32 candidates for respectively search A, B and C. Of the 37 candidates in method 2.1 and 31 candidates in method 2.2, 23 candidates are common for these methods.

The number of candidates that have been found by all methods used, 1.1-2.2, that meet all search criteria A, B and C, with probability values less than 10^{-9}, is only five.

5.1.3 Observations by method 3.1

Method 3.1, in Table 4.1 and 5.1, is a combination of all methods used. In the data set generated by this method, it has been taken into account that candidates that overlap in time have to be sorted, merged, and counted only as one single candidate. This data set consists of 361 candidates, with probability value less than 10^{-9}, that meet all the criteria A to C.

Figure 5.2 shows all candidates found by method 3.1. Figure 5.2a presents the candidates versus probability value bins. Most all of the candidates have probability values between 10^{-9} and 10^{-10}, where all searches A to C are done. The number of candidates falls of quickly with decreasing probability value. This is as expected, the number of events should fall of exponentially with decreasing p-value in a Poisson distribution. Figure 5.2b presents the number of candidates per day of the year. The candidates are spread out through the whole year. The last candidate found, is on the day of the year 308 (3 November, 2012), 10 days before SAMPEX re-entered the Earth's atmosphere. Days without any candidates, before day 308, are a combination of days without HILT data and days with HILT data but without any candidates. The number of candidates found per day is mostly between 2 and 4 candidates per day, with a maximum of six candidates per day (day of year 64 / 4 March 2012).

The global map in Figure 5.3, presents the satellite position (black), the magnetic foot point in the northern hemisphere (red) and in the southern hemisphere (blue), for each observed candidate. The histograms below and to the right show the

longitude and the latitude distribution of all observed candidates (method 3.1). As seen in the plots, the 361 TEB candidates are more or less uniform distributed. This may indicate that most of the candidates are something else than TEBs, as the distribution shown in Figure 2.29 is more expected. Both TEBs and TGFs are correlated to high lightning activity regions, e.g. South America, Africa and East Asia (see Section 2.5.4) [*Xiong et al.*, 2012]. Uniform distributed events, like cosmic ray showers, are thought to generate TEB mimic signals. This is more discussed in Section 6.4.

Notice, in the test we only check for signal above background variation. It gives that the number is as large as ~ 350 for only accepting one false positive per year. This indicate that we have other events than TEBs.

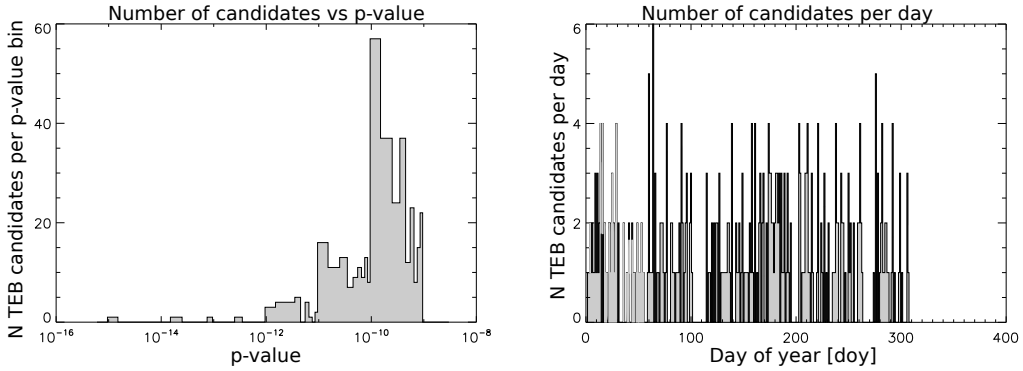

(a) Number of events per p-value bin (b) Number of events per day of year bin

Figure 5.2: (a) Number of method 3.1 TEB candidates per p-value bin and (b) number of TEB candidates per day of year bin in 2012.

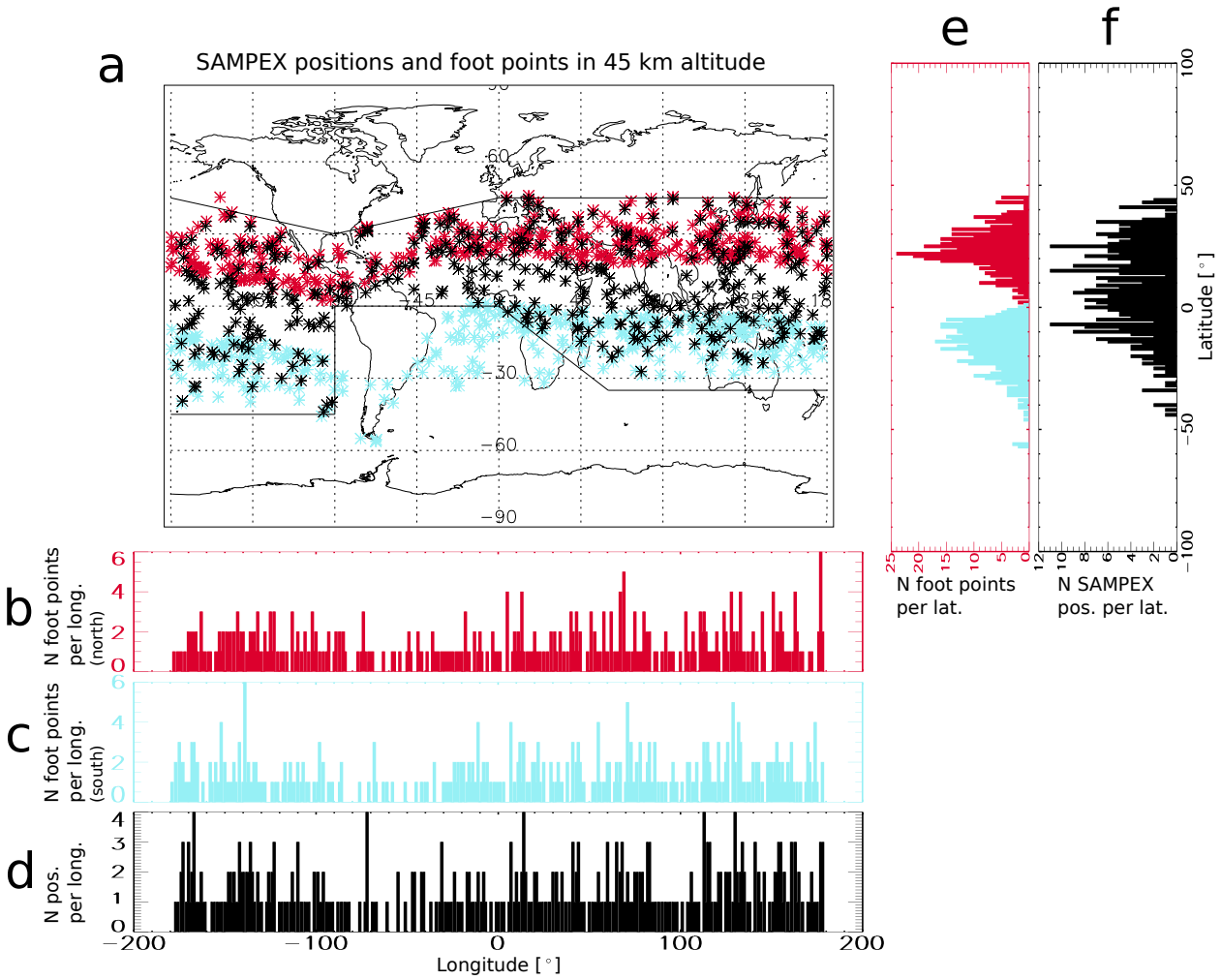

Figure 5.3: All SAMPEX candidates found by method 3.1 that fulfill all criteria A to C. (a) Black asterisks are SAMPEX positions when significant signals are observed. Black solid lines are the limits of the TEB search region. Red and blue asterisks are respectively northern and southern foot points. (b) The number of northern foot points per longitude bin. (c) The number of southern foot points per longitude bin. (d) The number of SAMPEX positions per longitude bin. (e) Number of northern (red) and southern (blue) foot points per latitude bin. (f) Number of SAMPEX positions per latitude bin.

5.1.4 Candidates that are removed

In the data sets generated by the TEB search algorithm, several events are obviously something else than a TEB event. Some events are removed because they were measured when SAMPEX passed outside the geographical TEB search region (see Section 4.2). Other events are removed because they obviously are something else than TEBs (see Section 4.3). Examples of such events are presented in Figure 5.4. Figure 5.4a is a signal measured by HILT on the October 2nd 05:31:47 UTC when the satellite passed over North America. It is thought to be correlated to high particle fluxes in the radiation belts. This one is removed because the satellite passed outside the TEB search region, near the polar region in the northern hemisphere. Figure 5.4b is a signal measured by HILT on the September 3rd 18:58:26 UTC when the satellite passed over Indonesia. This candidate is removed because of strong gradients in the background count rate (see Section 4.3).

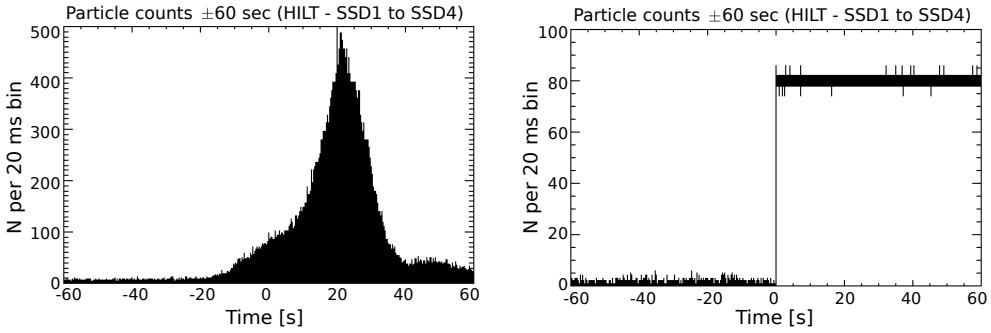

(a) October 2nd 2012, 05:31:27 UTC (b) September 3th 2012, 18:58:26 UTC

Figure 5.4: Two examples of signals measured by HILT that are removed by different criteria. (a) A more than one minute long high count rate event, measured when SAMPEX passed over North America, outside the geographical TEB search region (see Section 4.2). It is thought to be correlated to the radiation belts. (b) A more than one minute long high count rate event, measured when SAMPEX passed over Indonesia. This candidate was removed because of strong gradients in the background count rate. It has to be something else than TEBs.

5.2 Lightning observations

For all observed TEB candidates, that are presented in Table 5.1, the magnetic field line that passes through the satellite at the time of observation, has been traced down to 45 km altitude. This is described in Section 4.4. In this section the search for lightning, WWLLN data, in the foot point areas are presented.

The lightning search algorithm has generated a data set that contains WWLLN detected sferics. The data set consists of all sferics detected in a 500 km radius of the northern and the southern foot point and 500 km radius of the satellite nadir point, within a time interval of 10 minutes before and after the time when HILT measures a significant signal.

For each sferic of interest, information is stored. The offset in time between the sferic detection and the HILT detection, together with the distance between the foot point and the sferic, are the main components. Whether the sferic is observed in the northern, southern or in the nadir point is important for calculating the speed-of-light propagation delay along the magnetic field line.

For all the 361 TEB candidates found by method 3.1, 16 680 sferics have been marked as interesting. 6 646 of those sferics are located in northern foot point regions, 5 132 in southern and 4 902 in the nadir point region of the satellite. Searching for lightning in a ±10 minute time interval within a radius of 500 km is not necessarily finding the actual lightning stroke that generated the TEB, but it indicates whether there were thunderstorms in the actual region or not. This is also used to estimate local lightning rates around foot points (sferic $\cdot$ km$^{-2} \cdot$ s^{-1}), as we will see later in Section 6.5.

5.3 Results of the SAMPEX - WWLLN comparison

In this section the results of the SAMPEX - WWLLN comparison will be presented, with examples of TEB candidates. This section is divided in four parts:

1. WWLLN match ($\Delta t = 1$ s and $\Delta x \leq 250$ km)
2. Associated lightning activity ($\Delta t = 60$ s and $\Delta x \leq 250$ km)
3. Null hypothesis ($\Delta t = 60$ s and $\Delta x \leq 250$ km)
4. No associated lightning activity ($\Delta t = 60$ s and $\Delta x \leq 250$ km)

The different criteria are described more detailed in Section 4.5.

5.3.1 WWLLN match

One of all 361 TEB candidates meets the WWLLN match criterion. At least one sferic has to be detected within a radius of 250 km from the foot point, within the time accuracy interval of the HILT data ($\Delta t = \pm 1$ s). This event is presented in Section 5.3.1.1.

5.3.1.1 28 May 2012 - 07:43:25.52 UTC

On the 28th of May 2012, 07:43:25.52 UTC, SAMPEX passed east of the Philippines (lon. 143.27°, lat. 11.32°). HILT detected 12 counts in a two bins wide ROI, with a background count rate of 0.77 counts per 40 ms (see Figure 5.5). This corresponds to $P_A = 4.80 \cdot 10^{-11}$ for the search A and $P_B = 3.36 \cdot 10^{-10}$ for the search B. Both $P_{C_A} = 9.60 \cdot 10^{-11}$ and $P_{C_B} = 6.72 \cdot 10^{-10}$ are less than 10^{-9}, and this candidate fulfill all criteria in search A to C. This candidate is found to be most significant by using method 1.1 and all the presented p-values are estimated by this method. It is also found by method 1.3 search A to C, but for method 1.2 it is found in search A and B, but does not meet the search C criterion. Method 2.1 and 2.2 did not find this candidate in their search C, because 12 (0+5+7) or 14 (5+7+2) counts were not enough for three bins (see Figure 5.5a and Section 4.1.1). What kind of methods that found the candidate is presented in Table 5.2.

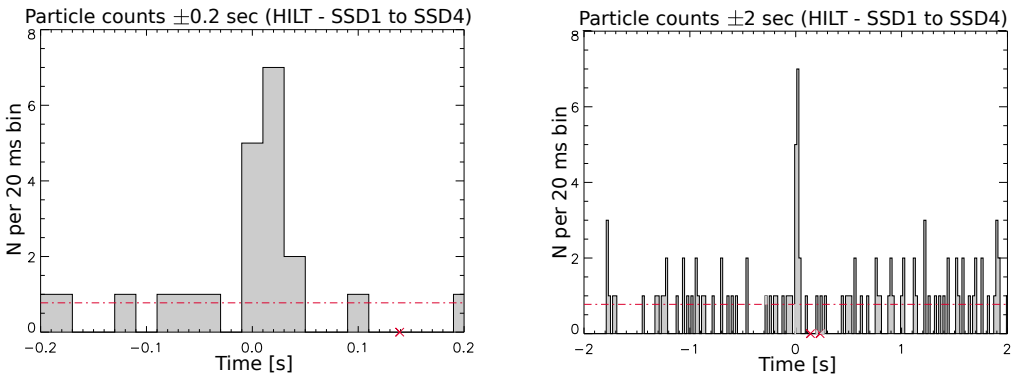

(a) 20 ms bin particle count by HILT ±0.2 sec

(b) 20 ms bin particle count by HILT ±2 sec

Figure 5.5: Number of particles per 20 ms bin measured by HILT when SAMPEX passed east of the Philippines (lon. 143.27°, lat. 11.32°) on the 28th of May 2012, 07:43:25.52 UTC.

Table 5.2: The TEB candidate found on the 28th of May 2012, 07:43:25.52 UTC is found by methods and search criteria marked with ×.

Method	Search A	Search B	Search C
1.1	×	×	×
1.2	×	×	
1.3	×	×	×
2.1	×	×	
2.2	×		

In Figure 5.6a the satellite position, corresponding magnetic field line, and the two foot points are presented. Figure 5.6b is a zoomed cut of Figure 5.6a, where the red

crosses are lightning strokes in a radius of 500 km and during a time period of 10 minutes before and after the actual event time. Within this time period and radius, there are 124 lightning strokes detected by WWLLN around the southern foot point (lon. 142.38°, lat. −5.08°). Correspondingly, there were 2 strokes in the northern foot point (lon. 143.32°, lat. −20.33°) and 0 strokes around the satellite nadir point (lon. 143.27°, lat. 11.33°).

At 07:43:25.662697 UTC, WWLLN detected a sferic (lon. 143.44°, lat. −4.72°) 125 km from the southern foot point. The tracing of the magnetic field line from the satellite down to 45 km altitude leads to an arc length of 1 970 km, that corresponds to a speed-of-light propagation delay of 6.57 ms. As mentioned in Section 4.5, the first electrons that arrives the satellite is thought to propagate with a velocity near the speed of light with a small pitch angle [*Cohen et al.*, 2010]. According to Equation 2.2, 1.0 MeV electrons propagates with velocity $\sim 0.94c$ and 10 MeV electrons with velocity $\sim 0.99c$. The speed-of-light propagation delay is therefore assumed to be the lower limit for the propagation time between the foot point and the satellite.

At 07:43:25.753798 UTC, 91.1 ms after the sferic described above, WWLLN detected another sferic (lon. 143.48°, lat. −4.75°) 128 km from the southern foot point. Of all the TEB candidates found by method 3.1, these two sferics are the only ones within a radius of 250 km from the foot point, in connection with a TEB candidate within ±1 s, as given by Equation 4.7 ($\Delta t = 1$ s). The reliability of this WWLLN matched TEB candidate is discussed in Section 6.5.

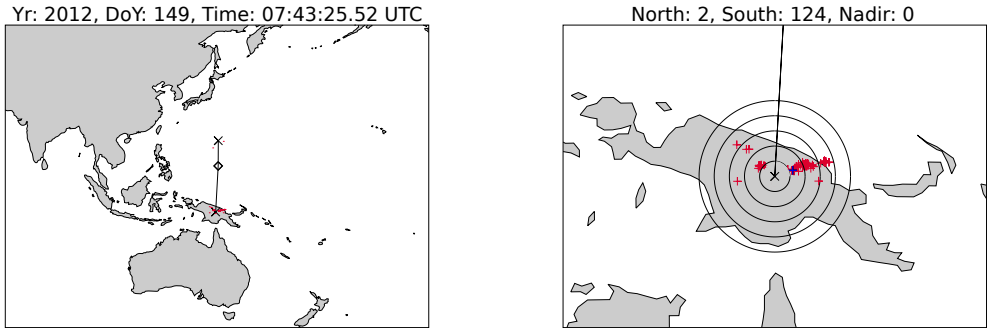

(a) Large scale map (b) Southern foot point

Figure 5.6: (a) The SAMPEX position, magnetic field line and the two foot points plotted for the 28th of May 2012, 07:43:25.52 UTC candidate. (b) The southern foot point plotted with red asterisks representing WWLLN detections within 500 km and ±10 min. The two sferics that fulfill the WWLLN match time criterion are represented as blue asterisks. The black solid circles, have their centers in the foot point and do have radii of 100 km, 200 km, 300 km, 400 km and 500 km. North, South and Nadir are numbers of detected sferics in these three foot points.

5.3.2 Associated lightning activity

Associated lightning activity is in this thesis defined as lightning strokes detected by WWLLN within a radius of 250 km and a time interval of ±1 min (see Section 4.5.2). In percent, how many of the TEB candidates for each method that fulfill this lightning criteria, is presented in Table 5.3. For all the TEB candidates found (method 3.1, search C), 38 of 361 do have associated lightning activity, that is 10.53%. Examples of such TEB candidates are presented in Section 5.3.2.1 and 5.3.2.2. A comparison between the associated lightning activity and the null hypothesis is discussed in Section 6.2.

Table 5.3: Ratio between candidates with associated lightning activity and the number of all candidates per method and search, in percent (%). Associated lightning activity is defined as at least one WWLLN detection within ±60 sec, within a radius less than 250 km from the foot point. The numbers in the parenthesizes are the number of candidates with associated lightning activity. The total number of candidates per methods and search is presented in Table 5.1.

Method	$P(N \geq n\|b)$	Search A	Search B	Search C	Common	Common
1.1	$< 10^{-9}$	11.20 (57)	11.02 (28)	11.40 (26)	11.59 (19)	60.00 (3)
1.2	$< 10^{-9}$	12.36 (44)	12.30 (39)	10.62 (29)		
1.3	$< 10^{-9}$	12.36 (43)	12.77 (40)	11.77 (32)		
2.1	$< 10^{-9}$	17.35 (38)	19.18 (14)	21.62 (8)	21.74 (5)	
2.2	$< 10^{-9}$	17.76 (38)	14.93 (10)	18.75 (6)		
3.1	$< 10^{-9}$	12.14 (93)	11.34 (50)	10.53 (38)	-	-

5.3.2.1 23 January 2012 - 14:18:31.78 UTC

On the 23 January 2012, 14:18:31.78 UTC, SAMPEX passed east of Taiwan (lon. 131.64°, lat. 22.90°). HILT detected 14 counts in a three bin wide ROI. The background count rate was 1.125 counts per 60 ms (see Figure 5.7). This candidate is most significant by using method 2.1, that gives a p-value of $P_A = 2.09 \cdot 10^{-11}$ in search A and $P_B = 2.67 \cdot 10^{-10}$ in search B. Search C is fulfilled with $P_{C_A} = 6.28 \cdot 10^{-11}$ and $P_{C_B} = 8.02 \cdot 10^{-10}$. It can be seen in Table 5.4 that this candidate has been found by mostly all methods, except search C in method 1.2.

The position of the satellite and the two magnetic foot points are plotted in Figure 5.8a. The tracing of the magnetic field line from the satellite down to 45 km altitude leads to an arc length of 580 km to the northern foot point (lon. 131.29°, lat. 27.54°) and 4 560 km to the southern foot point (lon. 131.20°, lat. -11.56°). All lightning strokes detected in a 500 km radius, ±10 min, in the southern foot point region, are

plotted in Figure 5.8b. The number of detected strokes in the southern foot point is 1 508, with correspondingly zero strokes both in the northern foot point or around the satellite nadir point. 18 of those lightning strokes fulfill the defined lightning activity criteria (radius less than 250 km, ±1 min).

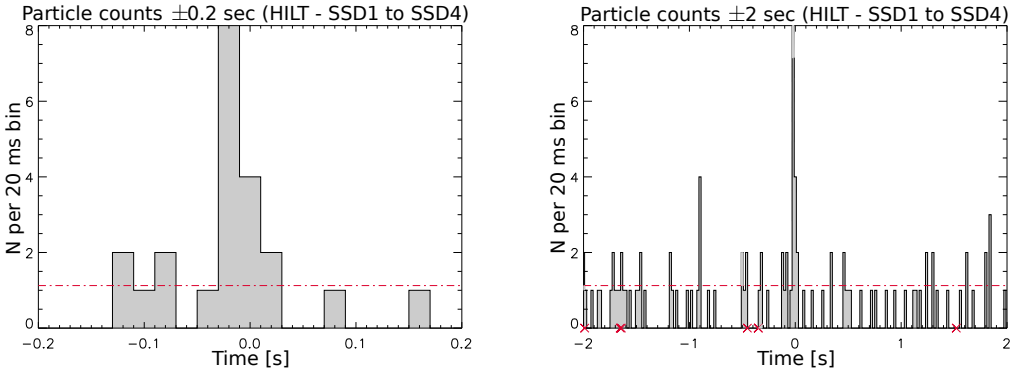

(a) 20 ms bin particle count by HILT ±0.2 sec

(b) 20 ms bin particle count by HILT ±2 sec

Figure 5.7: Number of particles per 20 ms bin measured by HILT when SAMPEX passed east of Taiwan (lon. 131.65°, lat. 22.91°) on the 23rd of January 2012, 14:18:31.78 UTC.

Table 5.4: The TEB candidate found on the 23rd of January 2012, 14:18:31.78 UTC is found by methods and search criteria marked with ×.

Method	Search A	Search B	Search C
1.1	×	×	×
1.2	×	×	
1.3	×	×	×
2.1	×	×	×
2.2	×	×	×

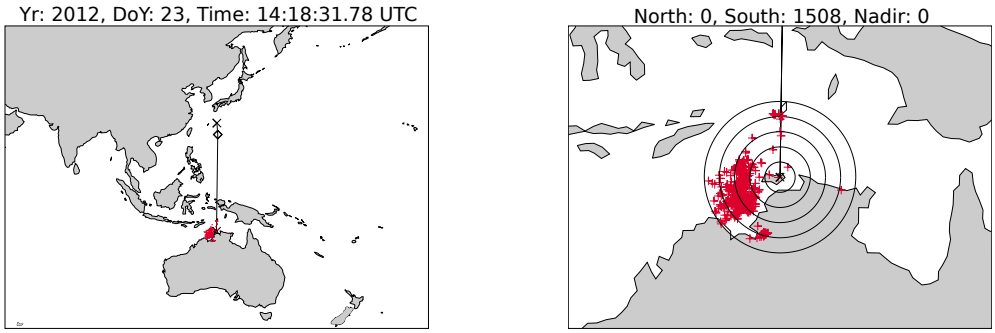

(a) Large scale map (b) Southern foot point

Figure 5.8: (a) The SAMPEX position, magnetic field line and the two foot points plotted for the 23rd of January 2012, 14:18:31.78 UTC candidate. (b) The southern foot point plotted with red asterisks representing WWLLN detections within 500 km and ±10 min. The black solid circles, have their center in the foot point and do have radii of 100 km, 200 km, 300 km, 400 km and 500 km. North, South and Nadir are numbers of detected sferics in these three foot points.

5.3.2.2 19 September 2012 - 01:41:43.42 UTC

On the 19 September 2012, 01:41:43.42 UTC, SAMPEX passed east of Papua New Guinea (lon. 163.31°, lat. -2.00°). HILT detected 10 counts in a one bin wide ROI. The background count rate was 0.51 counts per 20 ms (see Figure 5.9). This candidate is most significant by using method 1.2, that gives a p-value of $P_A = 1.92 \cdot 10^{-10}$ in search A and $P_B = 2.33 \cdot 10^{-10}$ in search B. Since the counts are in one bin, the p-values in search C is the same as for A and B. It can be seen in Table 5.5 that this candidate has been found by all methods 1.1-1.3, but not by method 2 at all. This is because both 10, 11 (10+1) or 14 (10+1+3) counts, were too low for three bins ROI (see Figure 5.9a and Section 4.1.1).

The position of the satellite and the two magnetic foot points are plotted in Figure 5.10a. The tracing of the magnetic field line from the satellite down to 45 km altitude leads to an arc length of 2 680 km to the northern foot point (lon. 165.91°, lat. 19.96°) and 789 km to the southern foot point (lon. 162.25°, lat. -9.06°). All lightning strokes detected in a 500 km radius, ±10 min, in the northern foot point region, are plotted in Figure 5.10b. The number of detected strokes in the northern foot point is 561, with correspondingly zero strokes both in the southern foot point and around the satellite nadir point. Of those lightning strokes 46 fulfill the defined lightning activity criteria (radius less than 250 km, ±1 min).

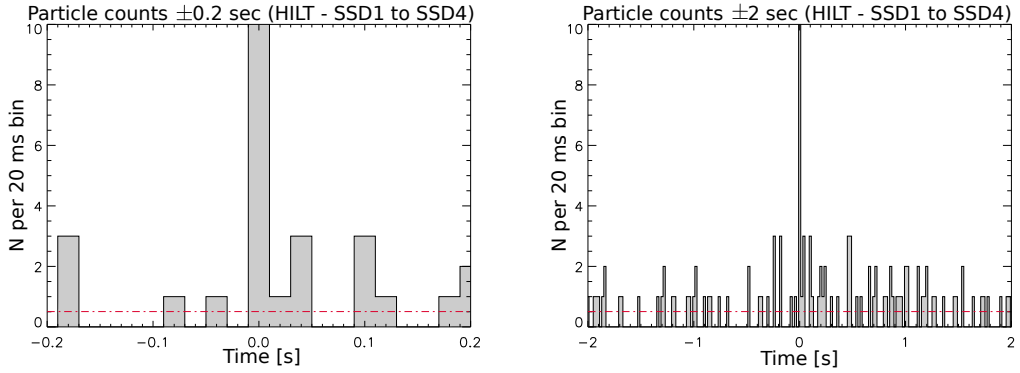

(a) 20 ms bin particle count by HILT ±0.2 sec

(b) 20 ms bin particle count by HILT ±2 sec

Figure 5.9: Number of particles per 20 ms bin measured by HILT when SAMPEX passed east of the Papua New Guinea (lon. 163.31 °, lat. -2.00 °) on the 19th of September 2012, 01:41:43.42 UTC.

Table 5.5: The TEB candidate found on the 19th of September 2012, 01:41:43.42 UTC is found by methods and search criteria marked with ×.

Method	Search A	Search B	Search C
1.1	×	×	×
1.2	×	×	×
1.3	×	×	×
2.1			
2.2			

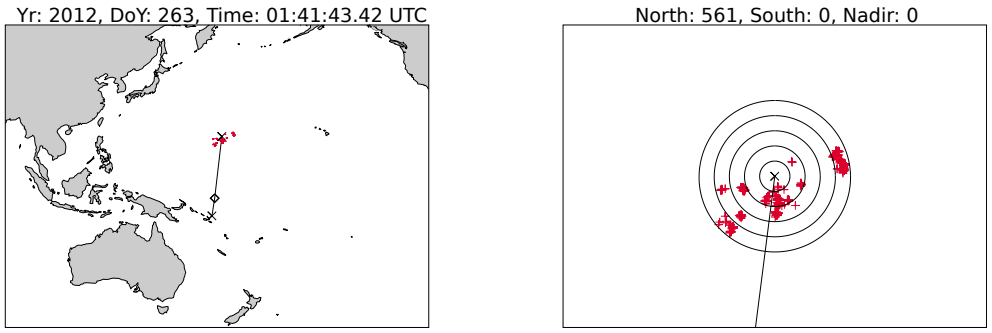

(a) Large scale map

(b) Northern foot point

Figure 5.10: (a) The SAMPEX position, magnetic field line and the two foot points plotted for the 19th of September 2012, 01:41:43.42 UTC candidate. (b) The northern foot point plotted with red asterisks representing WWLLN detections within 500 km and ±10 min. The black solid circles, have their centers in the foot point and do have radii of 100 km, 200 km, 300 km, 400 km and 500 km. North, South and Nadir are numbers of detected sferics in these three foot points.

5.3.3 Null hypothesis observations

The null hypothesis algorithm has generated a data set of the SAMPEX positions and corresponding foot points at arbitrary moments. One million moments were chosen in 2012 with a pseudo-random number generator in IDL. Of those moments, 377 513 moments corresponded to SAMPEX positions inside the TEB search window. Some moments were removed from the null data set because they were overlapped in time with moments where HILT measured a significant signal, or overlapped with other moments in the null data set. In the end, after data sorting, the null hypothesis data set consists of 360 051 moments with corresponding satellite and foot point positions. Each of these positions are, as was done for all the TEB candidates, searched for lightning.

The null lightning data set consists of all lightning strokes in a radius of 500 km from both foot points in a time interval of ±10 min, and the same parameters around the satellite nadir point. In total, the data set consists of 15 107 710 WWLLN detected lightning strokes. 6 403 367 of those are detected in northern foot points, 3 452 516 are detected in the southern foot points, and 5 251 827 strokes are detected around the satellite nadir point. Of the 360 051, 37 442 arbitrary moments in the null candidate data set do have associated lightning activity within a radius of 250 km from the foot point, ±60 s. This corresponds to an associated lightning activity rate of 10.40%. By this, 10.40% of all the null candidates do have associated lightning activity in at least one foot point. The null hypothesis is a test to see if there are more associated lightning in foot point regions when HILT detects significant signals, than when we just take arbitrary SAMPEX positions. This is more discussed in Section 6.2.

5.3.4 No associated lightning activity

No associated lightning activity, are those TEB candidates where WWLLN does not detect any lightning strokes within a radius of 250 km from the foot point, in a time interval ±1 min. Of the 361 candidates in method 3.1 search C, 323 candidates have no associating lightning activity. This is 89.5% of all candidates observed in 2012. The number of candidates that have no WWLLN detections at all within a radius of 500 km and ±10 min, is 28 (7.8%). A candidate with no associated lightning activity is presented in Section 5.3.4.1.

5.3.4.1 24 January 2012 - 18:57:11.80 UTC

On the 24th of January 2012, 18:57:11.80 UTC, SAMPEX passed over The Pacific Ocean, west of Mexico (lon. 243.70°, lat. 4.79°). This can be seen in Figure 5.12a. A bright two bins wide ROI peak with 15 counts is observed in the HILT data (see Figure 5.11). This candidate is most significant by using method 1.1. The observed background count rate is estimated to 1.00 counts per 40 ms, that gives the p-values $P_A = 3.02 \cdot 10^{-13}$ and $P_B = 3.04 \cdot 10^{-12}$. In search C the p-values are respectively $P_{C_A} = 6.04 \cdot 10^{-13}$ and $P_{C_B} = 6.08 \cdot 10^{-12}$, that fulfill the search criteria. This candidate is one of five candidates, that is found by all methods and all search criteria (see Table 5.6).

This is an example of a candidate that has no lightning activity at all, in a radius of 500 km around the foot points and the nadir point, in a time interval of ±10 min. The tracing of the magnetic field line from the satellite down to 45 km altitude leads to an arc length of 840 km to the northern foot point (lon. 244.70°, lat. 11.23°) and 3 440 km to the southern foot point (lon. 238.54°, lat. -22.21°). For the southern foot point, this can be seen in Figure 5.12b.

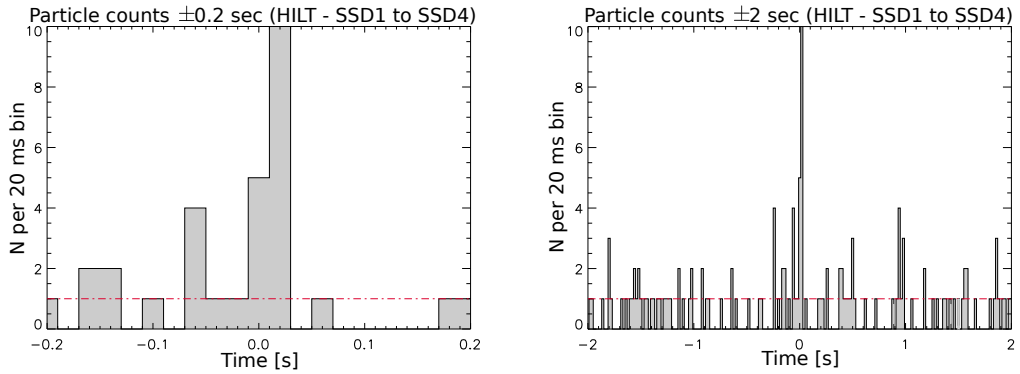

(a) 20 ms bin particle count by HILT ±0.2 sec

(b) 20 ms bin particle count by HILT ±2 sec

Figure 5.11: Number of particles per 20 ms bin measured by HILT when SAMPEX passed over The Pacific Ocean, west of Mexico (lon. 243.70°, lat. 4.79°) on the 24th of January 2012, 18:57:11.80 UTC.

Table 5.6: The TEB candidate found on the 24th of January 2012, 18:57:11.80 UTC is found by methods and search criteria marked with ×.

Method	Search A	Search B	Search C
1.1	×	×	×
1.2	×	×	×
1.3	×	×	×
2.1	×	×	×
2.2	×	×	×

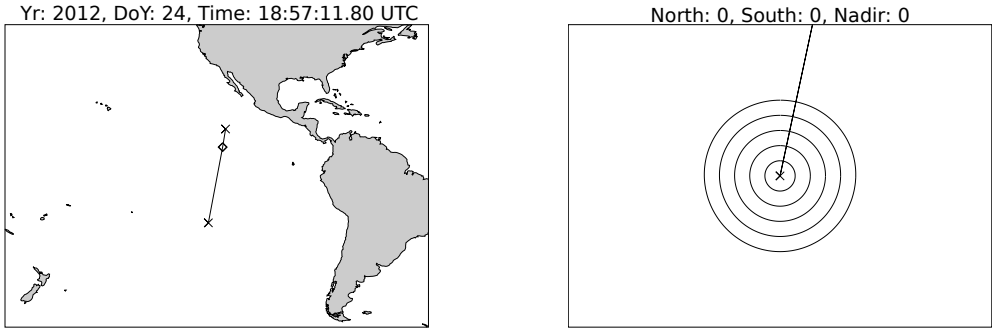

(a) Large scale map (b) Southern foot point

Figure 5.12: (a) The SAMPEX position, magnetic field line and the two foot points plotted for the 24th of January 2012, 18:57:11.80 UTC candidate. (b) The southern foot point plotted, where it can be seen that no lightning strokes are detected within 500 km and ±10 min. The black solid circles, have their center in the foot point and do have radii of 100 km, 200 km, 300 km, 400 km and 500 km. North, South and Nadir are numbers of detected sferics in these three foot points.

Chapter 6

Discussion

According to the observations presented in Chapter 5, there are many significant candidates that seem to be something else than fluctuations in the background radiation. The big question is what all these measured signals actually are? Are they TEBs or something else? In this chapter we will present a modeling analysis of how many TEBs SAMPEX is expected to detect, based on results from other satellites. We then include the associated lightning activity ratio and the null hypothesis into the discussion. We present and discuss suggestions of what other phenomena that could generate such signals. Finally, we discuss the reliability of the WWLLN match.

6.1 Expected TEB detection by SAMPEX

It is important to compare how many TEBs other satellites have detected and how many TEBs SAMPEX is expected to see. To address this we have modeled where a satellite, in a given orbit, is able to see TEBs. Here we will estimate the expected number of TEB detections by SAMPEX, by comparing with what Fermi has detected. We use Fermi because this is the satellite which has reported the largest number of TEBs (see Section 2.5.4.1). For this analysis we have six steps, that are briefly described later in this section, schematically presented in Figure 6.1 and discussed more detailed in the following sections.

Fermi has an orbit with inclination 25.58° and an altitude of $\sim 570\,\mathrm{km}$ [*Briggs et al.*, 2010]. SAMPEX had an inclination of $82\,^{\circ}$ and an altitude of $\sim 300\,\mathrm{km}$ (see Section 3.1 and Figure 3.1). These quantities together with the IGRF model (see Section 3.3) define where the satellite is magnetically connected at different locations. The foot points are set to be in an altitude of 45 km, as in the TEB search algorithm (see Section 4.4).

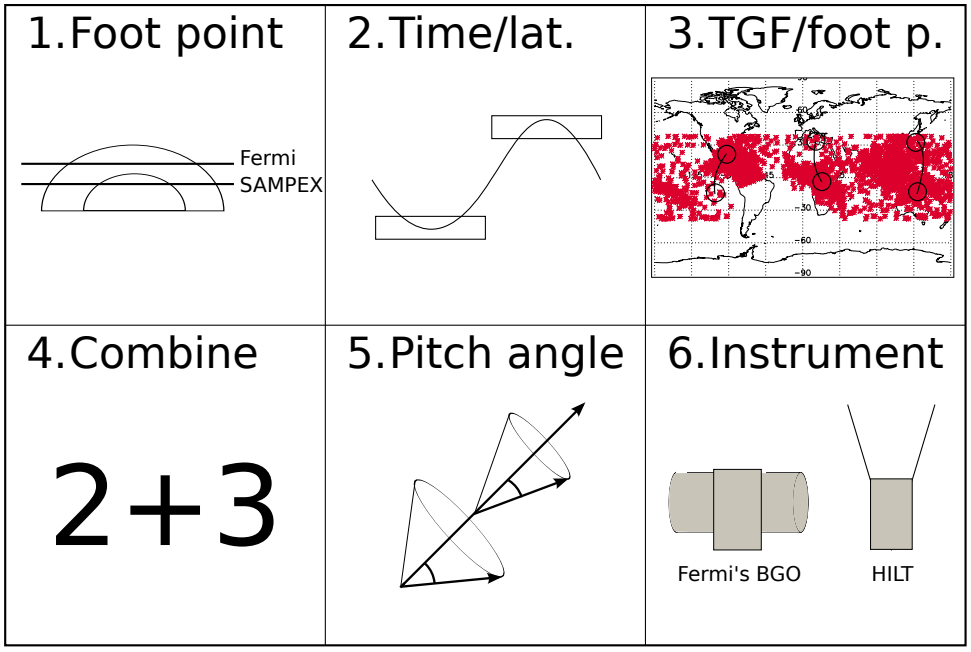

Figure 6.1: Schematically overview of the six stepped way to find the expected TEB detection by SAMPEX. Point 1 to 6 are briefly described in Section 6.1, and more detailed in the following sections.

As Fermi and SAMPEX have different orbit/inclination, altitude and detection sensitivity, we will address the following factors:

1. Different foot point regions with different properties. These are the foot point areas of the magnetic field lines the two satellites pass through, due to different altitudes.

2. Time spent per latitude bin per orbit, due to different inclinations.

3. TGF distribution compared to corresponding foot point regions. The expected TEB activity at these regions.

4. TGF weighted foot point regions, compared to the time spent per latitude bin per orbit. Combined point 2 and 3.

5. Pitch angle at different altitudes. Due to diverging field lines out of the atmosphere, the pitch angle distribution will be different for SAMPEX and Fermi.

6. Instrument sensitivity.

This is consistent with what kind of factors TEB detection is dependent on, mentioned in Section 2.5.4.3.

6.1.1 Different foot point regions

Figure 6.2 is a visualization of the regions a satellite is magnetically connected to, at a given position. It is a geomagnetic meridional cut of the Earth (parallel to the geomagnetic field lines). The geomagnetic field lines are represented as oval lines mirrored by the geomagnetic equator. The vertical dotted line is the geomagnetic equator and the two tilted lines represents the inclination angle or the cutoff search limits, depending on whether the inclination or the cutoff is at the highest latitude. The blue sectors are regions of foot points where the satellite is magnetically connected both in the northern and the southern hemisphere. This means that a TEB generated in the blue sectors can be detected when the satellite is located in the same or the opposite hemisphere. The green sectors are where the foot points are just connected to one satellite position. The area of the blue sectors has to be weighted twice as much as the area of the green, because the satellite is able to detect TEBs twice as often in those regions.

The red sectors in Figure 6.2 are foot point regions that are not magnetically connected to the satellite, when the satellite passes inside the TEB search region. Along the magnetic equator, the red region is where the satellite passes above the magnetic field lines that is connected to this region. The red regions at higher latitudes, in both hemispheres, are regions where the magnetic field lines go above the satellite position.

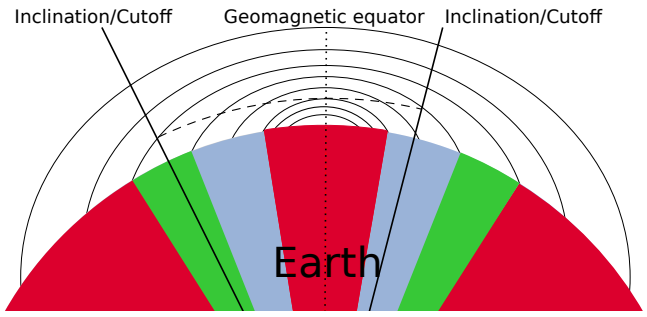

Figure 6.2: Geomagnetic meridional cut of the Earth (in the plane parallel to the geomagnetic field lines). The oval curves are geomagnetic field lines, the vertical dotted line is the geomagnetic equator and the tilted solid lines are the orbit inclination or the defined cutoff limits. The curved dashed line, between the two inclination/cutoff lines, represents the satellite orbit. The red sectors are regions that are not magnetically connected to the satellite when it is inside the TEB search region. Green sectors are regions that are magnetically connected to one potentially satellite position. Blue sectors are regions that are magnetically connected to two potentially satellite positions.

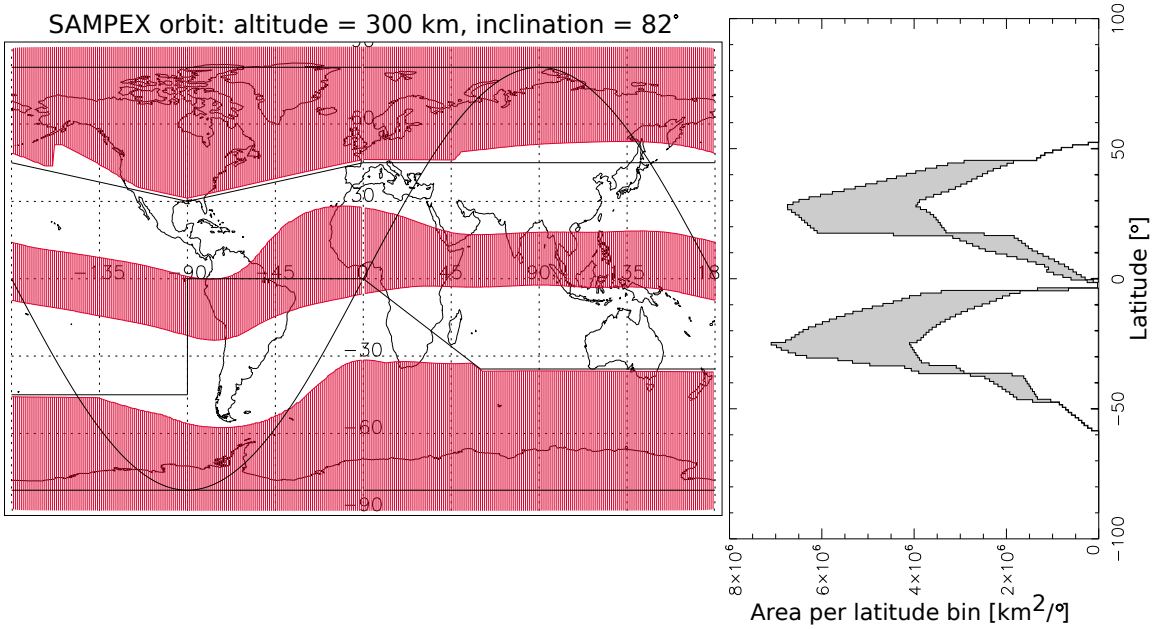

(a) SAMPEX: (White) $2.44 \cdot 10^8\,\mathrm{km}^2$, (Grey) $4.03 \cdot 10^8\,\mathrm{km}^2$.

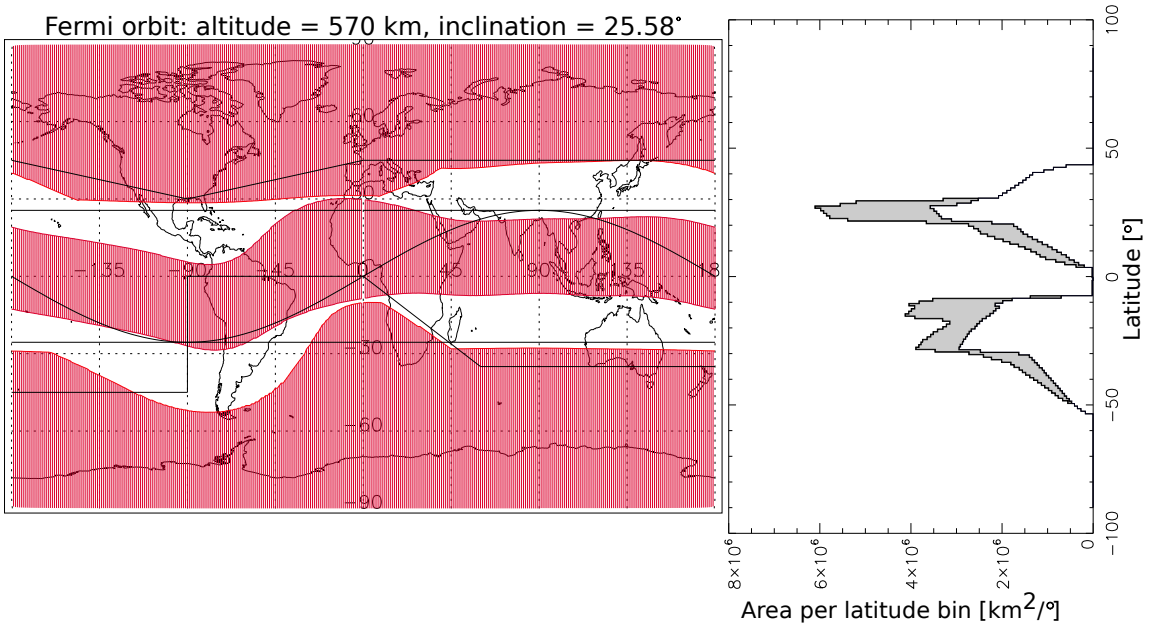

(b) Fermi: (White) $1.40 \cdot 10^8\,\mathrm{km}^2$, (Grey) $2.09 \cdot 10^8\,\mathrm{km}^2$.

Figure 6.3: (Left) Satellite orbit plotted together with the TEB search region limits. White regions are regions where the satellite is magnetically connected in one or two positions. Red regions are regions where the satellite has no magnetically connections, when it is inside the search region. (Right) Satellite area distribution per latitude bin. (White) Foot point area magnetically connected to the satellite. (Grey) Effective foot point area, weighted for regions where the satellite is connected to two possible positions, with a factor of two. The integral over all latitudes is presented in the sub captions.

Figure 6.3a and 6.3b are respectively the area of foot points seen by the SAMPEX and the Fermi satellite. The red shaded regions correspond to the red regions in Figure 6.2. It can be seen for both SAMPEX and Fermi, that it is an equatorial zone where the satellites do not have magnetically connection to. This is also the situation at higher latitudes. The white regions in Figure 6.3a and 6.3b are a combination of the green and blue regions in Figure 6.2, that is where the satellites are magnetically connected. The histograms to the right in Figure 6.3a and 6.3b represent the areas of the foot point regions. The white curves represent the area per latitude, that in total is $2.44 \cdot 10^8\,\mathrm{km}^2$ for SAMPEX and $1.40 \cdot 10^8\,\mathrm{km}^2$ for Fermi. The grey curves represent the effective area, and regions that are magnetically connected to two satellite positions are weighted twice as much as one-position regions. This effective area is $4.03 \cdot 10^8\,\mathrm{km}^2$ for SAMPEX and $2.09 \cdot 10^8\,\mathrm{km}^2$ for Fermi. These areas are all sub areas of the surface of a sphere with radius $R_E + 45\,\mathrm{km}$, where R_E is the mean Earth radius. SAMPEX detects an effective area of foot points that is a factor of $(4.03 \cdot 10^8\,\mathrm{km}^2/2.09 \cdot 10^8\,\mathrm{km}^2) \sim 1.93$ greater than the effective area seen by Fermi. This factor points in a favor to SAMPEX. This is a consequence of the low SAMPEX altitude in the end of its operation period.

6.1.2 Time spent per latitude bin per orbit

A satellite that orbits around the Earth with an inclination greater than 0°, is not uniformly latitude distributed during an orbit period. The satellite will be located at higher latitudes longer than at lower latitudes, as mentioned in Section 4.6. The sinusoidal orbit trajectories for two different inclinations, 82° and 25.58°, are presented respectively as black and red curves on the map in Figure 6.4 (left). The time spent per latitude bin relative to an orbit period, is presented in the histogram in Figure 6.4 (right). It can be seen that during an orbit the satellites are located longer at higher latitudes, than at lower and that Fermi is located much longer in the TEB search region than SAMPEX. In the modeling, this has been taken into account because it is important to see how much of an orbit period the satellite is magnetically connected to a blue, green or red region (referring to colored sectors in Figure 6.2).

Both the black and the red curve in the histogram in Figure 6.4 are for comparison reasons scaled such that the integral of the curves are equal to one. This is given by:

$$\int_{-90^\circ}^{90^\circ} t_{rel}(\phi)\, d\phi = 1, \tag{6.1}$$

where t_{rel} is the relative time per latitude and ϕ is the latitude angle. The unit will then be relative time per latitude bin.

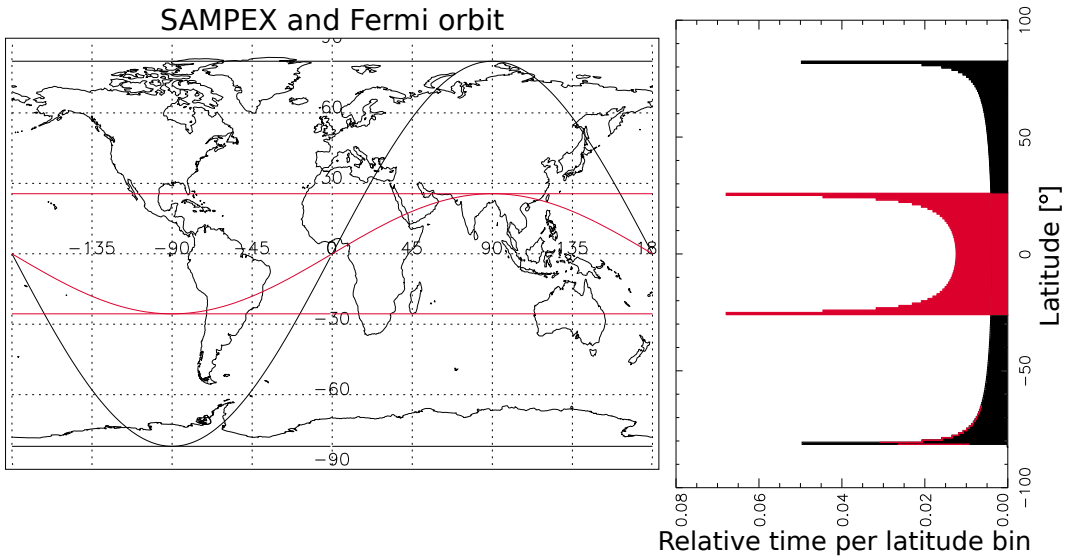

Figure 6.4: (Left) The Fermi (red) and SAMPEX (black) orbit plotted together. (Right) Relative time per latitude per orbit for SAMPEX (black) and Fermi (red). The integral of all latitudes in both the red and the black histogram is equal to one.

6.1.3 Global TGF distribution compared to foot point regions

The TGF distribution is now used as a measure of the TEB source distribution. Ideally, one would use the TEB distribution itself, but the detection rate of TEBs by Fermi is too low (see Section 2.5.4.3). Therefore, we use the TGF distribution, which should be fine as TEBs are thought to originate from the TGFs. Similar as lightning there are three areas where most of the TGFs are observed: America, Africa and East-Asia. This distribution corresponds well to the TEB distribution map, given in Figure 2.29. A RHESSI TGF catalog of more than three thousand TGFs [*Gjesteland et al.*, 2012] is used to predict how the TGF/TEB-source distribution is distributed in longitude and latitude. The catalog consists of more TGFs than presented by *Gjesteland et al.* [2012], but found by the same method. The TGF distribution is presented in Figure 6.5, plotted as red asterisks on the map. The number of TGFs observed per longitude and latitude bin are presented in histograms in the same figure.

If a TGF was observed in a region, where a TEB could have been observed by the satellite both in the northern and the southern hemisphere, it has to be weighted twice as much as if it was observed in a region corresponding to just one satellite position. Figure 6.6a and 6.6b are a comparison of the TGF distribution in longitude and latitude, weighted with the foot point area distribution for each of the satellites.

It can be seen in Figure 6.6a and 6.6b that SAMPEX includes more high rate TGF areas than Fermi does. The integral over all latitudes is $1.46 \cdot 10^{10}\,\mathrm{km}^2$ for SAMPEX and $5.92 \cdot 10^{9}\,\mathrm{km}^2$ for Fermi.

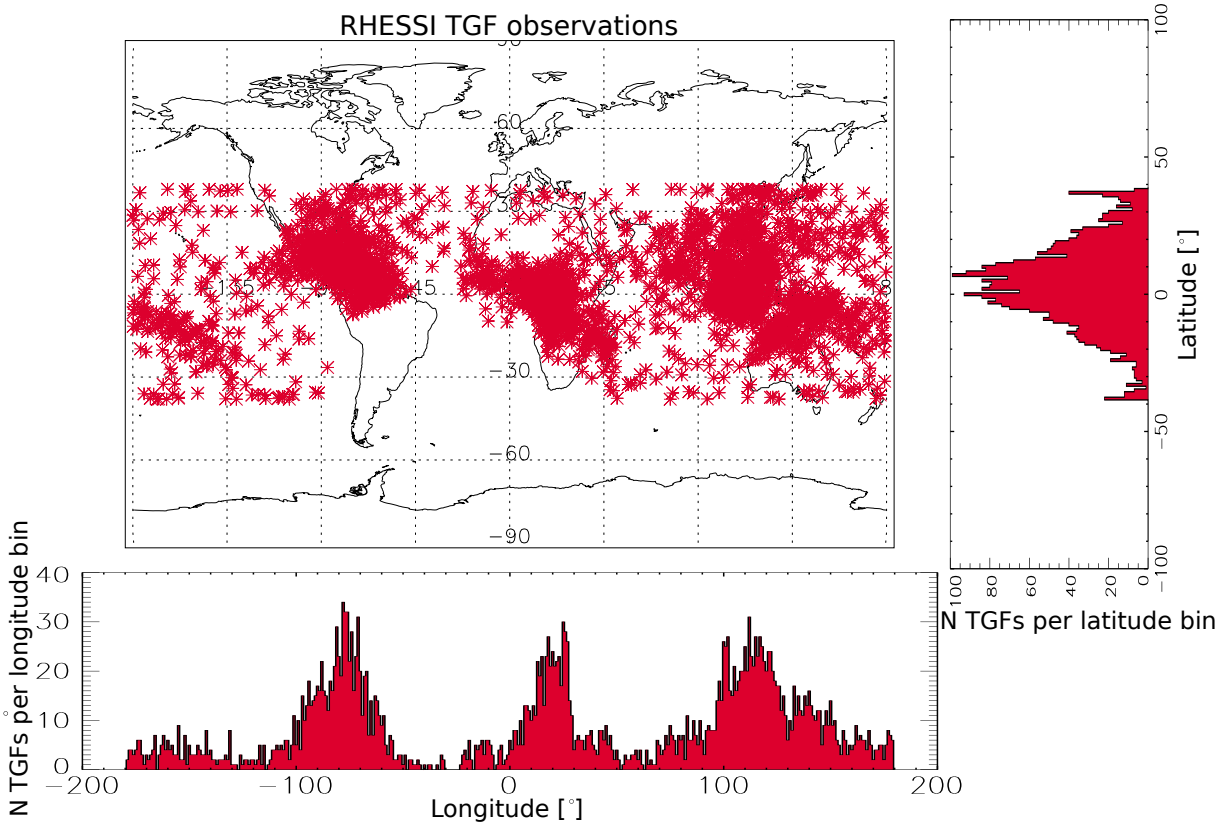

Figure 6.5: (Global map) 3013 TGFs observed by RHESSI [*Gjesteland et al.*, 2012], plotted as red asterisks. (Right) The number of observed RHESSI TGFs per latitude. (Below) The number of observed RHESSI TGFs per longitude.

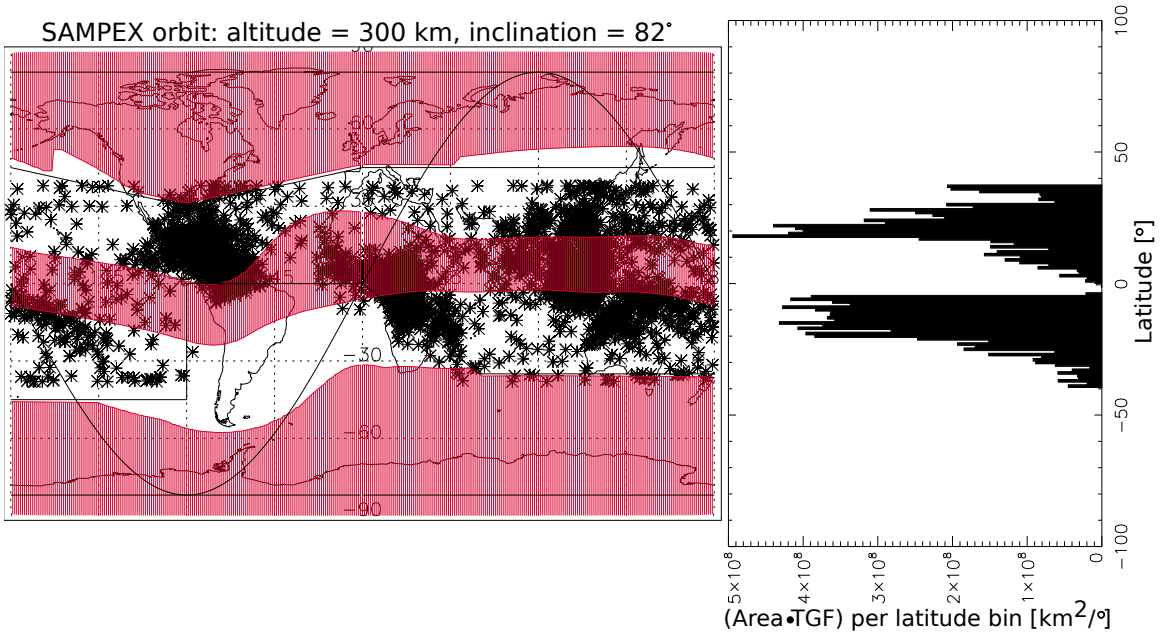

(a) SAMPEX: $1.46 \cdot 10^{10}\,\mathrm{km}^2$.

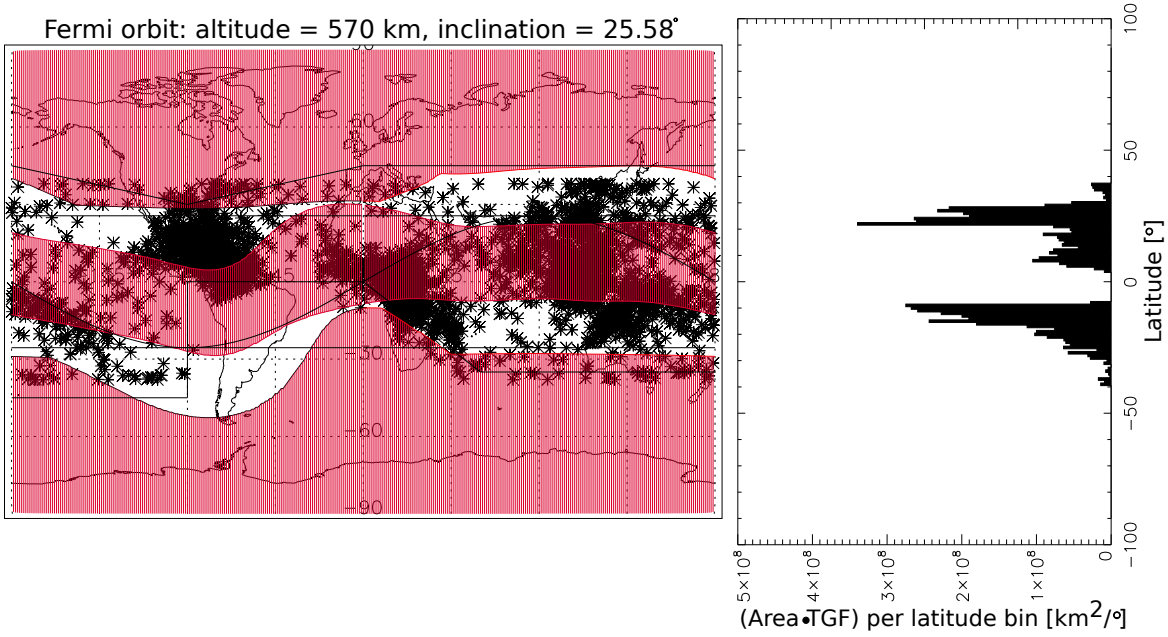

(b) Fermi: $5.92 \cdot 10^{9}\,\mathrm{km}^2$.

Figure 6.6: (Left) Satellite orbit plotted together with the TEB search region limits and the RHESSI TGF observations (black asterisks). White regions are regions where the satellite has magnetically connections in one or two positions. Red regions are regions where the satellite has no magnetically connections, when it is inside the TEB search region. (Right) Satellite area distribution compared to the TGF distribution. The integral over all latitudes is presented in the sub captions.

6.1.4 TGF weighted foot point regions compared to the time spent per latitude bin per orbit

Now we combine these three pieces of information to estimate the ratio of how many possible TEBs the two satellites can be exposed to. The TGF distributed foot point area, was presented in Figure 6.6a for SAMPEX and Figure 6.6b for Fermi, and the time per latitude distribution was presented in Figure 6.4.

The combined results are presented in Figure 6.7a for SAMPEX and Figure 6.7b for Fermi. The great difference in inclination angle between SAMPEX and Fermi is the factor that dominates. SAMPEX includes regions that Fermi does not see, which is favorable for SAMPEX. The problem is that due to the inclination angle of 82°, SAMPEX spends much of its time outside the TEB search region (see Section 4.2). In contrast, Fermi with its inclination of 25.58°, is located in the probable TEB region much longer of its orbit period than SAMPEX. The histograms in Figure 6.7 show how efficient the TEB search is per latitude. If we integrate over all latitudes, the result is $5.85 \cdot 10^7\,\mathrm{km}^2$ for the SAMPEX satellite. For the Fermi satellite this is, correspondingly to the SAMPEX case, presented in Figure 6.7b, where the integral over all latitude is $1.06 \cdot 10^8\,\mathrm{km}^2$. The fraction of these two quantities, Equation 6.2, gives a factor of ~ 0.55. Just based on these three factors, the SAMPEX satellite should be able to detect about half of the number of TEBs observed by Fermi.

$$\frac{\text{Area factor(SAMPEX)}}{\text{Area factor(Fermi)}} = \frac{5.85 \cdot 10^7\,\mathrm{km}^2}{1.06 \cdot 10^8\,\mathrm{km}^2} \sim 0.55 \tag{6.2}$$

However, there are a few more factors that have to be considered. The pitch angle at different altitudes and different instrument sensitivities, are included in the following sections.

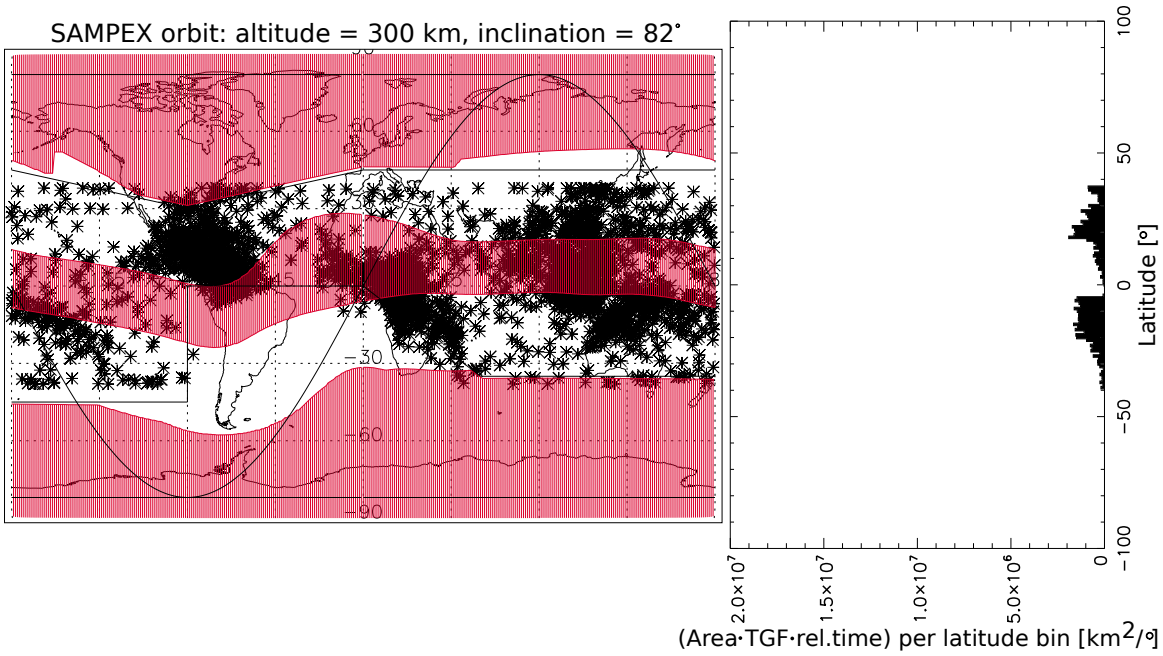

(a) SAMPEX: $5.85 \cdot 10^7\,\mathrm{km}^2$.

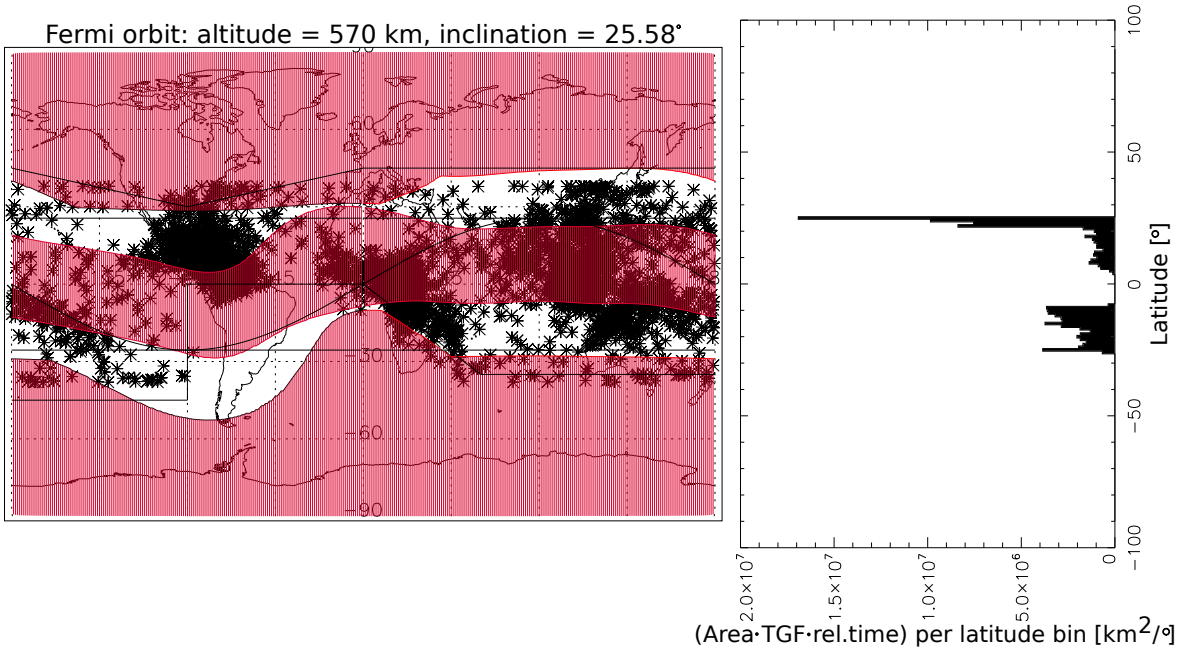

(b) Fermi: $1.06 \cdot 10^8\,\mathrm{km}^2$.

Figure 6.7: (Left) Satellite orbit plotted together with the TEB search region limits and the RHESSI TGF observations (black asterisks). White regions are regions where the satellite has magnetically connection in one or two positions. Red regions are regions where the satellite has no magnetically connection, when it is inside the TEB search region. (Right) Satellite area distribution compared to the TGF distribution, compared to the time per latitude bin distribution. The integral over all latitudes is presented in the sub captions.

6.1.5 Pitch angle at different altitudes

The pitch angle and the bounce motion were introduced in Section 2.2.4 and 2.2.5. The first adiabatic invariant, Equation 2.11, tells that the pitch angle varies as a function of the magnetic field strength and we assume that the magnetic momentum μ is constant along the magnetic field line (see Section 2.2.5). Consider an electron, gyrating along a magnetic field line where the field strength decreases with altitude. The relation between the pitch angle and the magnetic field strength in two points, Equation 2.13, is used to compare the pitch angle at two different altitudes. From Equation 2.8, the magnetic field strength decreases as $\sim 1/r^3$, where r is the radius from the center in a dipole field. For Fermi we use F and S is for SAMPEX. The cross section area ratio A_S/A_F, of the cones, that corresponds to the pitch angles α_S and α_F, to a gyrating particle in two given altitudes, S and F, is given by the ratio:

$$\frac{A_S}{A_F} = \frac{r_S^2}{r_F^2} = \frac{sin^2\,\alpha_S}{sin^2\,\alpha_F} = \frac{(R_E + R_F)^3}{(R_E + R_S)^3} \sim 1.13, \tag{6.3}$$

where $R_E = 6371\,\text{km}$ is the Earth radius. The geometry is given in Figure 6.8. In this analysis, where $R_S = 300\,\text{km}$ and $R_F = 570\,\text{km}$, the ratio given in Equation 6.3 is ~ 1.13. This means that because Fermi's orbit is higher, where the bulk of the escaping particles has smaller pitch angle and the area of the cone is smaller, Fermi is less likely to see the TEB.

If this factor is multiplied with the factor of ~ 0.55, given in Equation 6.2, we get ~ 0.62. However, there is still one factor that has to be considered.

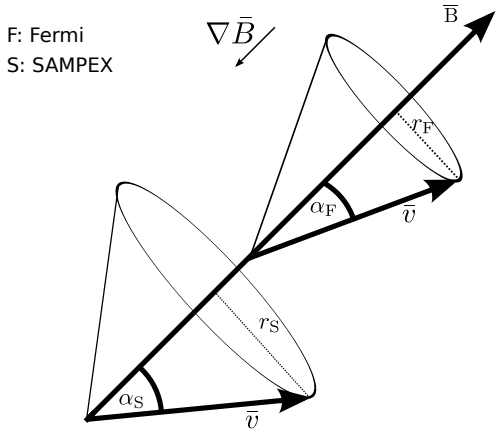

Figure 6.8: The pitch angle of an electron that gyrates along a magnetic field line in altitude S and F. The strength of the magnetic field decreases with altitude and the pitch angle decreases with decreasing magnetic field strength.

6.1.6 Instrument sensitivity

Until now, only parameters related to the orbit geometry and the geomagnetic field are taken into account. If two identical instruments were passing in two different orbits, this would be sufficient. However, Fermi's Bismuth Germanate detector (BGO) and HILT on SAMPEX do not have the same detection properties. The two BGO detectors on Fermi each has a geometric factor of $\sim$ 675 cm^2sr, that in total is $\sim$ 1 350 cm^2sr (see Appendix B.2). HILT on SAMPEX has a geometric factor of 60 cm^2sr (see Section 3.1.1 and Appendix B.1). If Fermi's BGO and HILT detect the same flux of gyrating electrons, Fermi should detect a $\sim$ 22.5 times stronger signal. In other words, if HILT detects 14 counts per 20 ms, Fermi's BGO should detect 315 counts per 20 ms.

According to the first three Fermi GBM TEBs presented in Table 2.2, Michael Briggs, member of the Fermi GBM team, has given us information about counts above 1 MeV (SAMPEX measures electrons $>$ 1 MeV) in the two Fermi BGOs [personal communication, March 27, 2015]. The counts are presented in Table 6.1. Most all of the other TEBs observed by Fermi are weaker than those presented. Consider that HILT observed a background count rate of 0.4 counts per 20 ms, the p-value of observing two or more counts is 0.09. Correspondingly for observing four or more counts, the p-value is 0.0008. These p-values are many orders of magnitude greater than 10^{-9}. Observing 9 or more counts, on the other hand, corresponds to a p-value of $5.04 \cdot 10^{-10}$, that would have been marked as interesting by the TEB search algorithm. 2, 4 and 9 counts in HILT are equivalent to respectively 48, 90 and 200 counts in the BGO detector (see Table 6.1).

Table 6.1: Counts above 1 MeV in Fermi BGO 1 and BGO 2, given by Michael Briggs [personal communication, March 27, 2015]. Most of the other Fermi detected TEBs are weaker than these three events. "Equivalent HILT" is the number of counts HILT would have detected if the same flux of particles passed the detector.

Id.	BGO 1 [counts]	BGO 2 [counts]	BGO 1 + BGO 2 [counts]	Equivalent HILT [counts]
080807.357	48	0	48	$\sim$2
090813.215	-	-	90	$\sim$4
091214.495	-	-	200	$\sim$9

From the middle of 2008 to the middle of 2014 (31 July), 15 TEBs have been detected by Fermi (see Section 2.5.4.1) and just one of these are, according to our calculations, detectable by HILT. The others, weaker ones, would not have been distinguishable from background radiation and instrument noise.

6.1.7 Expected TEB detection by SAMPEX

Now we have estimated all the various factors that define the different detection rates. The goal in this analysis is to get an idea of how many TEBs SAMPEX is expected to detect per year, using the Fermi detection rate of 2.5 TEBs per year as benchmark. Taking into account all the relevant factors, the detection rate is finally given by:

$$\text{Exp. TEB obs.} = \frac{1}{15} \cdot 2.5 \, \frac{\text{Fermi TEB}}{\text{Year}} \cdot 0.62 \, \frac{\text{SAMPEX TEB}}{\text{Fermi TEB}} = 0.10 \, \frac{\text{SAMPEX TEB}}{\text{Year}}, \tag{6.4}$$

where 1/15 is the ratio of TEBs that were bright enough in the BGO detector, to be observed by HILT. Consequently, HILT is able to observe $\sim$ 4% (0.1/2.5) of what Fermi observes. The probability of detecting one or more events, in a year of data, is derived by Equation A.6 in Appendix A about the Poisson statistics $[P(X = 0) = P_0(t)]$:

$$P(X \geq 1) = 1 - P(X = 0) = 1 - e^{-0.10} = 0.098. \tag{6.5}$$

The probability of detecting one or more TEBs in a year for SAMPEX, according to this analysis when 0.1 TEB is expected, is $\sim$ 9.8%. This is a relatively low probability of success, compared to $\sim$ 91.8% for Fermi.

6.2 Associated lightning activity ratio

The null hypothesis indicates that $\sim$ 10.4% of all arbitrary SAMPEX moments do have associated lightning activity (see Section 5.3.3). If the associated lightning activity ratio correlated to more than 300 TEB candidates, is significant greater than for the null hypothesis, this may suggest that there are a correlation between the measured signals and thunderstorm activity [*Connaughton et al.*, 2010].

According to Table 5.3, where the associated lightning activity ratios are presented, the binomial probability P(X $\geq$ x) (see Equation 4.9) for each method and search are estimated, as described in Section 4.6. These probability values are presented in Table 6.2. The probability of success used, $p = 0.1040$, is from the associated lightning activity ratio for the null hypothesis data set (see Section 5.3.3). For a binomial hypothesis test we do have a significant increase in the lightning activity ratio if the probability value is less than 0.05 (95% level of significance), as mentioned in Section 4.6.

For method 1.1-1.3, the probability values do not indicate that there is an increase in the associated lightning ratio, but for method 2.1 and 2.2, it is a significant increase. Method 2.1 and 2.2, search A, may have enough included candidates to claim that

there are more associated lightning activity. The number of included candidates are thought to be too low for the other methods and searches where $P < 0.05$. What we can conclude, is that for all the 361 TEB candidates together (method 3.1), there are, according to the statistics ($P \sim 0.49$), no more associated lightning activity correlated to the TEB candidates than for the null candidates. In other words, we cannot reject H_0 in Equation 4.8.

Table 6.2: The binomial probability $P(X \geq x)$ (see Equation 4.9), for the lightning activity ratio are presented for each method and search. n is the total number of TEB candidates (Table 5.1), x is the number of TEB candidates with associated lightning activity (Table 5.3). The probability of success $p = 0.1040$. The binomial test indicates an increase in the associated lightning activity ratio for TEB candidates if $P < 0.05$ (95% confidence).

Method	Search A	Search B	Search C	Common	Common
1.1	0.2976	0.4019	0.3401	0.3452	0.0096
1.2	0.1314	0.1543	0.4809		
1.3	0.1349	0.1015	0.2567		
2.1	0.0012	0.0173	0.0337	0.0836	
2.2	0.0008	0.1549	0.1090		
3.1	0.0667	0.2805	0.4939	-	-

6.3 No lightning, no TEBs

Connaughton et al. [2010] pointed out that based on the efficiency of the WWLLN (see Section 3.2), a correlation between a TGF (in our case a TEB) and an individual sferic in many cases would not be found. This means that a satellite may observe a TEB without having an exact WWLLN match, but WWLLN should detect some other sferics from the same thunderstorm system. The probability for WWLLN to detect an actual lightning stroke is rather low, but the probability for detecting at least one stroke in a thunderstorm should be much higher. If there are no lightning activity at all around any foot point in a time scale in range of minutes, it is reasonable to think that this has to be something else than TEBs. This applies to $\sim 89.5\%$ of the ~ 361 candidates. Typical duration and size of thunderstorms and systems of thunderstorms were discussed in Section 2.4.

Let us consider that 89.5% of all our candidates do not have anything to do with lightning and they have to be something else than TEBs. Then we have 10.5% candidates left. If we now consider that the same fraction (89.5%) of false TEB detections also applies to the candidates that have associated lightning activity but no matches, we are left with 0.8%, which is three candidates. This is a number consistent with the one candidate we found with WWLLN match (< 1 s

and $< 250\,\mathrm{km}$) and the observation rate for other satellites (see Section 2.5.4.1). It is important to notice that this is just a qualitative indicator that the number of observed TEBs are low. This is schematically presented in Figure 6.9.

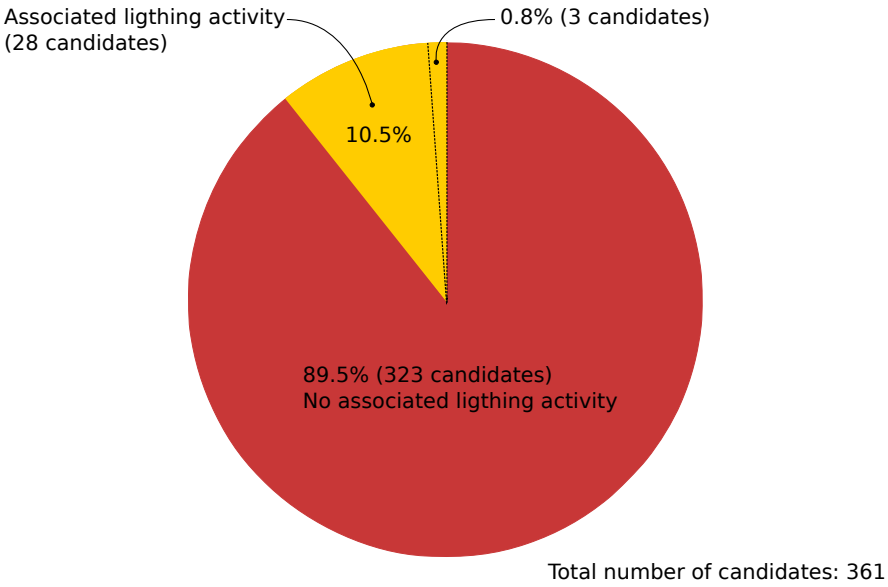

Figure 6.9: The circle represents all the TEB candidates. (Red) 89.5% of the candidates do not have associated lightning activity and probably have to be something else than TEBs. (Yellow) 10.5% of all candidates do have associated lightning activity. If we consider that 89.5% of those candidates do not have any correlation to lightning activity and have to be something else than TEBs, three candidates are left. Notice, this is just a qualitative indicator that a small number of TEBs are expected.

6.4 Other phenomena

From our investigation, it is not realistic that all SAMPEX TEB candidates are real TEBs. The estimation (see Section 6.1) of what SAMPEX should be able to observe, compared to what Fermi observes, shows that less than one TEB should be detected per year. Now, we will discuss what other phenomena that could cause such bright signals in the HILT data. Much of the background observed are thought to be cosmic rays hitting the detector or instrumental noise. Bright signals are thought to be cosmic ray showers or digital glitches in the instrument.

6.4.1 Cosmic ray showers

Cosmic rays are the most energetic particles ever observed [*Carlson*, 2009]. According to *Briggs et al.* [2010], it is known that cosmic rays could mimic TGF signals. Cosmic rays could be photons or nucleus with energies above 100 TeV, that are able to make showers of secondaries when interacting with the atmosphere or hitting the detector body. A wide range energy spectrum distributed as $\mathrm{dN/dE} \propto 1/\mathrm{E}^3$ holds for energies from 10^{10} eV to 10^{19} eV, with a flux hitting the Earth's atmosphere in range of one particle per square meter per year ($\sim 1\,\mathrm{m}^{-2} \cdot \mathrm{year}^{-1}$) [*Carlson*, 2009]. A more thorough review of cosmic rays and showers is beyond the scope of this thesis.

Cosmic ray events were tried to be removed in the Fermi TGF search, either by their characteristics in the GBM data or because of high energy deposition in Fermi's Large Area Telescope (LAT). *Grefenstette et al.* [2009] and *Gjesteland et al.* [2012] removed events shorter than 100 μs to avoid cosmic ray shower events. The problem for SAMPEX is that the time resolution of 20 ms restricts the possibility to remove events that is too short to be a TEB.

According to Table 4 in *Briggs et al.* [2013], the LAT-identified cosmic ray shower fraction for the total Fermi search is 26%. *Briggs et al.* [2013] and *Østgaard et al.* [2012] both estimated that Fermi would see about 900 ± 450 TGFs per year, if Fermi downloaded all data. If the same fraction of cosmic ray showers applies to that (26%), cosmic showers and TGFs together would be ~ 1216 triggered signals. Then Fermi would see ~ 316 cosmic ray showers per year. If SAMPEX would be as sensitive to cosmic ray showers as Fermi, then all of our candidates could well be cosmic ray showers.

In Figure 5.3, all the TEB candidates found by method 3.1 search C are plotted per longitude/latitude bin. In Figure 6.10, the same SAMPEX positions are plotted, but now the number of candidates per longitude/latitude bin are weighted by the area of the bin inside the TEB search region (see Section 4.2). The areas per bin are sub areas of a sphere with radius ($\mathrm{R_E} + 45\,\mathrm{km}$), given by:

$$A = \int_{\phi_1}^{\phi_2} \int_{\theta_1}^{\theta_2} (R_\mathrm{E} + 45\,\mathrm{km})^2 \, sin\,\theta \, \mathrm{d}\theta \, \mathrm{d}\phi = \frac{\pi}{180^\circ} (\theta_2 - \theta_1)(cos\,\phi_1 - cos\,\phi_2)(\mathrm{R_E} + 45\,\mathrm{km})^2, \tag{6.6}$$

where ϕ_1 and ϕ_2 are the co-latitude limits in degrees ($\phi_1 < \phi_2$), θ_1 and θ_2 are the longitude limits of the sub area ($\theta_1 < \theta_2$). It can be seen in Figure 6.10 that the TEB candidates distribution per longitude/latitude bin per area, is relatively uniform. If our candidates was real TEBs we would expected a distribution more like the TGF distribution given in Figure 6.5 or the TEB distribution given in Figure 2.29, where the numbers of observations are correlated to regions with high lightning activity. Our relatively uniform TEB candidate distribution, indicates that SAMPEX has

observed many events of uniform distributed phenomena, thought to be correlated to cosmic rays. This together with the expected SAMPEX TEB detection (see Section 6.1.7), indicate that most likely all of the $\sim$ 50 TEB candidates found by *Carlson et al.* [2009] (see Section 2.5.4.1), also may be something else than TEBs ($\sim$ one TEB expected in 8 years of SAMPEX data).

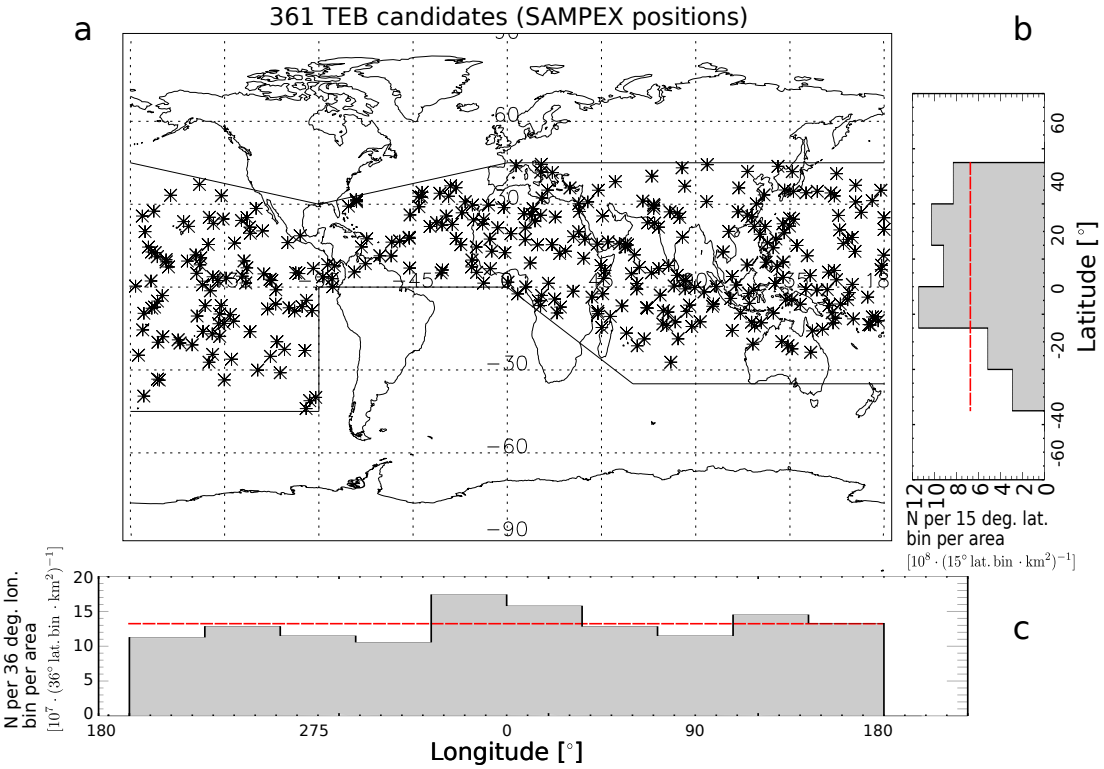

Figure 6.10: TEB candidate distribution. (a) All the TEB candidate SAMPEX positions found by method 3.1 search C plotted as black asterisks together with the limits of the TEB search region (black solid lines). (b) The number of TEB candidates per 15° latitude bin per area inside the TEB search region. (c) The number of TEB candidates per 36° longitude bin per area inside the TEB search region. The red dashed lines in plot b and c are the mean value of all bins.

6.4.2 Electronic glitches

It is thought to be a chance that digital glitches are able to generate significant signals in the HILT data set. This instrument technical phenomena is not related to something natural phenomena, but rather errors in the electronics. A glitch is a short-lived fault in a system and could be caused by induced current from other devices at the satellite. It is difficult to identify such signals. It has been tried

to find information in SAMPEX housekeeping data, but without any results so far [Mark Looper, private communication, 18 May, 2015].

6.5 Reliability of the WWLLN match

The WWLLN matched TEB candidate, observed on the 28 May 2012 - 07:43:25.52 UTC, is presented in Section 5.3.1.1. This TEB candidate has two sferics that fulfill the WWLLN match criteria and both of them could have generated a TEB. The reliability of this candidate will be more discussed in this section. At least three factors will be discussed for the WWLLN matched TEB candidate. (1) Is it realistic that a WWLLN detected sferic, 125 km away from the foot point, could cause the signal measured by HILT? (2) Is the time between the WWLLN detection and the HILT signal realistic according to clock drift and other uncertainties? (3) What is the probability of chance occurrence of one or more discharges, ±1 second, within a radius of 125 km?

The geometry of a WWLLN detection at $\sim$ 15 km altitude, $\sim$ 125 km horizontal displaced from a foot point in $\sim$ 45 km altitude, a cone of possible TEB directions and magnetic field lines with an inclination of $\sim 27°$, are presented in Figure 6.11. The field line inclination is estimated by a right-angled triangle where the foot point at 0 km is $\sim$ 89 km horizontal displaced from the foot point in 45 km altitude. This was the case for the WWLLN matched TEB candidate. The foot point found by IGRF has an uncertainty that depends on a lot of different factors, in this thesis it is set to ±40 km. It can be seen in Figure 6.11, that due to relatively large uncertainties in both space and time, the beam of gyrating electrons could propagate along magnetic field lines that the SAMPEX satellite passed at this moment.

According to the GLD360 match with the Fermi 100515.316 TEB, found by *Cohen et al.* [2010] (see Section 2.5.4.1), it was pointed that the horizontal displacement of $\sim$ 75 km, between the Fermi foot point and the GLD360 detection, would be near the edge of a predicted TEB [*Carlson et al.*, 2009; *Dwyer et al.*, 2008]. It is important to notice that *Cohen et al.* [2010] considered a much smaller time differences ($\Delta t \sim 0.25$ ms) than for our project ($\Delta t \sim 1$ s), and consequently it is easier to ascertain that the GLD360 actually was a TEB - sferic match.

The time criterion for a WWLLN match was presented in Equation 4.7. The time t_1, is 27 805.52 sec of day (sod), t_2 is 27 805.58 sod and $\Delta t = 1$ s. From this, the outer limits of the criterion interval are: $t_{\mathrm{WWLLN}} + s/c \in$ [27 804.52 sod, 27 806.58 sod]. The speed-of-light propagation delay is 6.57 ms, due to the 1 970 km distance along the magnetic field line, between the foot point and the SAMPEX position. $t_{\mathrm{WWLLN}} + s/c = 27\,805.662697\,\mathrm{sod} + 6.57 \cdot 10^{-3}\,\mathrm{s} \approx 27\,805.66\,\mathrm{sod}$. The time criterion for a WWLLN match is fulfilled for this TEB candidate, since 27 805.66 sod is inside

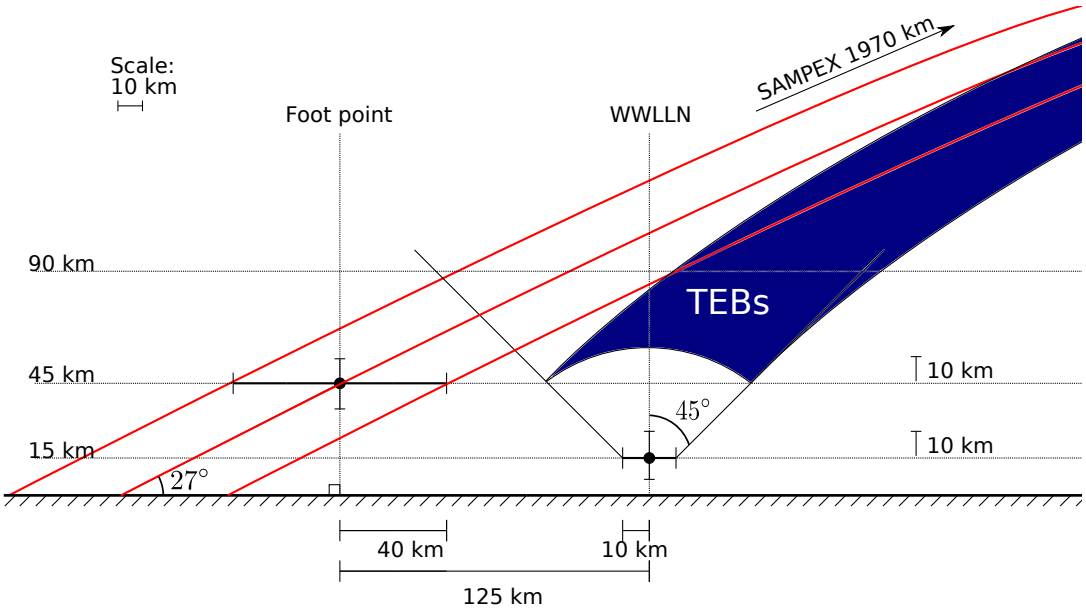

Figure 6.11: Geometry of a foot point in 45 km altitude and a lightning stroke 125 km horizontal displaced from the foot point, in 15 km altitude. This is just a qualitative argument that the WWLLN detected sferic could have generated a TEB, detected by SAMPEX.

the time interval given above. This is also fulfilled for the other detected sferic. The time uncertainty for WWLLN, $\Delta t \sim \pm 30\,\mu s$ (see Section 3.4.3), is in this context negligible, due to the large uncertainty in the SAMPEX data.

The WWLLN detection rate of sferics in the southern foot point is estimated by using the data set of 124 sferics detected within a radius of 500 km, ±10 minutes (see Section 5.3.1.1). The WWLLN detection rate is estimated to be $1.32 \cdot 10^{-7}\,\text{sferic} \cdot \text{km}^{-2} \cdot \text{s}^{-1}$ or $0.013\,\text{sferic} \cdot (125\,km)^{-2} \cdot (\pi \cdot 2\,\text{sec})^{-1}$, used as an expected value in this case. The probability of chance occurrence of detecting one or more discharges within ±1 s, 125 km of the southern foot point, is estimated to be ~ 0.013, by using Equation 6.5. In comparison, *Cohen et al.* [2010] has a probability of chance occurrence like $\sim$ 0.001 for his GLD360 match with the Fermi 100515.316 TEB. This probability is much smaller due to $\Delta t \sim 5$ ms and 75 km offset.

Let us consider that SAMPEX detects ~ 300 cosmic showers per year. This number is consistent with both the number of cosmic showers detected by Fermi per year (see Section 6.4.1) and the number of significant TEB candidates detected by HILT in 2012 (see Table 5.1). The probability of detecting a cosmic shower in an arbitrary 2 seconds long time interval, is $\sim 1.9 \cdot 10^{-5}$. A lightning stroke and a cosmic shower are thought to be two independent occurrences. The probability of detecting one or more lightning strokes with WWLLN and a cosmic shower by HILT in the same

moment, is the product of the probabilities separately, that is $\sim 2.5 \cdot 10^{-7}$. This is thought to be a relatively low probability of occurrence, but taking into account that one year is $\sim 10^7$ s, this could have occurred during 2012.

From the arguments proclaimed above, we can say that it is a probability that this could be a TEB observed by SAMPEX, but on the other hand, due to large uncertainties, it is not evidence to establish that this is a TEB. What we can say, is that it is a relatively low probability that both a cosmic shower and a sferic detection occurred at the same time and that it is $\sim 9.8\%$ probability for detecting one or more TEB per year.

Chapter 7

Conclusions

In this thesis work we have found 361 significant TEB candidates in the SAMPEX HILT data for 2012. TEB candidates are short pulses, that due to an assumed Poisson distributed background radiation, seem to be significant ($P(N \geq n|b_{obs}) < 10^{-9}$) above the fluctuations in the background b_{obs}. This is a relatively large number of candidates, when just one false positive is expected per year. The statistics just tells us that these candidates are probably something else than background, but nothing about what they actually are.

It has been performed a modeling analysis of how many TEBs HILT should be able to detect, compared to the number of TEBs that the Fermi's BGO has detected. Different orbits and instrument properties affect the number of expected TEB observations of the two satellites per year. Due to orbit geometry, SAMPEX should be able to observe 62% of what Fermi observes, e.g. ~ 1.55 TEBs per year. Fermi's BGO has a geometric factor that is ~ 22.5 times greater than for SAMPEX HILT, with the consequence that most of the Fermi TEBs would not have been bright enough for HILT to be observed. From this, SAMPEX should be able to detect 0.1 TEB per year, or 1 TEB per ten years.

$\sim 10.5\%$ of all the candidates have associated WWLLN detected lightning activity, in at least one magnetic foot point. In other words, 89.5% of the TEB candidates have no associated lightning activity. According to *Connaughton et al.* [2010], due to the WWLLN detection efficiency, the probability of having a thunderstorm where WWLLN does not detect any sferics at all, should be rather low. We assume therefore that a TEB should have at least associated lightning activity in at least one foot point.

A null hypothesis consisting of more than $3 \cdot 10^5$ arbitrary SAMPEX moments were searched for lightning in the same way as for the TEB candidates. The results of this null hypothesis show that $\sim 10.4\%$ of the null candidates do have associated lightning activity, which indicates by binomial hypothesis test that our TEB

candidates are not more correlated to thunderstorms, than the null candidates.

Consequently, a lot of arguments indicate that most likely all of our candidates are something else than TEBs. Such signals could be cosmic ray showers and/or digital glitches. It is known that cosmic showers could mimic TGF signals [*Briggs et al.*, 2010]. Calculations show that according to Fermi, SAMPEX could be able to detect $\sim$ 300 cosmic showers per year, but it is difficult to predict without information about energies in our HILT data.

Based on Fermi results, SAMPEX has the probability of 9.8% to observe one or more TEB per year. This is a relatively low probability of success, compared to Fermi.

One candidate, observed on the 28th of May 2012 at 07:43:25.52 UTC, has two WWLLN detected sferics, $\sim$ 125 km and $\sim$ 128 km from the southern foot point, which fulfill the WWLLN match time criterion (see Equation 4.7). This is the only candidate, of all observed, that has sferics within 250 km from the foot point that fulfill the time criterion.

We can not, from this analysis, establish that we have found a SAMPEX TEB in 2012. What we can establish is that almost all our more than 300 TEB candidates were something else than TEBs and that we have one possible TEB event.

Chapter 8

Future work

In this thesis we have found a lot of signals measured by HILT that could be TEBs (see Chapter 5). We have concluded that most of our TEB candidates are most likely something else than real TEBs. Suggestions of what other phenomena that could generate such signals have been presented (see Chapter 6 and 7). In this chapter we will suggest a method and elements that could be included in a future work, looking for TEBs in SAMPEX data.

1. Our search algorithm starts by a statistical search for signals significant above the background count rate in HILT data. We trace the magnetic field lines and search for lightning activity in the foot points by using WWLLN data (see Chapter 4).

   This method could be performed in the opposite way, by starting with the WWLLN data (schematically presented in Figure 8.1). A WWLLN detected sferic has both its location and time. The next step will be to trace the magnetic field line that has its foot point at the sferic location, and find out where SAMPEX was located in this moment. If SAMPEX passed near by the actual magnetic field line, the sferic has to be marked as interesting. By estimating the distance between the foot point and the satellite, along the field line, the speed-of-light propagation delay time could be estimated. If HILT detected counts above background in the right moment, this could be a TEB event. This search could be done as in the TEB search algorithm, by use of Poisson statistics (see Section 4.1).

   According to Table 6.1, most of the Fermi detected TEBs would have been too weak to be observed by our method (p-value $< 10^{-9}$). By this method, on the other hand, the p-value could be increased, such that weaker signals could be flagged as candidates. This could be done because we now have a combination of independent measurements (WWLLN & SAMPEX) for all the candidates. This would increase the probability of detecting one or more TEBs per year.

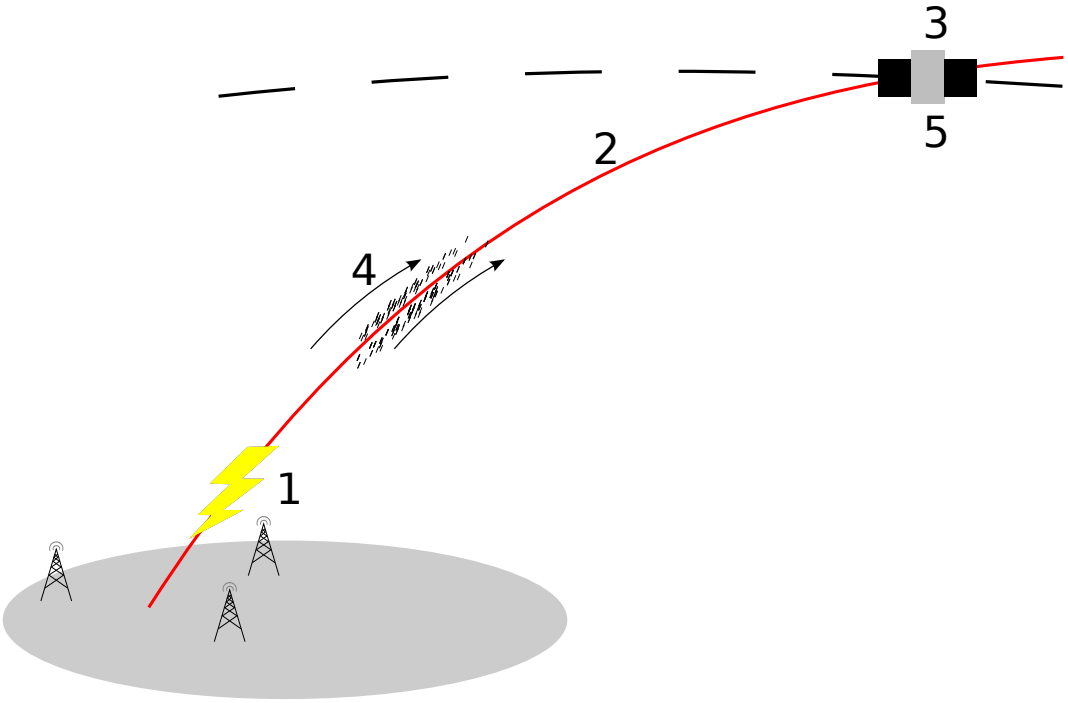

Figure 8.1: An alternative method for TEB search. (1) Start with a WWLLN detected sferic. (2) Trace the magnetic field line. (3) See if SAMPEX was located near by the magnetic field line. (4) Estimate the distance and the speed-of-light propagation delay time for the electrons between the foot point and SAMPEX. (5) Search for signals in HILT data.

2. In our modeling analysis we have estimated that SAMPEX is expected to observe $\sim$ 0.1 TEB per year (see Section 6.1). In this thesis we only had access to WWLLN data for 2012. Our group bought all the WWLLN data in May 2015. In a future work, more data could therefore be included to increase the probability of TEB detection. Including ten years of HILT and WWLLN data corresponds to a probability of observing one or more TEBs equal to $\sim$ 0.63 (Equation 6.5, 1 TEB per 10 years is expected). This could probably be done for earlier data, where you could have support from other instruments at SAMPEX to sort out other phenomena. The time accuracy due to drift in the space clocks will still be the same ($\Delta t \sim 1\,\mathrm{s}$).

3. If it is possible to find out more about the drift in the space clocks, maybe it could be compensated for. This could probably decrease the time uncertainties in the HILT data. Then it would be easier to proclaim a simultaneity between an electron beam's arrival at SAMPEX and a measured signal by HILT.

Appendix A

Poisson distribution

In this section the Poisson distribution is derived. This Appendix is based on lecture notes by Bjørn Davidsen at the University of Tromsø.

The Poisson distribution function gives the probability P_n, for a given event to occur $0, 1, 2, 3, ..., n, ...$ times in a given time interval t. When using Poisson distribution, some conditions have to be satisfied:

1. The probability P_n, for a given event to occur in a small time interval Δt, has to be proportional to the length of the interval: $P_1(\Delta t) = \lambda \cdot \Delta t$, where λ is just a constant
2. The probability P_n, for more than one event to occur in a small time interval Δt can be neglected, if we let $\Delta t \to 0$
3. The compliment probability, that none events occur in a small time interval Δt, is given by $P_0(\Delta t) = 1 - P_1(\Delta t)$
4. The probability for one event to occur, is not dependent to the probability for another event that happened earlier

P_0 is the probability that none events occur in an interval t. If the 4th condition is satisfied, it will be given by:

$$\begin{aligned} P_0(t + \Delta t) &= P_0(t) \cdot P_0(\Delta t) \\ &= P_0(t) \cdot (1 - \lambda \cdot \Delta t) \\ &= P_0(t) - \lambda \cdot P_0(t) \cdot \Delta t \end{aligned} \tag{A.1}$$

$$\Updownarrow$$

$$\frac{P_0(t + \Delta t) - P_0(t)}{\Delta t} = -\lambda \cdot P_0(t) \tag{A.2}$$

Let $\Delta t \to 0$:

$$\Updownarrow$$

$$\lim_{\Delta t \to 0} \frac{P_0(t+\Delta t) - P_0(t)}{\Delta t} = \lim_{\Delta t \to 0} -\lambda \cdot P_0(t) \tag{A.3}$$

The limit to the left is the same as the definition of the derivative $\frac{\mathrm{d}P_0(t)}{\mathrm{d}t}$, and this can be written as a separable differential equation:

$$\frac{\mathrm{d}P_0(t)}{\mathrm{d}t} = -\lambda \cdot P_0(t) \tag{A.4}$$

$$\Updownarrow$$

$$P_0(t) = C_0 e^{-\lambda t} \tag{A.5}$$

Since $P_0(t) \to 1$ when $t \to 0$, $C_0 = 1$. P_0 can be written as:

$$\underline{P_0(t) = e^{-\lambda t}} \tag{A.6}$$

In the same way, it can be shown that $P_1 = \lambda t \cdot e^{-\lambda t}$. Then use that:

$$\begin{aligned} P_1(t+\Delta t) &= P_1(t) \cdot P_0(\Delta t) + P_0(t) \cdot P_1(\Delta t) \\ &= P_1(t) \cdot (1 - \lambda \cdot \Delta t) + e^{-\lambda t} \cdot (\lambda \cdot \Delta t) \\ &= P_1(t) - \lambda \cdot P_1(t) \cdot \Delta t + \lambda \cdot e^{-\lambda t} \cdot \Delta t \end{aligned} \tag{A.7}$$

$$\Updownarrow$$

$$\lim_{\Delta t \to 0} \frac{P_1(t+\Delta t) - P_1(t)}{\Delta t} + \lim_{\Delta t \to 0} \lambda \cdot P_1(t) = \lim_{\Delta t \to 0} \lambda \cdot e^{-\lambda t} \tag{A.8}$$

$$\Updownarrow$$

This is a linear differential equation:

$$\frac{\mathrm{d}P_1(t)}{\mathrm{d}t} + \lambda \cdot P_1(t) = \lambda \cdot e^{-\lambda t} \tag{A.9}$$

With the solution:

$$P_1(t) = e^{-\lambda t}(\lambda t + C_1) \tag{A.10}$$

Since $P_1(t) \to 0$ when $t \to 0$, $C_1 = 0$. P_1 can be written as:

$$\underline{P_1(t) = \lambda t \cdot e^{-\lambda t}} \tag{A.11}$$

In the same way, you can find P_2, P_3 etc. Then you will find:

$$\underline{P_2(t) = \frac{(\lambda t)^2}{2} \cdot e^{-\lambda t}} \quad \text{and} \quad \underline{P_3(t) = \frac{(\lambda t)^3}{2 \cdot 3} \cdot e^{-\lambda t}} \tag{A.12}$$

If we assume that:

$$P_n(t) = \frac{(\lambda t)^n}{n!} \cdot e^{-\lambda t} \quad \text{where} \quad n = 0, 1, 2, 3, ... \tag{A.13}$$

Then it is possible to do a proof by induction of this expression, where $n = k$:

$$\begin{aligned} P_{k+1}(t + \Delta t) &= P_{k+1}(t) \cdot P_0(\Delta t) + P_k(t) \cdot P_1(\Delta t) \\ &= P_{k+1}(t) \cdot (1 - \lambda \cdot \Delta t) + \frac{(\lambda t)^k}{k!} \cdot e^{-\lambda t} \cdot (\lambda \cdot \Delta t) \\ &= P_{k+1}(t) - \lambda \cdot p_{k+1}(t) \cdot \Delta t + \frac{\lambda^{k+1} t^k}{k!} \cdot e^{-\lambda t} \cdot \Delta t \end{aligned} \tag{A.14}$$

This expression may be rewritten as:

$$\lim_{\Delta t \to 0} \frac{P_{k+1}(t + \Delta t) - P_{k+1}(t)}{\Delta t} + \lim_{\Delta t \to 0} \lambda \cdot P_{k+1}(t) = \lim_{\Delta t \to 0} \frac{\lambda^{k+1} t^k}{k!} \cdot e^{-\lambda t} \tag{A.15}$$

The first term is known as the time derivative and we can rewrite this as a linear differential equation:

$$\frac{\mathrm{d}P_{k+1}(t)}{\mathrm{dt}} + \lambda \cdot P_{k+1}(t) = \frac{\lambda^{k+1} t^k}{k!} \cdot e^{-\lambda} t \tag{A.16}$$

With a solution:

$$\begin{aligned} P_{k+1}(t) &= e^{-\lambda t} \left(\int \frac{\lambda^{k+1} t^k}{k!} \cdot e^{-\lambda t} \cdot e^{\lambda t} dt + C_{k+1} \right) \\ &= e^{-\lambda t} \left(\frac{(\lambda t)^{k+1}}{k!(k+1)} + C_{k+1} \right) \\ &= e^{-\lambda t} \left(\frac{(\lambda t)^{k+1}}{(k+1)!} + C_{k+1} \right) \end{aligned} \tag{A.17}$$

Since $P_{k+1} \to 0$ when $t \to 0$, $C_{k+1} = 0$. $P_{k+1}(t)$ is given by:

$$P_{k+1}(t) = \frac{(\lambda t)^{k+1}}{(k+1)!} \cdot e^{-\lambda t} \tag{A.18}$$

This is the same as if we substitute $n = k+1$. Instead of writing $P_n(t)$, it is possible to write P(X = n). Then we get the expression:

$$P(X = n) = \frac{(\lambda t)^n}{n!} \cdot e^{-\lambda t} \quad \text{where} \quad n = 0, 1, 2, 3, ... \tag{A.19}$$

This is the Poisson distribution function, with expected value $\mu = \mathrm{E(X)} = \lambda t$, variance $\mathrm{Var(X)} = \lambda t$ and the standard deviation $\mathrm{SD(X)}{=}\sigma = \sqrt{\mathrm{VAR(X)}} = \sqrt{\lambda t}$. The Poisson Cumulative Distribution Function (CDF), $P(X \leq n)$ is given by:

$$P(X \leq n) = \sum_{i=0}^{n} \frac{(\lambda t)^i}{i!} \cdot e^{-\lambda t}, \quad \text{where} \quad n = 0, 1, 2, 3, ... \tag{A.20}$$

In the search for TEBs we estimate the expected value μ with the average count of a number of bins before and after the actual bin(s). The p-value is evaluated from Equation A.20 and is defined as:

$$\begin{aligned} P(X \geq n) &= 1 - P(X \leq n-1) \\ &= 1 - \sum_{i=0}^{n-1} \frac{\mu^i e^{-\mu}}{i!} \cdot, \quad \text{where} \quad n = 0, 1, 2, 3, ... \end{aligned} \tag{A.21}$$

Appendix B

Calculation of geometric factor

The calculations of geometric factors, of HILT and Fermi's BGO, are done with help from professor emeritus Johan Stadsnes.

B.1 SAMPEX HILT

The geometric factor of the HILT instrument on SAMPEX. The parameters used in this calculation are obtained from *Klecker et al.* [1993].

Geometric factor : $G = \Omega \cdot A$

Sensitive SSD area: $159\,\mathrm{cm}^2$

View angle: $68° \times 68°$ (full angle)

Radius: $R = \sqrt{(11.7\,\mathrm{cm})^2 + (3.8\,\mathrm{cm})^2}$

Rough estimate of solid angle. The geometry is described in Figure B.1.

$$\Omega \approx \frac{(7.6\,\mathrm{cm})^2}{(11.7\,\mathrm{cm})^2 + (3.8\,\mathrm{cm})^2} \approx 0.38\,\mathrm{sr} \tag{B.1}$$

Rough estimate of geometric factor:

$$G = \Omega \cdot A = 0.38\,\mathrm{sr} \cdot 159\,\mathrm{cm}^2 = 60.42\,\mathrm{cm}^2\mathrm{sr} \approx 60\,\mathrm{cm}^2\mathrm{sr} \tag{B.2}$$

Our result is in accordance with *Klecker et al.* [1993], the geometric factor of the HILT instrument is $60\,\mathrm{cm}^2\mathrm{sr}$.

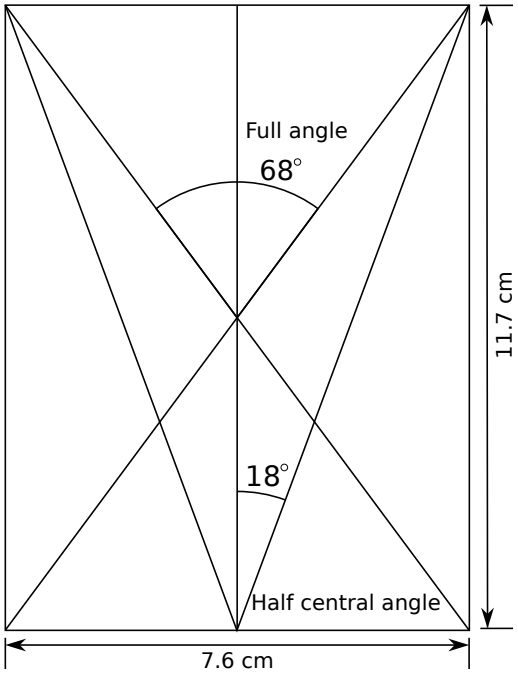

Figure B.1: The geometry of HILT used in the estimate of the geometric factor.

B.2 Fermi's BGO

The two Fermi's BGO detectors have a cylindrical shape, as can be seen in Figure B.2b. Calculation of the BGO geometric factor for X-rays per detector is done by (see Figure B.2a):

$$G_{\text{eff}} = 2\int_0^{90^\circ} A_{\text{eff}}(\phi)\,\mathrm{d}\Omega(\phi) \quad \text{where} \quad \mathrm{d}\Omega = \pi\, cos\,\phi\,\mathrm{d}\phi, \tag{B.3}$$

where A_{eff} is the effective area given in Figure B.3 and $\mathrm{d}\Omega$ is the unit angle. It is assumed that the radiation is isotropic distributed over the half sphere, $\phi\,\epsilon\,[-90^\circ, 90^\circ]$ (see Figure B.2a). $\mathrm{d}\,\Omega$ is for a half sphere with radius $R = 1$. For the 279 keV simulated measured values of A_{eff}, we got a geometric factor of $\sim 675\,\text{cm}^2\text{sr}$ per detector, and correspondingly $\sim 600\,\text{cm}^2\text{sr}$ for the 898 keV simulated values of A_{eff} (see Figure B.3). These measurements are for photons. For the electrons, a fraction will be back scattered and the radiation will not be totally isotropic for large angles. This is because of shielding due to the multiplication tubes in both ends of the cylinder. The geometric factor should therefore be a bit smaller for electrons, but $675\,\text{cm}^2\text{sr}$ per BGO is used in this thesis.

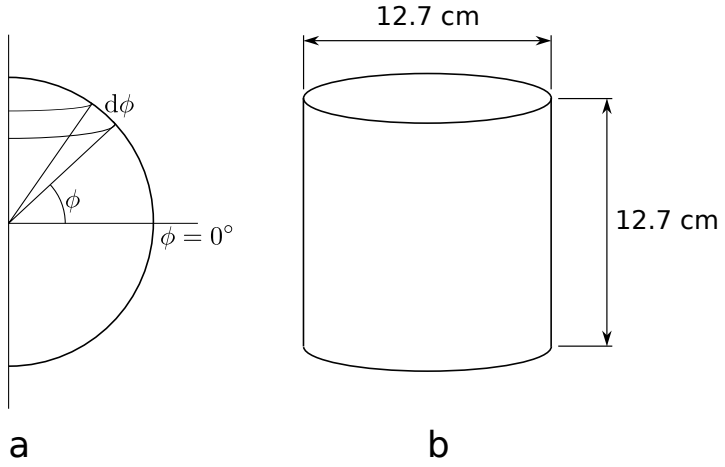

Figure B.2: a: Assume that the radiation is isotropic distributed over the half sphere, $\phi\,\epsilon\,[-90°, 90°]$ b: The geometry of Fermi's BGO, used in the estimate of the geometric factor.

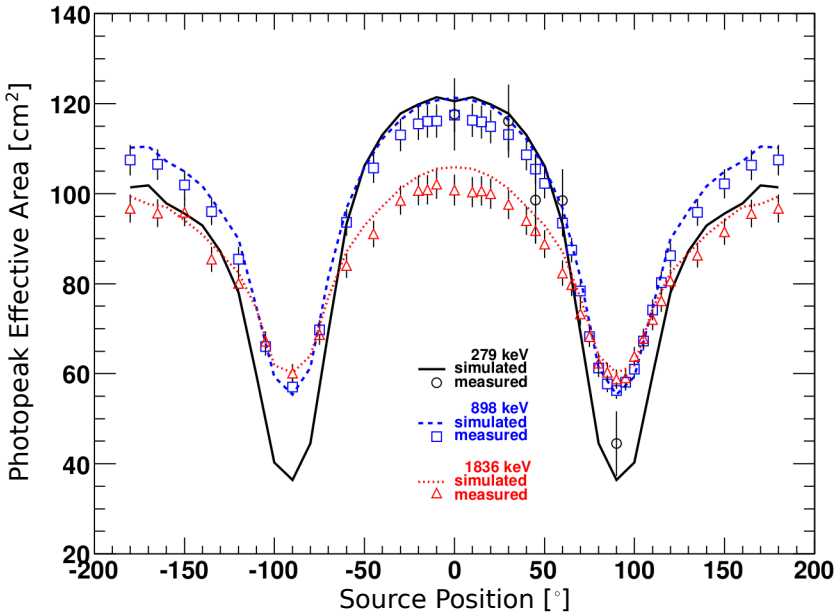

Figure B.3: Fermi's BGO effective area A_{eff}. Source Position is the ϕ-angle given in Figure B.2. Adapted from *Meegan et al.* [2009].

Bibliography

Abarca, S. F., K. L. Corbosiero, and T. J. Galarneau (2010), An evaluation of the Worldwide Lightning Location Network (WWLLN) using the National Lightning Detection Network (NLDN) as ground truth, *Journal of Geophysical Research*, *115*, D18206, doi:10.1029/2009JD013411.

Anderson, C. D. (1933), The Positive Electron, *Physical review*, *43*(6), 491–498, doi:http://dx.doi.org/10.1103/PhysRev.43.491.

Babich, L. P., E. N. Donskoy, and I. Kutsyk (2005), The feedback mechanism of runaway air breakdown, *Geophysical Research Letters*, *32*(9), L09809, doi: 10.1029/2004GL021744.

Baker, D., G. Mason, O. Figueroa, G. Colon, J. Watzin, and R. Aleman (1993), An overview of the Solar Anomalous, and Magnetospheric Particle Explorer (SAMPEX) mission, *IEEE Transactions on Geoscience and Remote Sensing*, *31*(3), doi:10.1109/36.225519.

Baumjohann, W., and R. A. Treumann (1997), *Basic Space Plasma Physics*, Imperial College Press, London.

Bazelyan, Y. P., and E. M. Raizer (2000), The streamer-leader process in a long spark, in *Lightning Physics and Lightning Protection*, chap. 2, pp. 27–89, Taylor & Francis, doi:10.1201/9781420034011.ch2.

Berger, K. (1978), Blitzstrom-Parameter von Aufwärtsblitzen, *Bull.Schweiz.Elektrotech.*, (69), 353–360.

Berger, M. J., J. H. Hubbell, S. M. Seltzer, J. Chang, J. S. Coursey, R. Sukumar, D. S. Zucker, and K. Olsen (1998), XCOM: Photon Cross Sections Database, *NIST Standard Reference Database 8 (XGAM).*

Bethe, H., and J. Ashkin (1953), Passage of radiation through matter, in *Experimental Nuclear Physics*, edited by E. Segre, vol. 2 ed., chap. 2, pp. 166–358, New York - London.

Briggs, M. S., et al. (2010), First results on terrestrial gamma ray flashes from the

Fermi Gamma-ray Burst Monitor, *Journal of Geophysical Research*, *115*, A07323, doi:10.1029/2009JA015242.

Briggs, M. S., et al. (2011), Electron-positron beams from terrestrial lightning observed with Fermi GBM, *Geophysical Research Letters*, *38*, L02808, doi: 10.1029/2010GL046259.

Briggs, M. S., et al. (2013), Terrestrial gamma-ray flashes in the Fermi era: Improvedobservations and analysis methods, *Journal of Geophysical Research: Space Physics*, *118*(6), 3805–3830, doi:10.1002/jgra.50205.

Burkholder, B. S., M. L. Hutchins, M. P. McCarthy, R. F. Pfaff, and R. H. Holzworth (2013), Attenuation of lightning-produced sferics in the Earth-ionosphere waveguide and low-latitude ionosphere, *Journal of Geophysical Research: Space Physics*, *118*(6), 3692–3699, doi:10.1002/jgra.50351.

Carlson, B. (2009), Terrestrial Gamma-Ray Flash production by lightning, Ph.D. thesis.

Carlson, B. E., N. G. Lehtinen, U. S. Inan, N. B. Crosby, T.-Y. Huang, and M. J. Rycroft (2009), Observations of Terrestrial Gamma-Ray Flash Electrons, *AIP Conference Proceedings*, pp. 84–91, doi:10.1063/1.3137717.

Carlson, B. E., T. Gjesteland, and N. Østgaard (2011), Terrestrial gamma-ray flash electron beam geometry, fluence, and detection frequency, *Journal of Geophysical Research*, *116*, A11217, doi:10.1029/2011JA016812.

Celestin, S., and V. P. Pasko (2011), Energy and fluxes of thermal runaway electrons produced by exponential growth of streamers during the stepping of lightning leaders and in transient luminous events, *Journal of Geophysical Research*, *116*, A03315, doi:10.1029/2010JA016260.

Christian, H. J. (2003), Global frequency and distribution of lightning as observed from space by the Optical Transient Detector, *Journal of Geophysical Research*, *108*(D1), 4005, doi:10.1029/2002JD002347.

Cohen, M. B., U. S. Inan, R. K. Said, M. S. Briggs, G. J. Fishman, V. Connaughton, and S. A. Cummer (2010), A lightning discharge producing a beam of relativistic electrons into space, *Geophysical Research Letters*, *37*, L18806, doi:10.1029/2010GL044481.

Coleman, L. M., and J. R. Dwyer (2006), Propagation speed of runaway electron avalanches, *Geophysical Research Letters*, *33*, L11810, doi:10.1029/2006GL025863.

Collier, A. B., T. Gjesteland, and N. Østgaard (2011), Assessing the power law distribution of TGFs, *Journal of Geophysical Research*, *116*, A10320, doi: 10.1029/2011JA016612.

Connaughton, V., et al. (2010), Associations between Fermi Gamma-ray Burst Monitor terrestrial gamma ray flashes and sferics from the World Wide Lightning Location Network, *Journal of Geophysical Research*, *115*, A12307, doi:10.1029/2010JA015681.

Cooray, V. (2003), *Mechanism of electrical discharges*, IEE Power Series, 45–123 pp., Institution of Engineering and Technology, London.

Davis, A. (2012), High-Resolution Count Rates from SAMPEX/HILT.

Dowden, R., J. Brundell, and C. Rodger (2002), VLF lightning location by time of group arrival (TOGA) at multiple sites, *Journal of Atmospheric and Solar-Terrestiral Physics*, *64*, 817–830.

Dowden, R., et al. (2008), World-wide lightning location using VLF propagation in the Earth-ionosphere waveguide, *IEEE Antennas and Propagation Magazine*, *50*(5), 40–60.

Dwyer, J. R. (2003), A fundamental limit on electric fields in air, *Geophysical Research Letters*, *30*, 2055, doi:10.1029/2003GL017781.

Dwyer, J. R. (2004), Implications of x-ray emission from lightning, *Geophysical Research Letters*, *31*, L12102, doi:10.1029/2004GL019795.

Dwyer, J. R. (2008), Source mechanisms of terrestrial gamma-ray flashes, *Journal of Geophysical Research*, *113*, D10103, doi:10.1029/2007JD009248.

Dwyer, J. R., and M. a. Uman (2014), The physics of lightning, *Physics Reports*, *534*, 147–241, doi:10.1016/j.physrep.2013.09.004.

Dwyer, J. R., B. W. Grefenstette, and D. M. Smith (2008), High-energy electron beams launched into space by thunderstorms, *Geophysical Research Letters*, *35*, L02815, doi:10.1029/2007GL032430.

Dwyer, J. R., D. M. Smith, M. A. Uman, Z. Saleh, B. Grefenstette, B. Hazelton, and H. K. Rassoul (2010), Estimation of the fluence of high-energy electron bursts produced by thunderclouds and the resulting radiation doses received in aircraft, *Journal of Geophysical Research*, *115*, D09206, doi:10.1029/2009JD012039.

Encyclopædia Britannica, I. (2007), Electrical charge distribution in a thunderstorm, (see `http://search.eb.com/eb/article-9048228`).

Finlay, C. C., et al. (2010), International geomagnetic reference field: the eleventh generation, *Geophysical Journal International*, *183*, pp. 1216–1230, doi:10.1111/j.1365-246X.2010.04804.x.

Fishman, G., P. Bhat, R. Mallozzi, and J. Horack (1994), Discovery of intense gamma-ray flashes of atmospheric origin, *Science*, *264*(5163), 1313–1316.

Gjesteland, T., N. Østgaard, A. B. Collier, B. E. Carlson, C. Eyles, and D. M. Smith (2012), A new method reveals more TGFs in the RHESSI data, *Geophysical Research Letters*, *39*, L05102, doi:10.1029/2012GL050899.

Grefenstette, B. W., D. M. Smith, B. J. Hazelton, and L. I. Lopez (2009), First RHESSI terrestrial gamma ray flash catalog, *Journal of Geophysical Research*, *114*, A02314, doi:10.1029/2008JA013721.

Gurevich, A. V., G. M. Milikh, and R. Roussel-Dupre (1992), Runaway electron mechanism of air breakdown and preconditioning during a thunderstorm, *165*, 463–468.

Henley, E. M., and A. L. Garcia (2007), *Subatomic Physics*, 3 ed., 640 pp., World Scientific Publishing Co. Pte. Ltd, London - Hackensack.

Jacobson, A., R. Holzworth, J. Harlin, R. Dowden, and E. Lay (2006), Performance assessment of the world wide lightning location network (WWLLN), using the Los Alamos sferic array (LASA) as ground truth, *Journal of Atmospheric and Oceanic Technology*, *23*, 1082–1092.

Khairul, K., M. Mohammad, A. Mardina, and L. Kevin (2011), Investigation of the D-region Ionosphere characteristics using Tweek Atmospherics at Low Latitudes, *Proceeding of the 2011 IEEE International Conference on Space Science and Communication*, (July), 130–133.

Klecker, B., et al. (1993), HILT: a heavy ion large area proportional counter telescope for solar and anomalous cosmic rays, *IEEE Transactions on Geoscience and Remote Sensing*, *31*(3), 542–548.

Korth, H. (2008), IDL Geopack DLM, `http://ampere.jhuapl.edu/code/idl_geopack.html`.

Lehtinen, N. G., and U. S. Inan (2005), Conditions for production of terrestrial gamma-ray flashes.

Lehtinen, N. G., T. F. Bell, and U. S. Inan (1999), Monte Carlo simulation of runaway MeV electron breakdown with application to red sprites and terrestrial gamma ray flashes, *Journal of Geophysical Research*, *104*(A11), 24,699–24,712.

Marisaldi, M., et al. (2010), Detection of terrestrial gamma ray flashes up to 40 MeV by the AGILE satellite, *Journal of Geophysical Research*, *115*, A00E13, doi:10.1029/2009JA014502.

Mason, G. M., et al. (1998), SAMPEX: NASA's first small explorer satellite, *Aerospace Conference*, *5*, 398–412, doi:10.1109/AERO.1998.685848.

McDaniel, W. (1989), *Atomic collisions: electron and photon projectiles*, Atomic Collisions, 699 pp., Wiley.

Meegan, C., et al. (2009), The Fermi Gamma-Ray Burst Monitor, *The Astrophysical Journal*, *702*(1), 1–36, doi:10.1088/0004-637X/702/1/791.

Moss, G. D., V. P. Pasko, N. Liu, and G. Veronis (2006), Monte Carlo model for analysis of thermal runaway electrons in streamer tips in transient luminous events and streamer zones of lightning leaders, *Journal of Geophysical Research*, *111*, A02307, doi:10.1029/2005JA011350.

NASA Goodard (2015), Astrphysics & Heliophysics Explorers Missions, `http://explorers.gsfc.nasa.gov/missions.html`, [Accessed: 13.01.2015].

Østgaard, N., T. Gjesteland, R. S. Hansen, A. B. Collier, and B. Carlson (2012), The true fluence distribution of terrestrial gamma flashes at satellite altitude, *Journal of Geophysical Research*, *117*, A03327, doi:10.1029/2011JA017365.

Pasko, V. P. (2010), Recent advances in theory of transient luminous events, *Journal of Geophysical Research*, *115*, A00E35, doi:10.1029/2009JA014860.

Rakov, V. A., and M. A. Uman (2007), *Lightning: Physics and Effects*, 687 pp., Cambridge University Press, New York.

Rodger, C. J., J. B. Brundell, and R. L. Dowden (2005), Location accuracy of VLF World-Wide Lightning Location (WWLL) network: Post-algorithm upgrade, *Annales Geophysicae*, *23*, 277–290.

Roussel-Dupre, R., and A. V. Gurevich (1996), On runaway breakdown and upward propagating discharges, *101*, 2297–2311, doi:10.1029/95JA03278.

Skeltved, A. B. (2013), A study of the relativistic runaway electron avalanche and the feedback theory to explain terrestrial gamma-ray production, Master Thesis.

Smith, D. M., L. I. Lopez, R. P. Lin, and C. P. Barrington-Leigh (2005), Terrestrial Gamma-Ray Flashes Observed up to 20 MeV, *Science*, *307*, 1085–1089.

Smith, D. M., et al. (2006), The Anomalous Terrestrial Gamma-ray Flash of 17 January 2004, *Eos Trans. AGU*, p. 87(52).

Smith, D. M., B. J. Hazelton, B. W. Grefenstette, J. R. Dwyer, R. H. Holzworth, and E. H. Lay (2010), Terrestrial gamma ray flashes correlated to storm phase and tropopause height, *Journal of Geophysical Research*, *115*, A00E49, doi:10.1029/2009JA014853.

Stolzenburg, M., and T. C. Marshall (2008), Charge Structure and Dynamics in Thunderstorms, *Space Science Reviews*, *137*(1-4), 355–372, doi:10.1007/s11214-008-9338-z.

Stolzenburg, M., W. D. Rust, and T. C. Marshall (1998), Electrical structure in thunderstorm convective regions: 3. Synthesis, *Journal of Geophysical Research*, *103*, 14097–14108, doi:10.1029/97JD03545.

Tipler, P. A., A. Ralph Llewellyn, and M. Llewellyn (2012), *Modern Physics*, 702 pp., W.H. Freeman, New York - Basingstoke.

Wilson, C. T. R. (1925), The Acceleration of β-particles in Strong Electric Fields such as those of Thunderclouds, *Mathematical Proceedings of the Cambridge Philosophical Society*, *22*(04), 534, doi:10.1017/S0305004100003236.

Xiong, S., et al. (2012), Location prediction of electron TGFs, *Journal of Geophysical Research*, *117*, A02309, doi:10.1029/2011JA017085.